NASA-CR-194223

127p.

(NASA-CR-194223) ARCING IN SPACE
STRUCTURES IN LOW EARTH ORBIT Final
Report, 1 Jan. 1990 - 29 Dec. 1991
(Physical Sciences) 127 p

N94-32478

Unclas

G3/33 0010559

SBIR 1987 Phase II

NASA
National Aeronautics and Space Administration

Report Documentation Page

NASA-CR-194223

2. Government Accession No.

3. Recipient's Catalog No.

4. Title and Subtitle

Arcing in Space Structures in Low Earth Orbit

5. Report Date

January 1992

6. Performing Organization Code

7. Author(s)

B.L. Upschulte, W.J. Marinelli, G. Weyl
and K.L. Carleton

8. Performing Organization Report No.

PSI-2123/TR-1153

10. Work Unit No.

9. Performing Organization Name and Address

Physical Sciences Inc.
20 New England Business Center
Andover, MA 01810

11. Contract or Grant No.

NAS3-25797

13. Type of Report and Period Covered

Final Report
1 Jan 90 to 29 Dec 91

12. Sponsoring Agency Name and Address

NASA Lewis Research Center
Research & Technology Branch
21000 Brookpark Road, MS 500-305
Cleveland, OH 44135

14. Sponsoring Agency Code

3350-LMK

15. Supplementary Notes

SBIR-10-01-9030
Release Date: 4-15-94

P-

16. Abstract

This report describes results of an experimental and theoretical program to investigate arcing of structures containing dielectric and conducting materials when they are biased negatively with respect to a plasma. An argon ion source generated Ar^+ ions of directed energy 20 to 40 eV and density $\sim 10^7$ cm^{-3} that impinged upon samples containing a dielectric material on top of a negatively biased Kovar plate. Arcing events were studied for bias voltages between -300 and -1000V with respect to the ion beam. The samples were Dow Corning 93-500 adhesive on Kovar, fused silica cover slips bonded on Kovar, and silicon solar cells mounted on Kovar. Measurements of discharge current, Kovar plate voltage, and radiation from the arc versus time were carried out. Microsecond duration exposure images and optical spectra in the 0.24 to 0.40 μm band were also acquired durign arcing events. Arcing events were found to be associated with exposed adhesive and means were found to eliminate arcing altogether. The charging of a silica cover plate and the fields around the plate were calculated using a particle-in-cell code. Models were developed to explain the ignition of the arc and the physical processes occurring during the discharge.

17. Key Words (Suggested by Author(s))

Solar Cell
High Voltage
Arcing
Spectrum
Adhesive
Cover Glass
Contamination
Space Plasma

18. Distribution Statement

19. Security Classif. (of this report)	20. Security Classif. (of this page)	21. No. of pages	22. Price
Unclassified	Unclassified	104	

NASA FORM 1626 OCT 86

CONTENTS

Page

FIGURES

FIGURES (Continued)

FIGURES (Continued)

Figure No. Page

TABLES

1. INTRODUCTION

An important factor in the development of high power solar array systems for space vehicles is the weight penalty associated with the power distribution network. In conventional solar array power systems cells with a bandgap of approximately 1 volt are connected in series to achieve an array voltage of 32 volts, which is regulated to a constant 28 volt level. A large assembly of these arrays, ganged in parallel, are used to meet the power requirements of large space vehicles. As the need for even larger (> 10 kW) power systems arises, it has become apparent that significant savings can be obtained by operating these arrays at higher voltages. This mode of operation, accomplished by connecting a larger number of cells in series, alleviates the need for much of the power distribution network.

However, interaction of the high voltage ends of the arrays with the ambient space plasma found in low earth orbit leads to surface flashover for positively biased components and arcing in negatively biased components. Experiments conducted on both the PIX I and PIX II experiments showed that the arc frequency was dependent on both the bias voltage and plasma density[1-3]. Numerous experiments[4-13] conducted in space plasma simulation chambers using negatively biased cells have noted the occurance of several common phenomenon:

1. An apparent threshold for arcing near -200 volts and a steep dependence of the arc rate on bias voltage.
2. A conditioning of the cells manifested as an initially high arc rate which then decreased to a constant level in time.
3. A propensity for the cells to arc at "triple junctions" occuring at the interconnect region or along the cell/cover glass interface.

Two distinct mechanisms are advanced to explain the propensity for arcing in these arrays. Dielectric breakdown of a thin layer of insulating contaminant covering the metallic interconnect has been proposed to explain arc initiation by Parks, Jongeward, Katz, and Davis[14]. In a plasma environment ions are attracted to the surface of the contaminant layer by the negative potential of the underlying interconnect, neutralizing the layer's surface. The large internal fields generated across the contaminant layer lead to emission across the interface and vaporization of the contaminant. The discharge is sustained via electron ionization of the vaporized layer. Hastings, Weyl, and Kaufmann[15, 16] have proposed that arcs are generated by the desorption and ionization of neutral molecules from the surface of the cover glass as a result of electron emission from the interconnect. The available experimental evidence provides confirmation for neither theory.

A first step towards the use of high voltage solar array panels is being taken in the design and construction of Space Station Freedom (SSF). Current design specifications call for the solar array power system to operate at 160 volts with the negative end of the array serving as ground. This voltage was chosen because arcing of the array system was not believed to be significant at these voltages. A schematic diagram of the station is shown in Figure 1. Ground return for the array panels is provided through the truss assembly, which is constructed of anodized aluminum. The behavior of the array system in LEO depends in a complex manner on the interaction of the array with the surrounding plasma. Figure 2 shows a simplified equivalent electrical diagram for the SSF power system. The floating potential of the station components with respect to the space plasma depends on the current collecting characteristics of the array and structural components. These parasitic currents must be minimized to reduce sputtering of the spacecraft surfaces. In addition, the ratio of the electron and ion currents must be managed to insure that the voltage (with respect to the space plasma) attained by spacecraft components does not exceed the dielectric breakdown strength of the materials or coatings.

When fully insolated, current models of the SSF environment predict that electron collection by the array cell edges and interconnects will drive the return side of the array to -130 volts[17]. Thus the anodized aluminum coating on the truss (which is an insulator) must be capable of withstanding the -130 volt bias. The anodized coating is present primarily as a thermal control surface. Current specifications call the for ratio of the visible absorptivity to the IR emissivity of the coating to have a value of 0.9. This requirement has driven the anodization of the aluminum towards a chromic acid process that results in a coating thickness on the order of 0.07 to 0.10 mils (1.8 to 2.5 μm). Measurements of arcing thresholds for these films reported by Carruth et al.[17] at NASA Marshall and Grier et al.[18] at NASA Lewis have shown these coatings to have a breakdown threshold of -120 to -140 volts. Furthermore, extensive sputtering of the arc site is noted as is a propensity for site to arc repetitively and at lower bias voltages once formed. Measurements conducted on a somewhat thicker (0.2 mil or 50 μm) coating produced by a sulfuric acid process have been observed to arc at -500 to -600 volts[18]. However, once an arc site is formed arcing is observed to occur at voltages as low as -140 volts at these sites. While the sulfuric acid process coating would appear to be ideal from an electrical standpoint, the IR emissivity of the coating is too high and results in excessive cooling of the structure.

Ion collection by the structure is enhanced by coating as many surfaces as possible with Z93 thermal control paint, which has been shown to be a conductor[19]. The ability of Z93 to perform as a conductor in a space environment has recently been called into question following tests at NASA Lewis Research Center and Cleveland State University.[20,21] In addition, to reduce electron collection by the array cell edges, it has been proposed to allow the DC93-500 adhesive used to bond the protective cover slips to the cells to coat the cell edges - forming an insulating layer. Concerns regarding sputtering and outgassing of the adhesive, resulting in contamination and possible degradation of nearby components, have been expressed and this concept remains under evaluation. Finally, the use of a plasma contactor to counter electron collection on the structure and raise the spacecraft potential has been proposed. However, these devices consume substantial amounts of power and are electrically noisy.

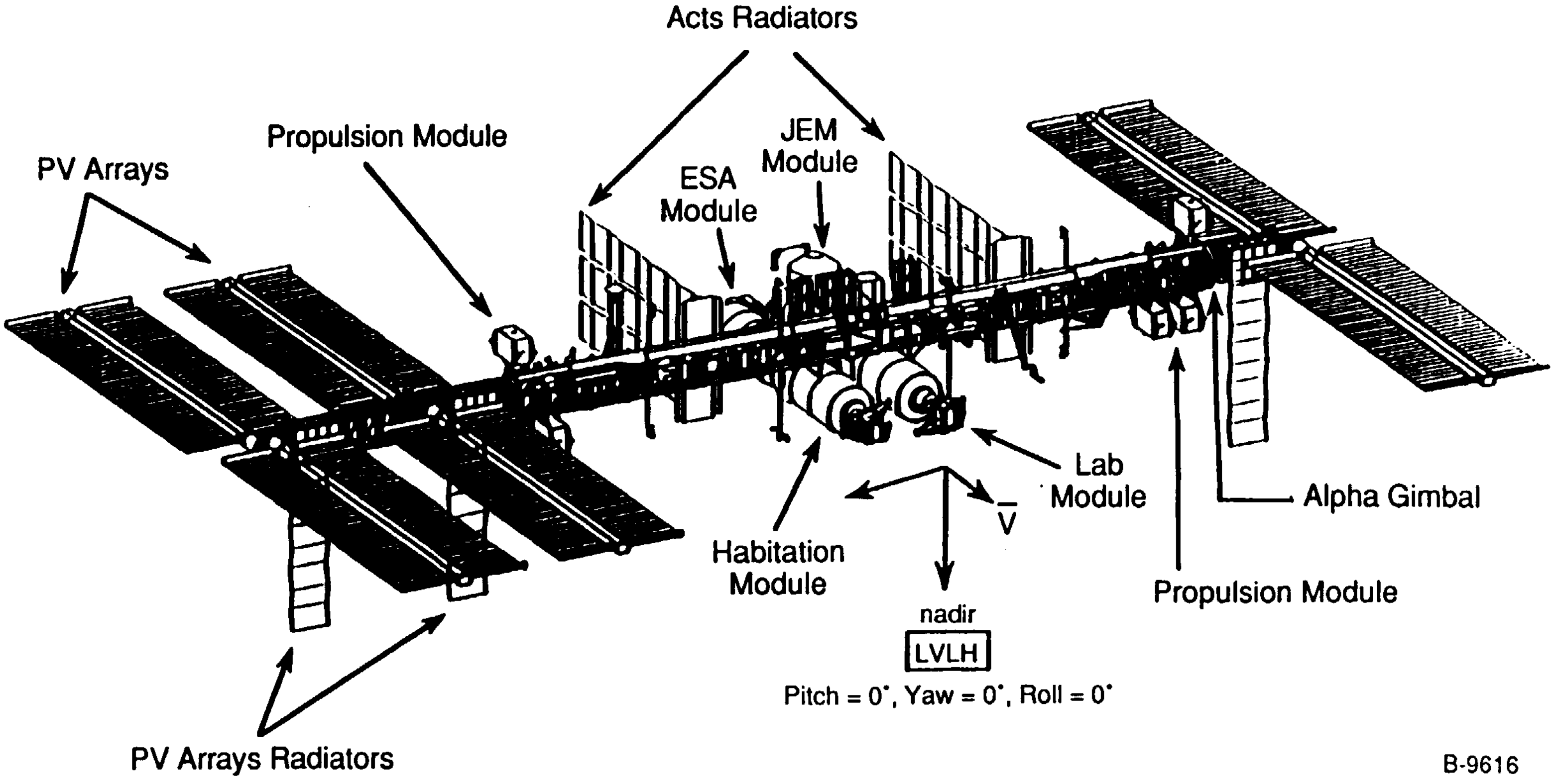

Figure 1. Space Station Freedom Man Tended Configuration.

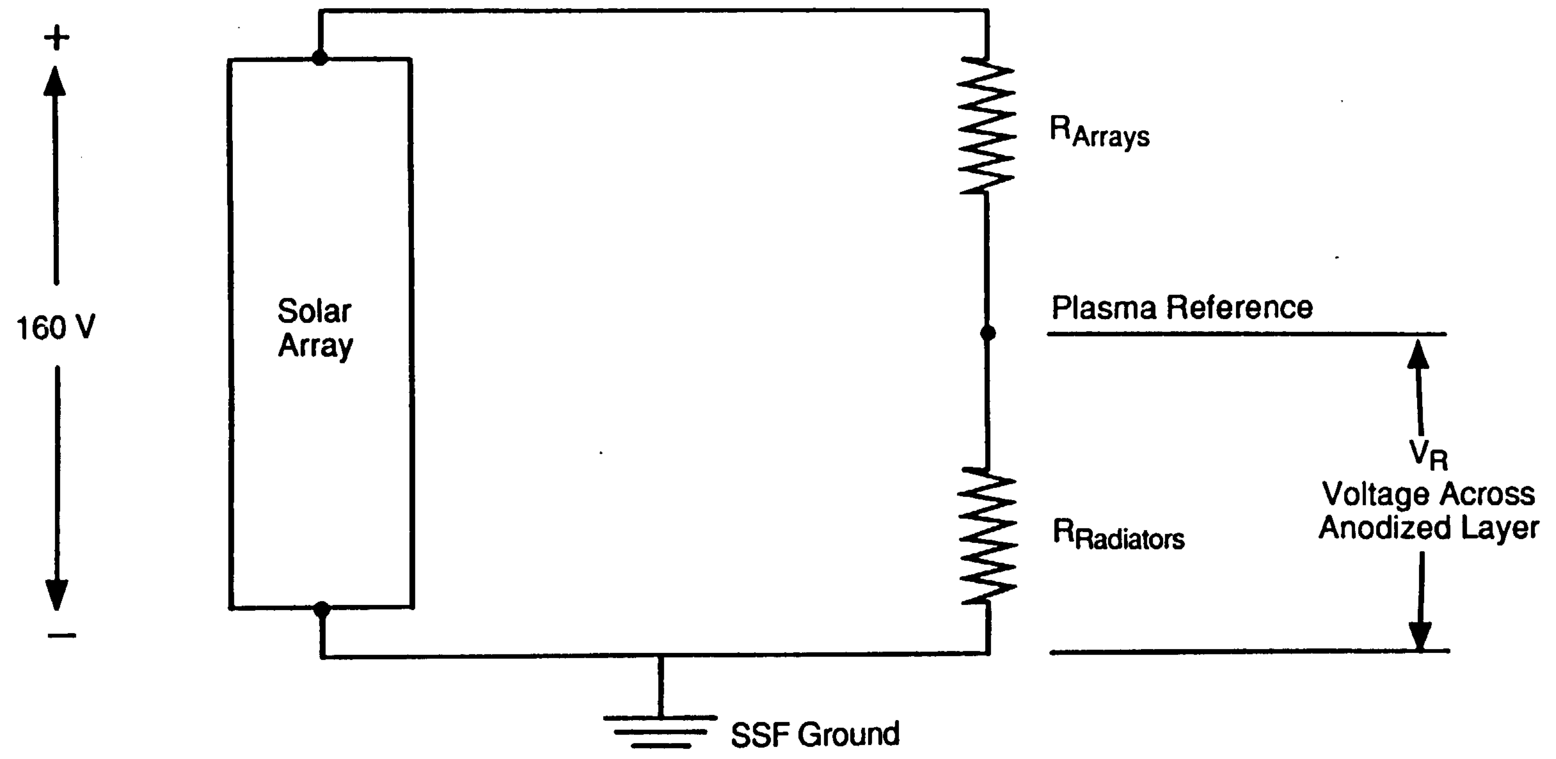

R_{Arrays} - "Impedance" of Arrays to Collecting Electrons from Plasma
$R_{Radiators}$ - "Impedance" of Radiators to Collecting Ions from Plasma

$$V_R \propto \left(\frac{R_{Radiators}}{R_{Arrays} + R_{Radiators}} \right) (-160\ \text{V})$$

B-9606

Figure 2. Space Station Freedom Charging Potential Equivalent Circuit.

The discussion presented above illustrates the interrelated nature of the problems associated with operating these arrays at high voltage. The performance of the entire system hinges upon the interplay between the power, thermal control, contamination management, and communications systems. At the heart of this interplay is the interaction of these biased structures with the LEO plasma environment.

The efforts described in this report seek to discover and mitigate the fundamental processes that are responsible for arcing and, to a lesser extent, parasitic current collection. The approach is two-fold, with an experimental investigation of these processes coupled to a theory and modelling effort. The goal of the approach is the use of the experiments to uncover the physical processes responsible for arcing. The processes are then generalized within the theory and modelling effort to enable prediction of arcing phenomenon for different physical configurations and compositions. The efforts addressed two primary issues: 1) the arcing of negatively biased solar cells placed in an LEO plasma environment and 2) the arcing of anodized aluminum coatings to be employed on the SSF truss structure. This work is described in Sections 2 and 4 respectively. In the course of investigating the arcing of solar cells, it became apparent that the interaction of DC93-500 adhesive with the space plasma and ambient environment was a key factor in determining arcing rates. This adhesive is used to bond the protective cover slips to the solar cells. Therefore, we investigated this phenomenon in more detail. These results are presented in Section 3. The development of a theory to address the arcing of solar cells in an LEO environment is presented in Section 5 and is coupled to comparisons with both flight (PIX II) and laboratory (present work) data. Finally, recommendations and conclusions based on both the experimental and theoretical investigations are presented in Section 6.

2. EXPERIMENTAL INVESTIGATIONS OF SOLAR CELL ARCING

There have been numerous laboratory investigations of both solar cell arcing and parasitic current collection under negatively biased conditions in an LEO plasma environment.[4-14] In contrast, there have been a significantly fewer number of flight investigations. In general, the major difference between the two type of measurements have been the use of relatively high density rare gas plasmas (10^5 to 10^6 ions cm^{-3}) in laboratory systems compared to the much lower density (10^2 to 10^4 ions cm^{-3}), largely oxygen plasmas found in LEO. Given the apparent scaling of arc rate with plasma density obtained in the PIX II flight data and other disparities in measurements, the validity of ground testing for these systems is constantly at issue. This situation is aggravated by the sparse and often compromised quality of the flight data[1-3]. The chief concerns in the comparison of ground and flight data are the possibility that oxygen plasmas play an additional chemical role in arcing behavior and that, as the plasma densities are lowered in test chambers, sheath sizes become comparable to the chamber dimensions. In the latter regime, the fundamental nature of the interaction may change.

2.1 Approach

Our measurement program was not targeted at measuring accurate arcing rates for specific array configurations, i.e. quantitative comparisons with flight data was not a primary goal of the effort. Previous work on the theory of arcing, developed under Phase I of this effort,[15,16] had indicated that surface contaminants and microscopic surface structures might play a role in arc initiation and maintenance. Hence, a primary goal of this effort was the conduct of arcing measurements under conditions where surface composition, structure, and contamination could be controlled and verified.

A key feature of this work was the conversion of an ultra-high vacuum (UHV) surface science chamber to a space plasma test facility for the conduct of these measurements. The facility will be described in greater detail below. However, it must be emphasized that the ability to control the chamber pressure at the 10^{-9} torr level was a primary factor in determining the role of the DC93-500 adhesive in solar cell arcing. Furthermore, the use of in situ diagnostics, such as Auger and mass spectroscopy, enabled us to understand and control both the surface and gas phase compositions. Finally, our effort was one of the first to employ quantitative optical imaging of solar cell arcing and to correlate optical emission with arc strength. The use of a gated and intensified CCD array camera system enabled us to determine the location of arcing sites in real time and was a valuable tool in the identification of adhesive as a participant in the arc process.

Early in the conduct of these measurements three issues arose concerning the reporting of arcing phenomenon: 1) how does one define an arc, 2) how does one (or can one) measure an arcing threshold, and 3) what are the appropriate conditions for making arcing measurements. Our experiments in general noted that solar cell discharge phenomenon fell into two regimes. One regime was characterized by frequently occurring discharges, short in duration (~50 ns), which dissipated little charge and had a immeasurable impact on the measured cell voltage. Interspersed with these small arcs (or pre-arcs) were larger events, of 1 to 5 μs in duration, which transferred significant amounts of charge from the array to the surrounding plasma and resulted in a significant (5 percent) reduction in the cell voltage. The shorter arcs produced no detectable optical emission while, as will be seen, optical emission from the larger arcs could be directly correlated with the amount of charge dissipated. From a power system perspective, the shorter duration arcs would have a negligible impact on power delivery while the larger arcs could significantly reduce the amount of power available to the spacecraft. We chose as an operational definition of an arc one in which the observed voltage drop was greater than 5 percent of the bias voltage and where optical emission was detectable. The latter constraint was imposed to eliminate the counting of arcs which might originate from sites other than the solar cell, such as exposed leads. Arcing of leads was a problem uncovered early in the program and corrected, but the optical emission constraint was continued to guard against the possible failure of a performing lead system.

A constantly recurring question in the performance of the experimental effort was the issue of a threshold for the arcing process. From a system standpoint, operation of an array below the threshold would insure no deleterious effects due to the arcing process. For there to be a true threshold for the arcing process there would have to be a part of the process that was energetically unfavorable below a given bias voltage, such as a sputtering process or secondary electron emission. In the laboratory, or in a flight experiment, one measures arcing rates and looks to find a voltage below which arcing is never observed. In practice, arcing rates become negligible as one approaches the -100 to -300 volt regime, with the time between arcs approaching the available measurement time. The measurement in time in the laboratory is often restricted by the lifetime of the plasma source or the affordability of the vacuum chamber test time. In flight the plasma conditions are constantly changing during the orbit, which limits the ability to make the prolonged observations required to measure low arc rates.

The use of larger arrays to measure arcing rates at low voltages could, in principle, improve the measurements by increasing the number of arc sites. However, in practice arcs from different parts of the array are correlated through depletion of surface charge on large parts of the array from an arc occurring at a single site. Thus, in low plasma density environments the arc rate is determined by the recharge rate of the array dielectric surfaces and the arcing rate of the site with the lowest threshold. Hence, measurements of arc thresholds are much more likely to reflect the ability of the experimenter to count low arc rates than the discovery of a true threshold. These measurements may not be particularly relevant, since the SSF power system must perform for periods which are orders of magnitude longer than any controlled experiments performed to date. Our approach to addressing this issue is to understand that we can only determine a bound for the threshold and instead look for changes in the cell design processing which have a significant impact on the measured arc rate. In general, the approach seeks to eliminate arcing sites altogether and avoid a semantic discussion of arcing thresholds.

Finally, many efforts have noted a reduction in cell arc rates over time at a specific bias voltage, or a conditioning of the cell. In general, the rate of conditioning is accelerated at higher bias voltages. Thus, arc rates measured on an unconditioned cell could be a convolution of the true arc rate with the conditioning process. Our approach to avoiding these artifacts has been to condition the cells at -1000 volts bias until the arc rate stabilizes at a fixed value.

2.2 Experimental Apparatus

All experiments were conducted in the previously mentioned ultra-high vacuum chamber. The chamber is a 21 in. long by 10 in. o.d. cylinder in which all ports are sealed with Cu gaskets and knife edge flanges to allow operation at pressures as low as 2×10^{-11} torr. The chamber is shown schematically in Figure 3 and described below. In the forward section of the chamber are four 6 in. clear aperture ports employed for operation of sample diagnostics. An Auger electron spectrometer is located on the top flange and may be positioned to within 0.25 in. of the sample for surface analysis. A differentially pumped quadrupole mass spectrometer (0 to 300 amu range) is located on the lower port and is configured to detect species desorbed from the sample as well as the background environment. Ports on either side of the chamber and on the end wall are available for optical access. In these experiments the end wall port is used for optical access and may be equipped with a fast, low resolution optical spectrometer for discharge characterization. A camera system may be employed to photograph arcing events from this port as well. One of the side ports is fitted with the plasma source. The end-wall of the chamber may also be equipped with a retarding potential electron energy analyzer which may be employed to sample emission from the surface.

In the mid-section of the chamber four small access ports are provided for pressure measurement (ionization gauge), gas dosing, and a 0 to 5 keV ion sputtering gun for sample cleaning. In the rear section of the chamber ports are provided for a 1000 l/s turbomolecular pump and sample viewing.

The samples to be tested are mounted in the cradle of a 5 degree-of-freedom UHV sample manipulator which provides access to all of the forward ports in the chamber. High voltage and low-voltage isolated feedthrough are currently available for precise electrical measurements.

2.2.1 Plasma Source. - The plasma source, which is a Kaufmann type charge-neutralized ion source purchased from Ion Tech Inc., has been mounted on a vacuum flange and slides into a full nipple extension attached to a 8 in. conflat flange port on the UHV chamber, see Figure 3. The plasma source mounts using three 5/16-18 threaded rods. These rods are threaded into a conflat flange at the back. The opposite end of the threaded rods are supported by a circular aluminum collar concentric with the full nipple extension port on the UHV chamber. The plasma source mounting bracket slides on the threaded rods to allow the source to solar cell distance to be varied from 13 to 35 cm. The three rods

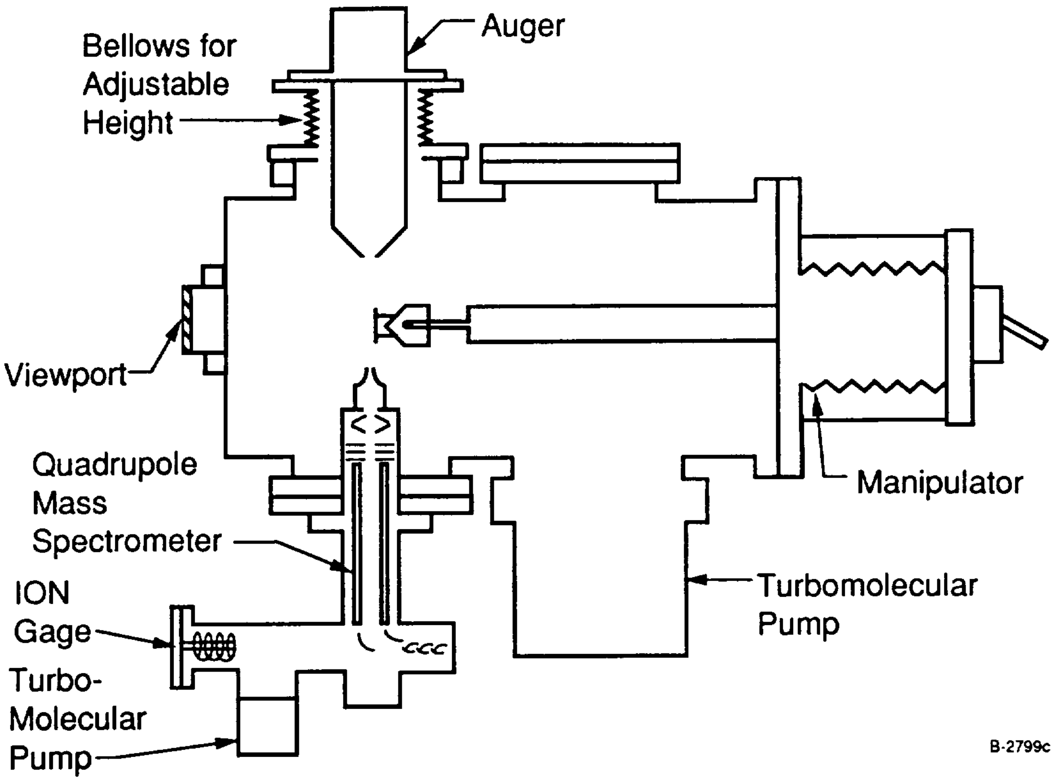

(a) Side View

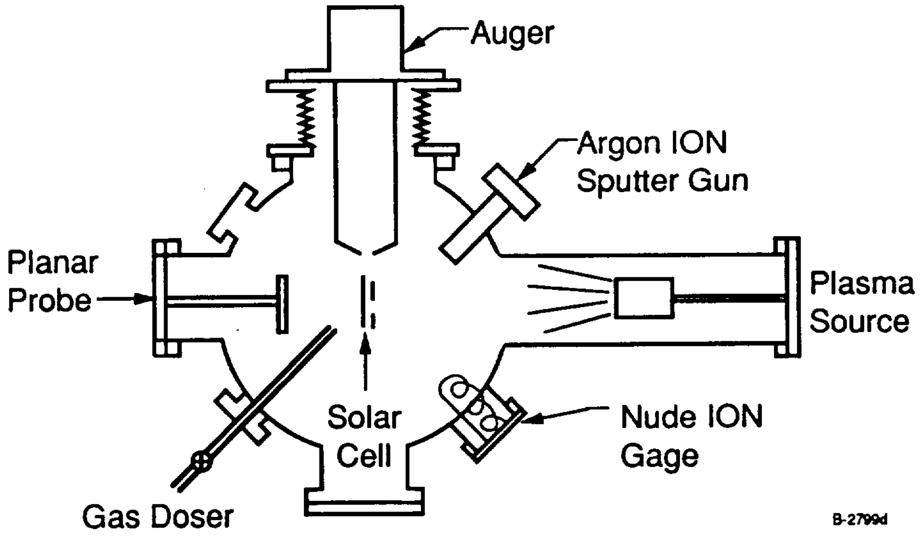

(b) View Along Manipulator Axis

Figure 3. - Schematic drawing of the UHV chamber showing location of diagnostics.

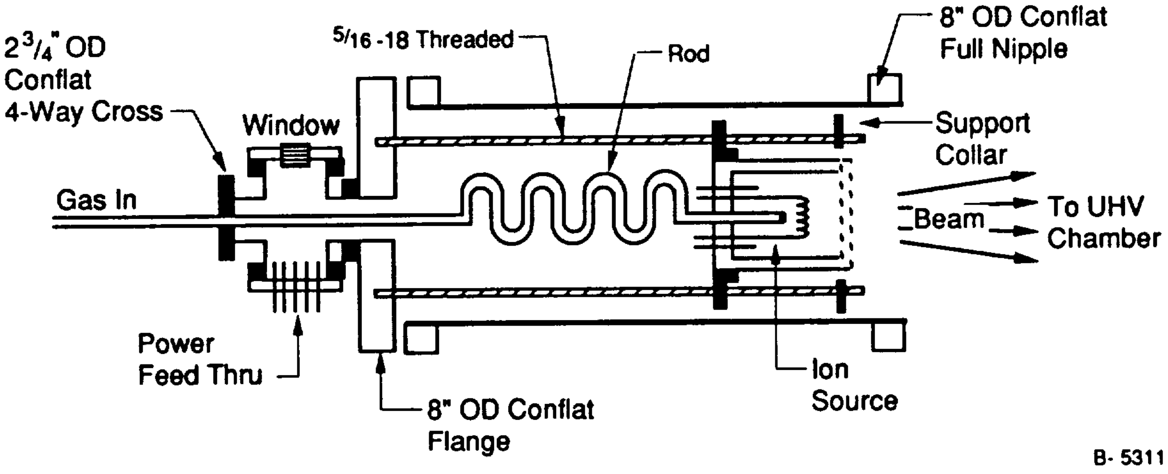

Figure 4. - Plasma source mounting arrangement.

are arranged in an optical mount pattern so that small angular adjustments may be specifically and reproducibly set. A 2-3/4 in. OD conflat four-way cross was added to the 8 in. OD mounting flange to provide feedthrough access to the plasma source. A coil of thin wall stainless steel tubing is used for the gas inlet line and allows the required flexibility. Electrical feedthroughs and UHV compatible electrical leads (18 in. long) were provided by Ion Tech Inc., as part of the plasma source.

The ion source discharge parameters include: cathode filament current (CFC), discharge current (DC), and discharge voltage (DV). The discharge voltage is nominally set to between 90 and 100V, corresponding to the electron energy at the peak of the ionization cross section curves for most gases. The discharge current is controlled by varying the cathode filament current, i.e., thermoelectron emission rate through the filament temperature. The cathode filament erodes in time, resulting in thinning of the tungsten cathode material (its operational lifespan is about 10 to 20 hr). This thinning leads to a monotonic increase in cathode temperature, emission rate and discharge current unless countered by reducing the CFC. Nominal discharge currents are about 0.2A, corresponding to 18W of power dissipation in the gas.

The ion beam parameters include: beam and accelerator grid voltage and current. The beam current is the current leaving the discharge chamber. This current has two components. The first component comes from ions that strike the accelerator grid and appears as accelerator grid current. The second component arises from ions accelerated by the accelerator grid to form a beam (jet or spray may be a better description). The difference between beam current and accelerator grid current is the actual current that propagates into the vacuum chamber. At high beam voltages the accelerator grid current is typically less than 10 percent of the beam current. At low voltages, ≤50V, these currents are within the resolution of the sensors, or about 1 mA. The beam voltage sets the ion translational energy when the ion (1) strikes a surface, or (2) crosses a plane at ground potential. The accelerator grid voltage extracts ions from the discharge cell and repels electrons back into the cell. The ion extraction efficiency is a complex function of the beam and accelerator grid voltages, discharge cell-accelerator grid spacing and hole size, as well as gas flow, gas temperature, and charge density in the discharge chamber of the ion source.

The neutralizer parameters include: neutralizer filament current, and filament emission current. Electron emission is controlled by the filament (heating) current. Typically, the emission level is set so that there is a net positive current (beam current minus accelerator grid current). The neutralizer filament is oriented along a diameter of the ion beam and immersed in it at a distance roughly 2 cm downstream of the exit plane of the ion source.

The pressure in the UHV chamber is related to the argon flow rate in the ion source. There is, however, a minimum flow rate for the ion source to be operational. Figure 5 shows the chamber pressure versus flow rate. As can be seen from this figure, the minimum Ar pressure in the UHV chamber is 5 x 10^{-6} torr. Figure 5 shows that the measured pressure is in excellent agreement with the calculated pressures.

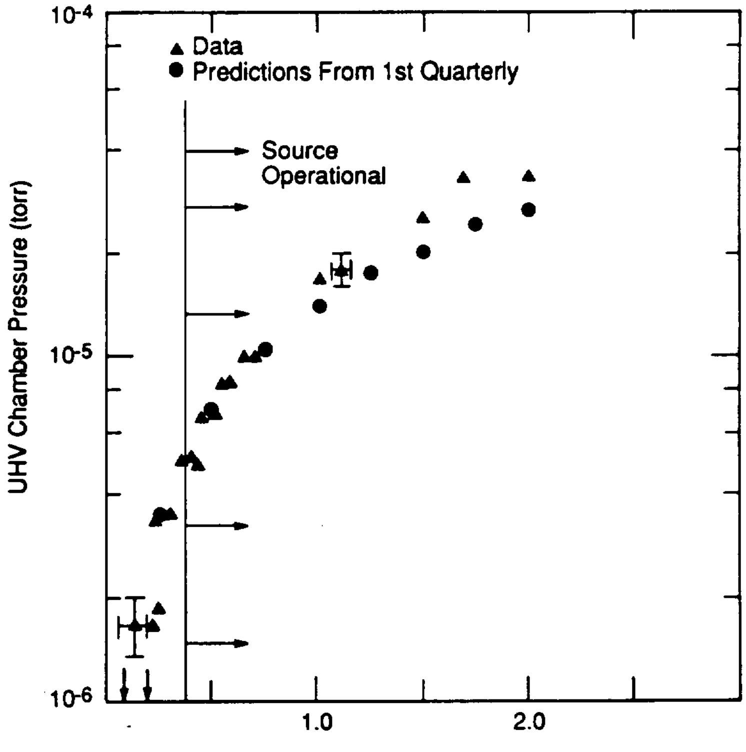

Figure 5. - Comparison of predicted and measured UHV chamber pressure during source operation

2.2.2 Langmuir Probe Measurements of Plasma Properties. - A planar and a cylindrical Langmuir probes were constructed and mounted on translational stage, as shown in Figure 6. The planar probe consisted of a 3.8 cm diameter copper disk, while the cylindrical probe had a length of 2.34 cm, width 0.25 mm and was oriented parallel to the incoming ion flow. Details of the electronics used to sweep the voltage and of the I versus V characteristics of these probes can be found in Reference 22. We present here only the results.

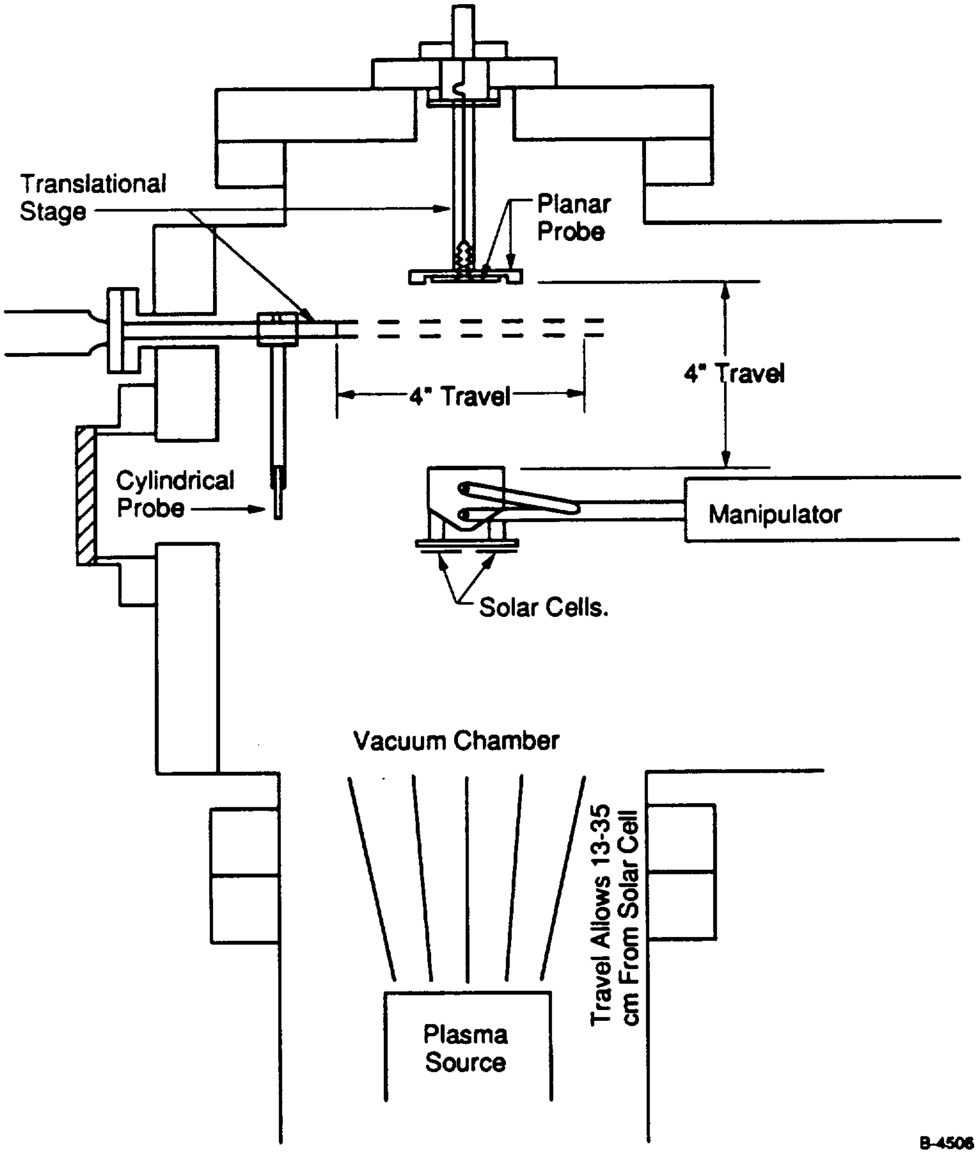

Figure 6. - Langmuir probe and solar cell mounting in UHV chamber.

Most of the samples tested were positioned 34 cm downstream from the source and the radial profile of the ion beam, obtained from a measurement of the ion saturation current using the cylindrical probe, is shown in Figure 7. The beam is seen to have a diameter of roughly 5 cm at half maximum. The plasma densities are presented in Table 1. As a function of ion extraction energy, the electron temperature was found to be 1.25 eV ±0.15 eV and the ion spread energy was 7.5 eV. As discussed in Reference 22 and shown in Figure 8, there is a sudden rise in ion current and density when the beam energy E_b exceeds 40 eV indicating that there is a dramatic increase in ion extraction efficiency above E_b = 40 eV.

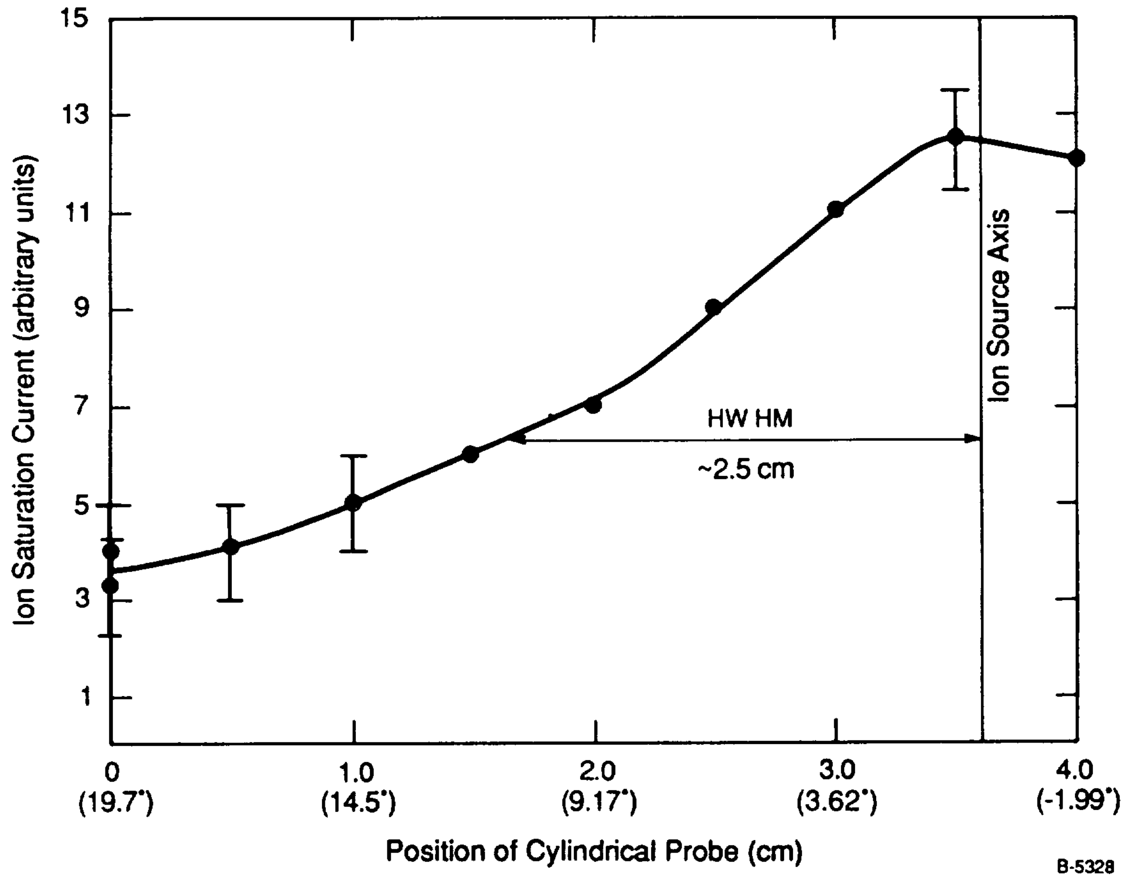

Figure 7. - Radial profile of ion saturation current, cylindrical probe.

TABLE 1. - PLASMA CHARACTERISTICS

Beam Energy (eV)	Electron Density (10^6 cm^{-3})	Ion Density (10^6 cm^{-3})
20	7.4 ± 1.5	5.6 ± 1.0
30	7.4	5.5
40	8.8	6.0
50	10.0	7.5
60	12.1	10.0

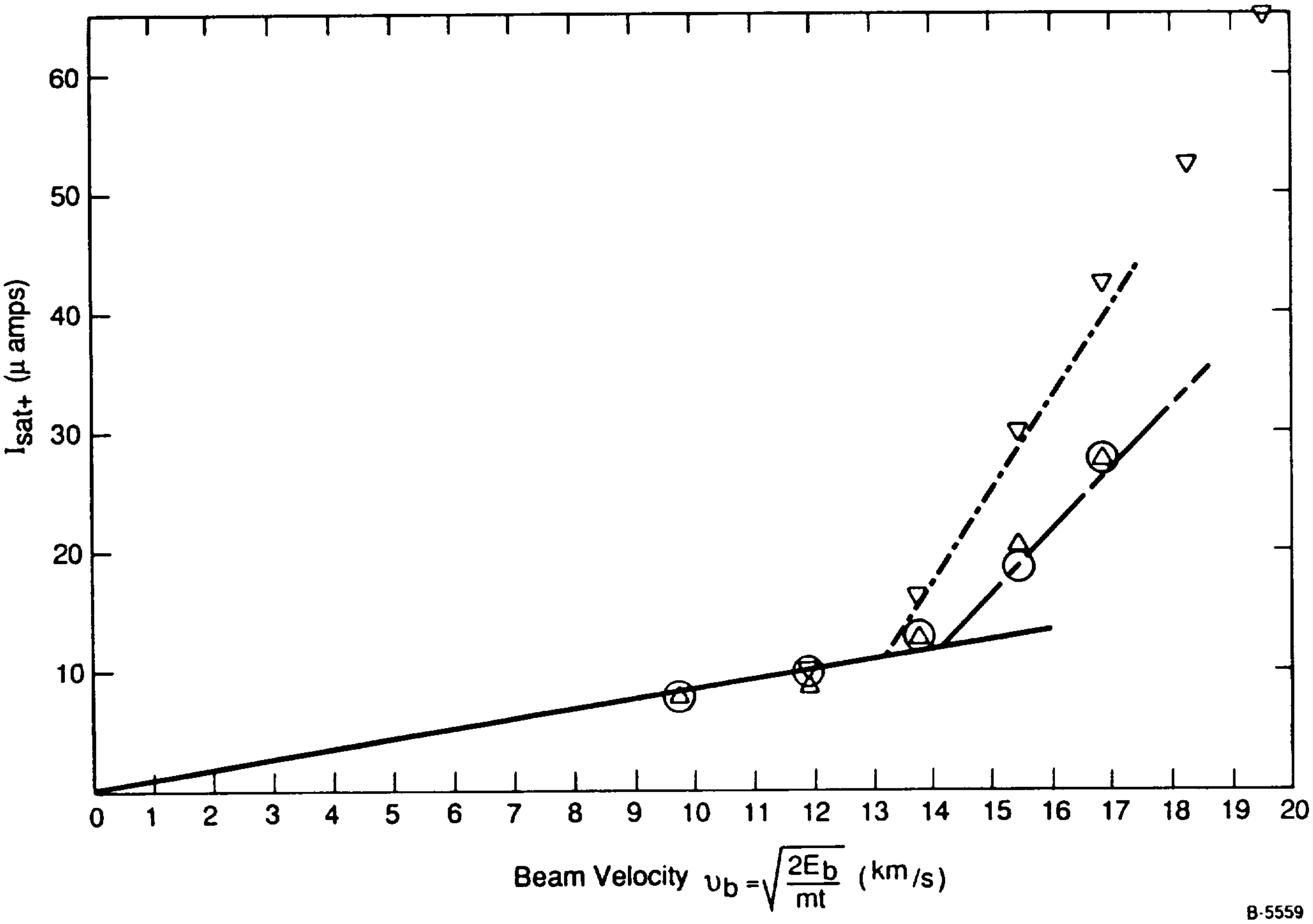

Figure 8. - Saturation current (I_{s+}) versus beam velocity (V_b) for planar Langmuir probe.

To investigate arcing behavior, standard plasma source conditions have been set for all the arc test series. These conditions include: 90V discharge voltage, 0.2A discharge current, 20 eV beam energy, 500V accelerator grid potential, and 1 mA electron neutralization current. The source to interconnect distance is about 25 cm and the ion saturation current is roughly 7 x 10^{-7} A/cm^2.

2.2.3 Electrical Diagnostics. - Samples were placed in the UHV chamber and mounted onto a Kovar plate which could be biased negatively with respect to the chamber walls and to the ion beam. The biasing circuit and arc sensing circuit are shown in Figure 9.

Design and construction of the arc sensing circuit is based on an experiment schematic by Snyder.[7] The data acquisition system used to record the arc time evolution is a Heath Zenith PC-based 20 MHz real time digital storage oscilloscope. The oscilloscope A/D channel senses a voltage drop across the 50Ω resistor as charge stored in the capacitors flow to the arc site. The time constant of the sensor is determined by the RC product of the 50Ω resistor and the 50 pf capacitance in series; i.e., 2.5 ns. Using a 13 MHz function generator to simulate an arc event and the digital oscilloscope in the interleaved mode, we have been able to confirm that the time response is less than 100 ns. For measuring arcs, which typically last a couple of μs, this is adequate response time. The recharge time of the arc-depleted interconnect by the power supply is controlled by the 10 MΩ resistor, 100 pf capacitor and series associated cable capacitance. This recharge time constant is on the order

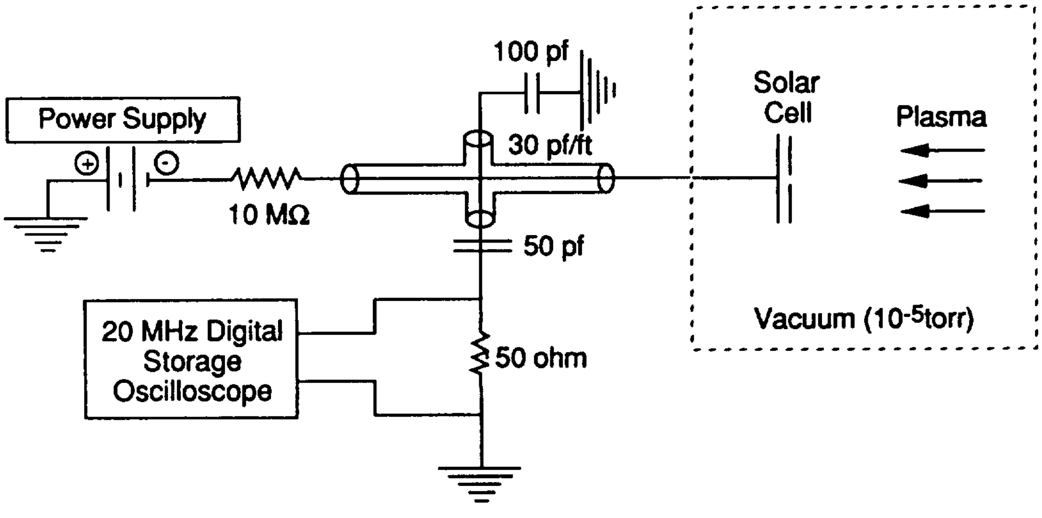

Figure 9. - Schematic for arc sensor circuit.

of 1 ms and thus does not contribute to observations made of the arc event in the 1 μs time frame. This 10 MΩ resistor also acts to protect the power supply by limiting its current output. The voltage drop across the 50Ω resistor actually arises due to only a fraction of the current drawn by the arc. This fraction corresponds to 50 pf divided by the total capacitance in the system beyond the 10 MΩ resistor, and is approximately 0.1. The oscilloscope trigger level acts as a threshold setting for arc current. Assuming the threshold is set at the 10 mV level, the current flowing through the 50Ω sensing resistor is 0.2 mA, but the corresponding total current flow from the system is 2 mA.

2.2.4 Solar Cell Mechanical and Electrical Mounting. - Early experiments used solar cells or coverslips mounted to insulated Kovar plates. These plates were biased using bare copper wires insulated with Varaflex©, a fiberous glass sleeving. Tests on biased leads showed considerable arcing, see Figure 10.

Elimination of the high voltage lead arcing was necessary to continue meaningful investigations of the solar cell arcing phenomena. This was accomplished by coating the entire conducting lead with a teflon heat shrink tube. In addition, the attachment point was placed in the shadow of the directed plasma source and the connection was recessed into the thickness of a copper support. During the course of this effort the support for the interconnect and solar cell was upgraded to facilitate the removal and insertion of different configurations, see Figure 11. The new support was constructed from a 1/4 in. thick rectangle of copper plate, just slightly larger than the rectangular Kovar interconnect plate. Two screw mounted pinch points were included at the ends of the long axis and serve to hold the interconnect plate and solar cell to the copper support. In this fashion the interconnect and solar cell could be inserted and removed without disturbing the negative high voltage lead, which is recessed and pinned into the back of the copper support. In the experiments using an actual solar cell, the solar cell was attached with a very small amount of adhesive to the interconnect/Kovar plate and the solar cell electrical lead was spot welded to the Kovar interconnect plate. A careful procedure was used in the mounting of the solar cell to avoid exposing the support adhesive to the plasma. Testing of the support and high voltage lead showed over a factor of ten reduction in the arc frequency compared with previous configurations and appeared to be declining with added exposure to the plasma. Ultimately, these events fell below detectability and this configuration has remained intact since that time.

2.2.5 UV Radiometer. - A UV radiometer, consisting of a Hamamatsu model R1220 solar blind photomultiplier tube in an EMI-GENCOM Model SRI/F housing was employed to observe emission of light from the array test region. This tube provides an active photocathode of about 3/4 in. in diameter, and response from 115 nm to about 305 nm with ~0.2 quantum efficiency. For our measurements the air transmission cutoff at around 190 nm sets the lower wavelength bound. Our sensitivity for arc related light emission is best in the UV. The detection of light emission in the visible is hindered by the bright scattered light of the 3000 K tungsten filament used to space charge neutralize the output of the ion source. During the experiment the radiometer was positioned at a vacuum window/flange 6 in. from the solar cell. The window material is quartz and transmits

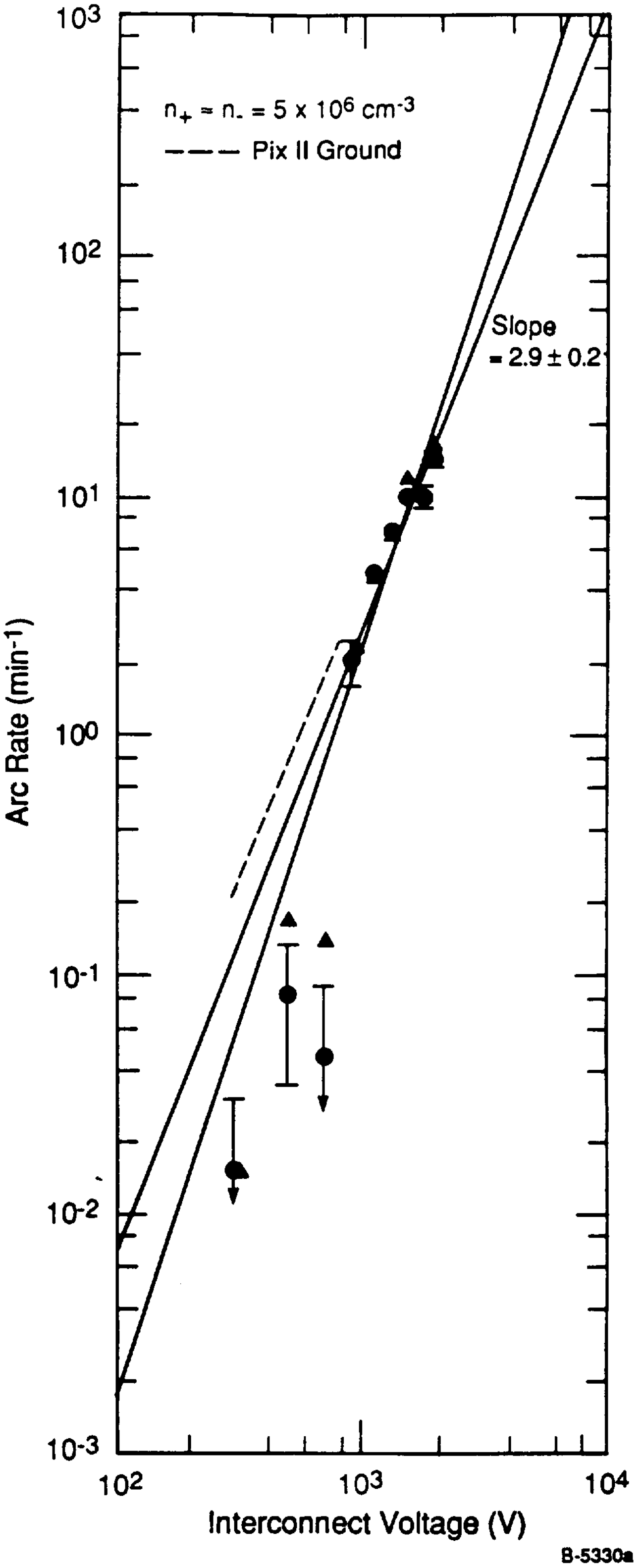

Figure 10. - Arc rate voltage dependence of exposed adhesive and interconnect leads.

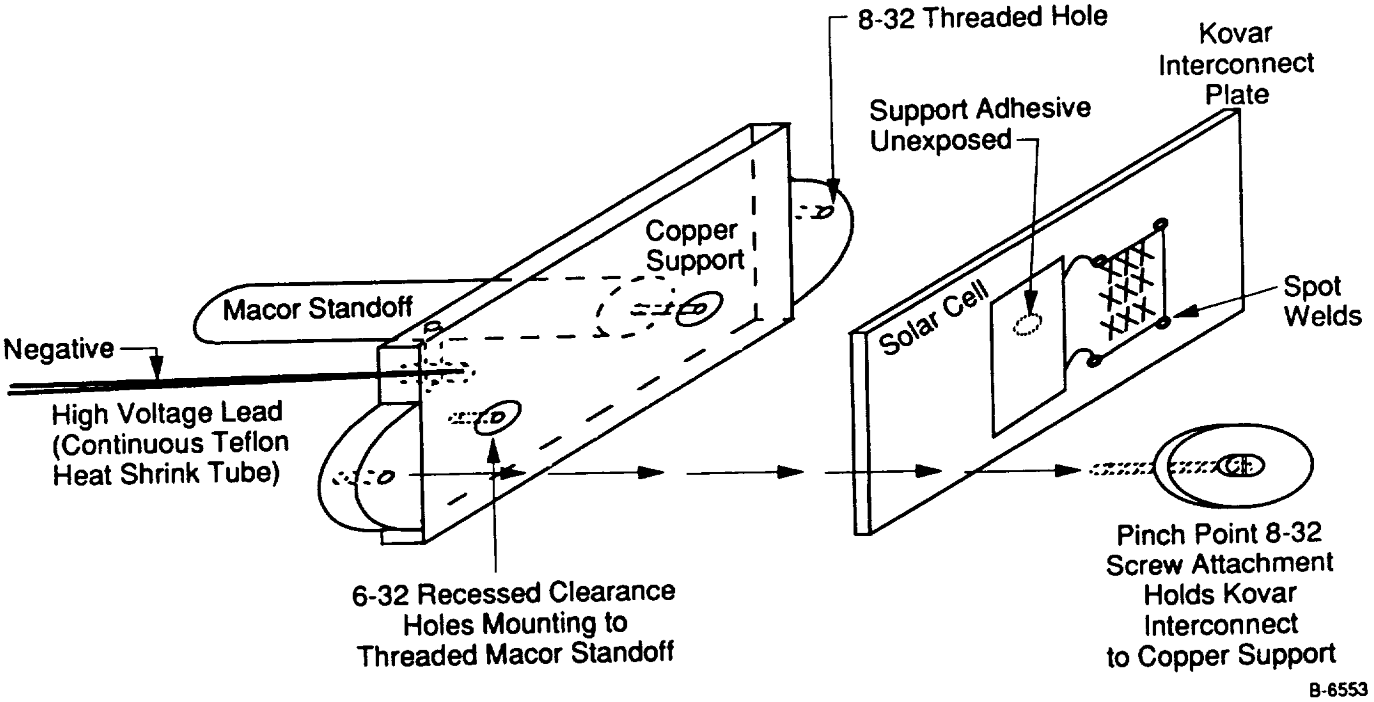

Figure 11. - Exploded view of new copper support/negative high voltage lead.

greater than 90 percent of the light in this wavelength region. Signal from the radiometer was passed to a Heath Zenith SD5000 computer digital scope (50 ohm input impedance) operated at its maximum real time acquisition rate of 25 megasamples/s. Data is stored in the PC-based scope and can be manipulated in a LOTUS® 1-2-3 spreadsheet. Arc events are captured by triggering the digital scope with the capacitively coupled arc sensor.

In addition to arc current flow, the change in bias voltage on the cell was recorded using a Tektronix model P6015 high voltage probe. This probe provides a 1000 to 1 attenuation of the (AC/DC) voltage with better than 100 kHz bandwidth. In single shot mode, at voltages of 1 kV or less, we were able to confirm a bandwidth of better than 8 MHz. This probe was attached to the negative high voltage interconnect on the atmospheric side of the vacuum feedthrough. For most of our testing the 3 pF of added capacitance due to the probe was insignificant.

2.2.6 Optical Multichannel Analyzer Spectrometer. - This detection system used a Princeton Instruments Optical Multichannel Analyzer (OMA) coupled to a Jarrell-Ash 1/4m monochromator to view and spectraly disperse emission from arc events. A 300 line/mm grating in the spectrometer allowed us to disperse the 200 to 400 nm region in one spectrum onto the 712 element diode array. This instrument possesses many advantages over a simple monochromator and PMT device. The most important is the multiplex advantage of detecting the dispersed light throughout the entire 200 to 400 nm region for each arc event. Although the detection sensitivity of the OMA is adequate, we were unable to measure any signal until the factor of 20 to 40 enhancement from larger circuit capacitance was implemented.

Our OMA experiments proceeded as follows. The diode array intensifier was gated on for 5 μs, as triggered by the output of the arc sensor through the digital scope. Some inherent delay time through the intensifier pulse circuitry caused the initial 300 to 400 ns of the light emission to be lost. This prohibits the collection of light from shorter duration arc events. Experiments consisted of co-averaging many arc events on the diode array followed by a background subtraction of an identical number of intensifier pulses without arc events. Wavelength calibration was obtained with spectra of well known Hg lines from a penlamp discharge source. Response corrections were evaluated using a standard lamp.

2.2.7 Intensified Array Camera. - Actual images of individual arc events were captured on the gated and image-intensified CCD camera system. The core of the imaging system is a PSI designed and built intensified CCD array camera. The CCD camera is a Model NXA 1060, manufactured by Amperex. A schematic diagram of the system is shown in Figure 12. Custom software was developed which permits asynchronous control of the camera and synchronization with the trigger source from the arc sensor. The intensifier is gated on coincidentally with the trigger pulse for 5 μs in order to capture the arc emission while eliminating unwanted background light. The camera system is calibrated against a known responsivity detector so that, at any gain level, it is possible to relate the A/D level of the pixel in the digital image to a number of incident photons. For this application the camera was coupled to a Nikon F/4.5 compound quartz lens system and a UG-5 UV transmitting filter to eliminate the unwanted visible glow of the hot tungsten filament.

2.3 Solar Cell Test Samples

Solar cell arcing tests were performed primarily on single 1 x 2 cm^2 silicon cells. These cells were supplied to the effort free-of-charge by Spectrolab Inc., a primary supplier of the 8 x 8 cm^2 cells to be used on the SSF array panels. A schematic diagram of the construction is shown in Figure 13. The cell is comprised of a 150 μm thick AR-coated fused silica cover glass attached to a 64 μm thick silicon cell with Dow Corning DC93-500 two-part RTV adhesive. This adhesive is a low volatility type which has been extensively characterized in connection with spacecraft contamination studies. The cover glass extends over the edge of the silicon cell on three sides by approximately 100 μm. A metallized interconnect tab is connected to the cell along the 2 cm axis for current extraction. The cover glass terminates where the current collection tab leaves the cell surface. A thin film of adhesive acting as a buffer between the tab and the edge of the cover glass. The base of the cell is coated with a multilayer metallization for bonding to the metallized tab on the next cell in the array series. A photograph of the cell is shown in Figure 14.

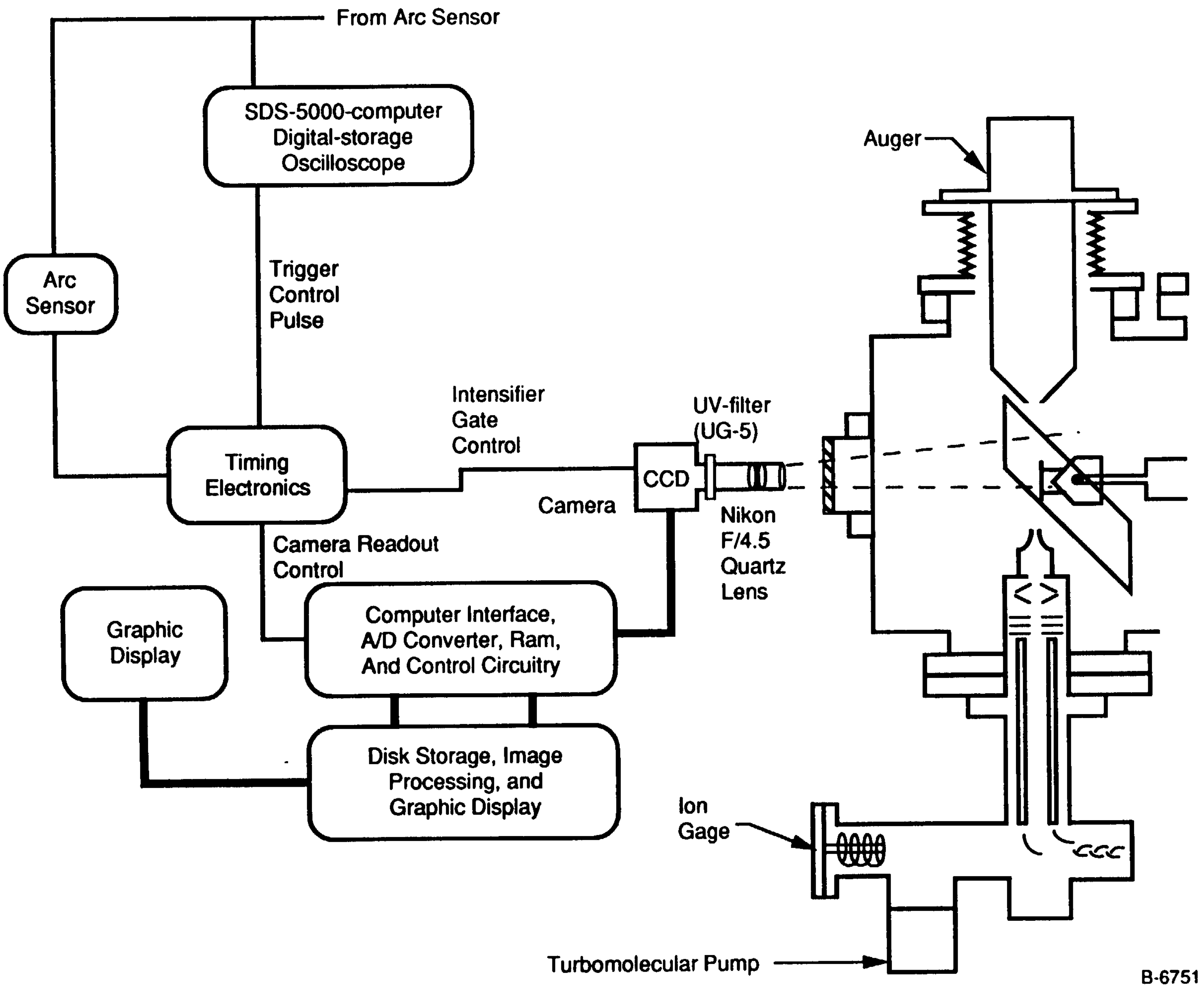

Figure 12. - CCD camera schematic.

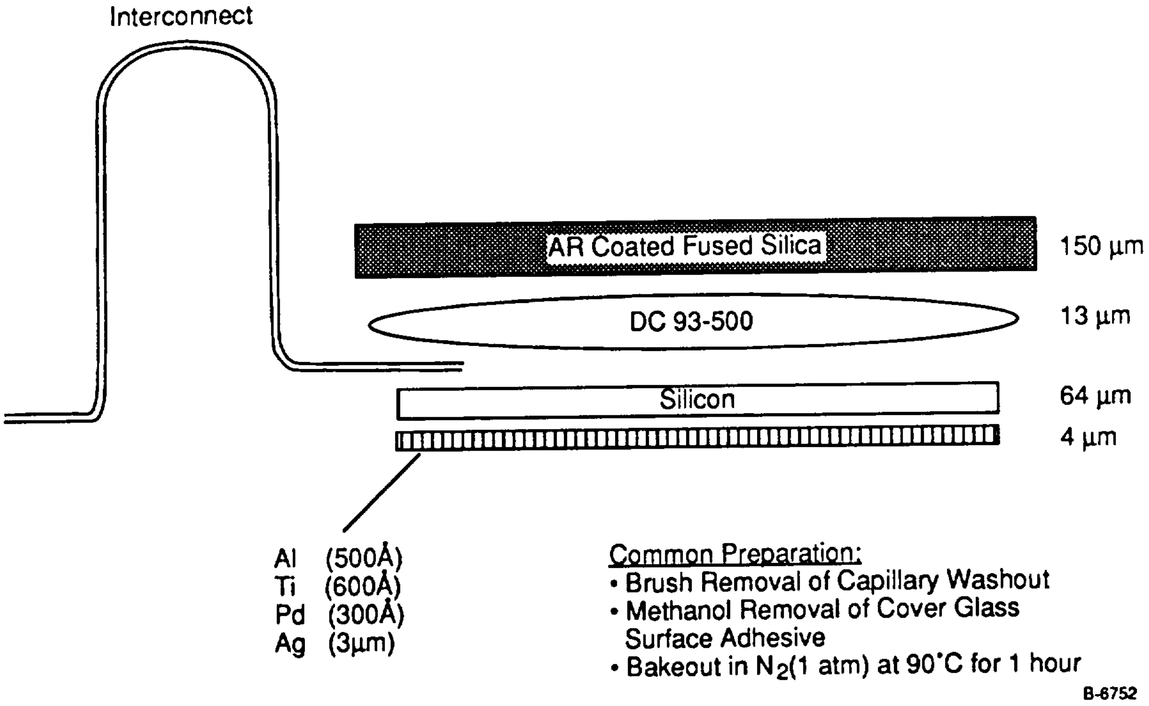

Figure 13. - Schematic diagram of Spectrolab 1 x 2 cm^2 solar cell construction.

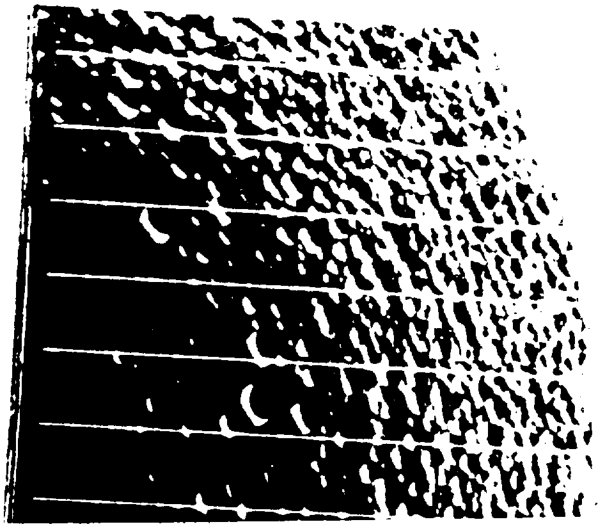

Figure 14. - Photograph of Spectrolab 1 x 2 cm^2 solar cell - top view.

The intersection of the plasma, the solar cell metallization or silicon, and the cover glass form a triple junction. These junctions are known to be a likely sites for high voltage arcing. An extensive examination of these cells was conducted to characterize these junctions. Figure 15 shows an expanded view of the underside of a typical solar cell, where the cover glass extends over the silicon cell edge, taken using a reverse contrast microscope. The black regions of the photograph show where excess DC93-500 adhesive has extruded from beneath the cover slip during fabrication. The adhesive has formed a jagged and somewhat irregular seal along the edge of the silicon. A similar type of construction is now being used on both the SSF 8 x 8 cm^2 array and the Advanced Photovoltaic Solar Array (APSA) cells. A recent inspection of the array edges on the 8 x 8 cells have shown approximate 70 percent of the cell edges are obscured by the excess adhesive.[23]

To investigate the effects of excess adhesive at these triple junctions a sample of the cells were modified by removing the adhesive. Several different techniques were tested to remove the adhesive. These included mechanical abrasion with small wire wheels, the use of small dental tools, and solvent removal. The use of wire wheels was effective at removing the excess adhesive but left small filaments of adhesive protruding from underneath the cover glass. Solvent removal using Dynasolve 220, a commercially available compound, was effective at removing the adhesive but the extent of removal was difficult to control due to the uneven distribution of the adhesive around the edge of the cell. Often the solvent would remove the adhesive from beneath the cover glass, which would not be acceptable for flight quality cells. However, for our operational purposes, these cells were acceptable and were used in the measurement program. In Figure 16 we show a view of the underside of a cell cleaned with Dynasolve 220. The treatment clearly reveals the silicon/cover glass junction and the extent of the, now clear, overhang.

Figure 15. Photograph of underside of Spectrolab 1 x 2 cm^2 cell.

Figure 16. - Photograph of underside of Spectrolab 1 x 2 cm^2 cell cleaned with Dynasolve 220.

Additional concerns regarding the role of adhesives in arcing led us to conduct tests on a silicon cell in which the cover slip was attached using an electrostatic bonding process. This cell was furnished by the Advanced Power Technology group at Boeing. The cell was a prototype which had no attached interconnect and a cover glass which had not been correctly placed on the silicon, leaving two exposed triple junctions. This cell is shown schematically in Figure 17 and a photograph is included as Figure 18. A limited range of tests were conducted using this cell.

2.4 Electrical and Optical Characteristics of Solar Cell Arcs

The combined use of electrical and optical diagnostics for the detection of arcs produced an interesting correlation. Typical current and voltage traces derived from the arc sensors are shown in Figures 19 and 20. The current sensor trace (Fig. 19) shows a discharge of approximately 2 μs in duration which is highly structured. The corresponding trace for the voltage sensor reproduces the starting and terminating points of the arc but fails to reproduce the structure observed in the current trace, due to the limited temporal response of the voltage sensor. For this specific measurement the cell bias voltage was -1000 volts and peak currents during the arc reached 30 mA. Note that the voltage trace indicate a reduction in the cell voltage from -1000 volts to approximately -300 volts at the termination

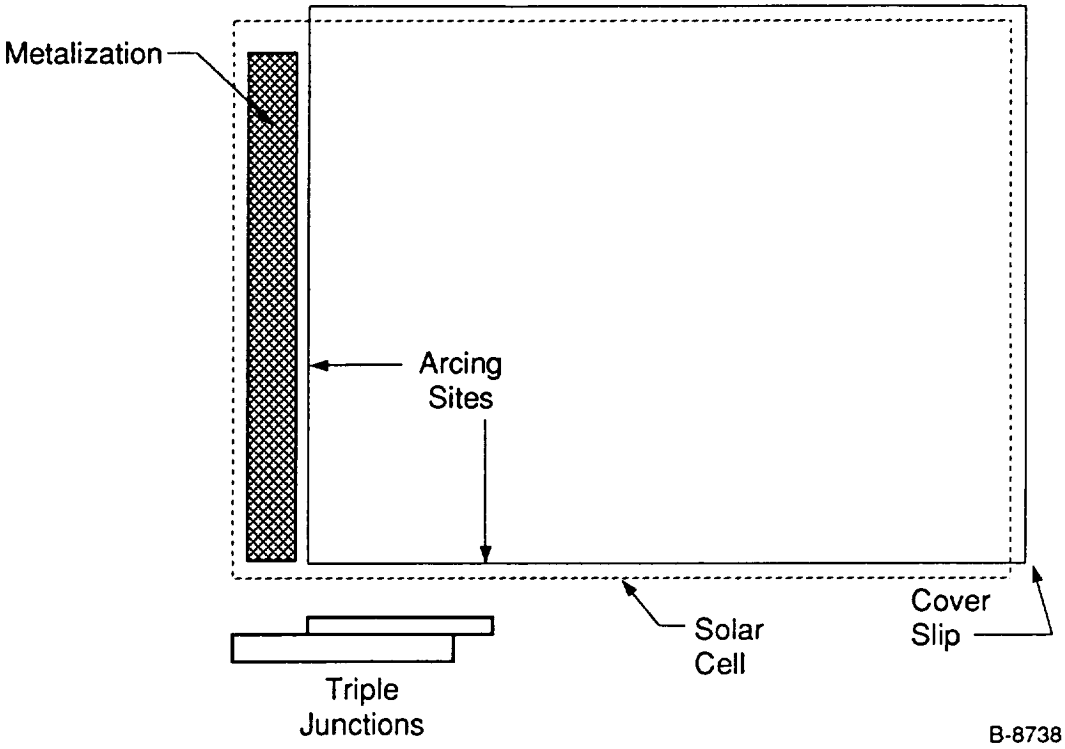

Figure 17. - Schematic diagram of Boeing electrostatically-bonded solar cell.

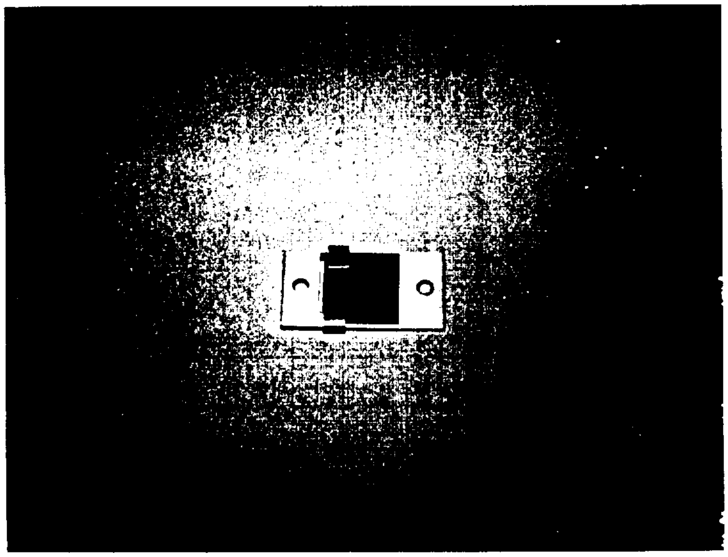

Figure 18. - Photograph of Boeing cell in Kovar mount.

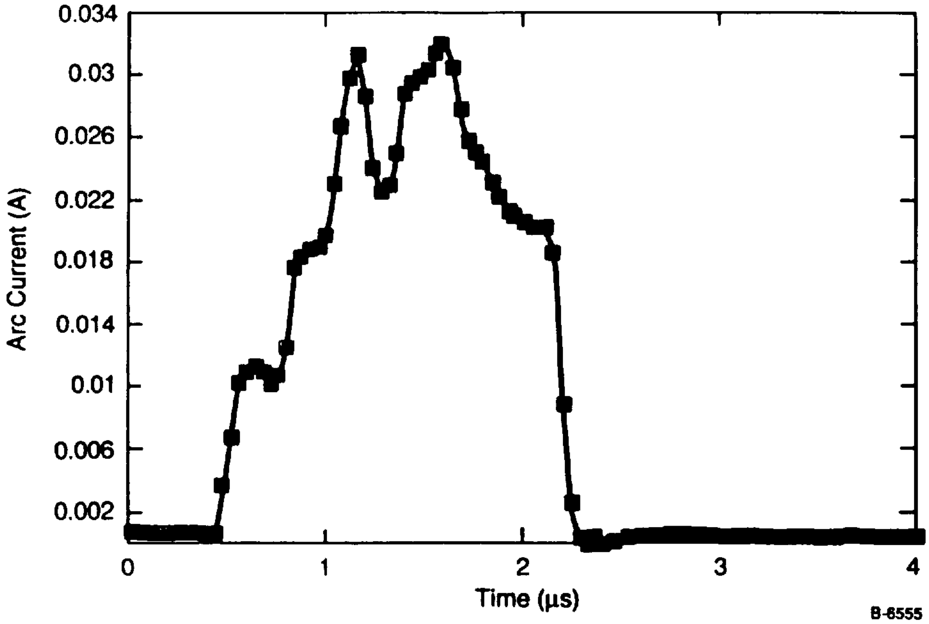

Figure 19. - Current flow to the arc event measured by a capacitively coupled arc sensor.

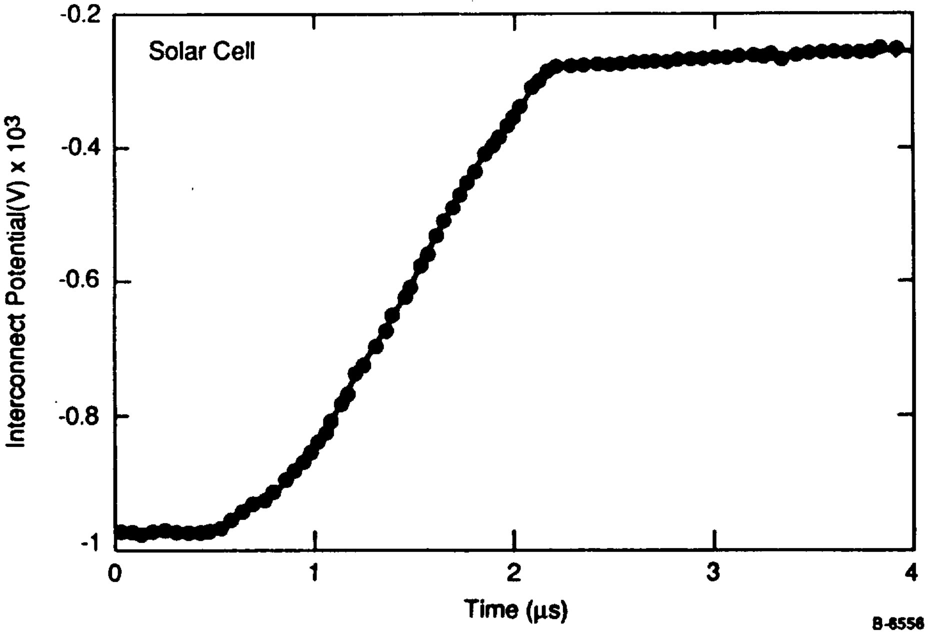

Figure 20. - Change in interconnect potential as measured by the Tektronix high voltage probe.

to approximately -300 volts at the termination of the arc. The arcs observed from these cells span a range of currents and cell voltage reductions. The arc current can be related to the cell voltage drop through the relation

$$\Delta Q = C \, \Delta V$$

where ΔQ is the total charge transferred in the arc, ΔV is the total voltage drop on the cell during the arc, and C is the capacitance of the arc sensor measurement system. Figure 21 shows the time running integral of the charge transferred for a single arc. The data exhibits good correlation between the charge and the voltage sensors. Figure 22 shows the integral of the charge transferred in an arc as a function of the total voltage drop. The slope of the line formed from the plot, 53 ± 0.05 pF, agrees quite well with the measured capacitance of the arc sensor system, 52 pF.

The solar cell biasing system included the capability to add additional capacitance to the cell, in order to simulate the response of a much larger array of cells. This capacitance could be varied from the inherent capacitance of the system of approximately 70 pF to a total capacitance of nearly 800 pF. A significant observation of the arc electrical characteristics was that the arc duration was insensitive to added capacitance but that the arc current scaled with added capacitance.

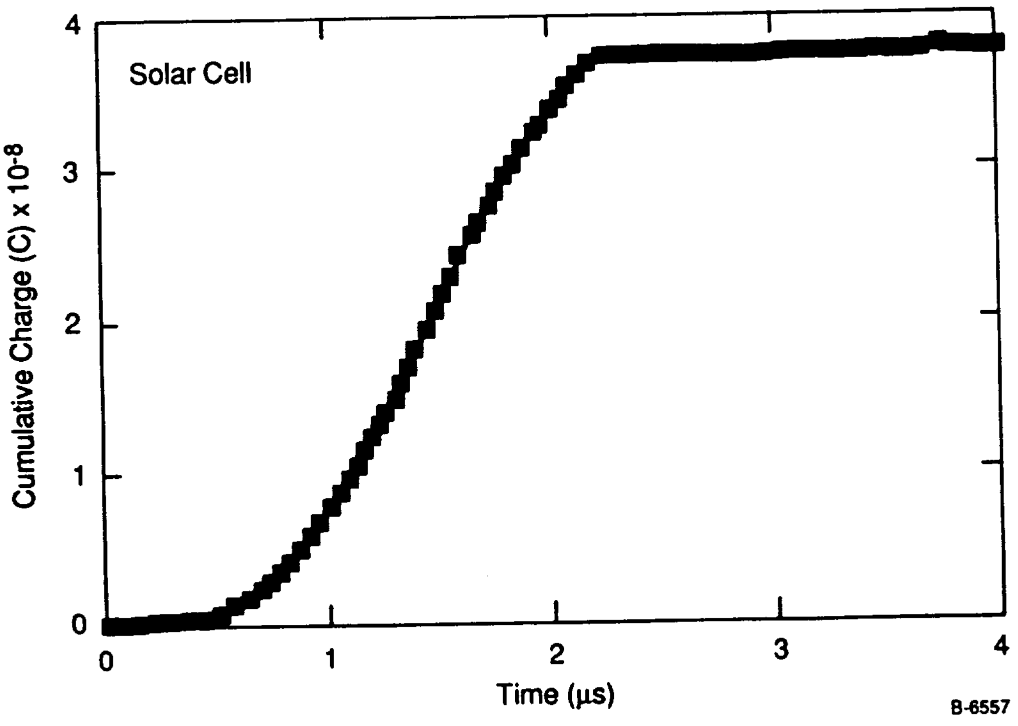

Figure 21. - Integral of current flow of arc event shows remarkable similarity to the potential drop curve.

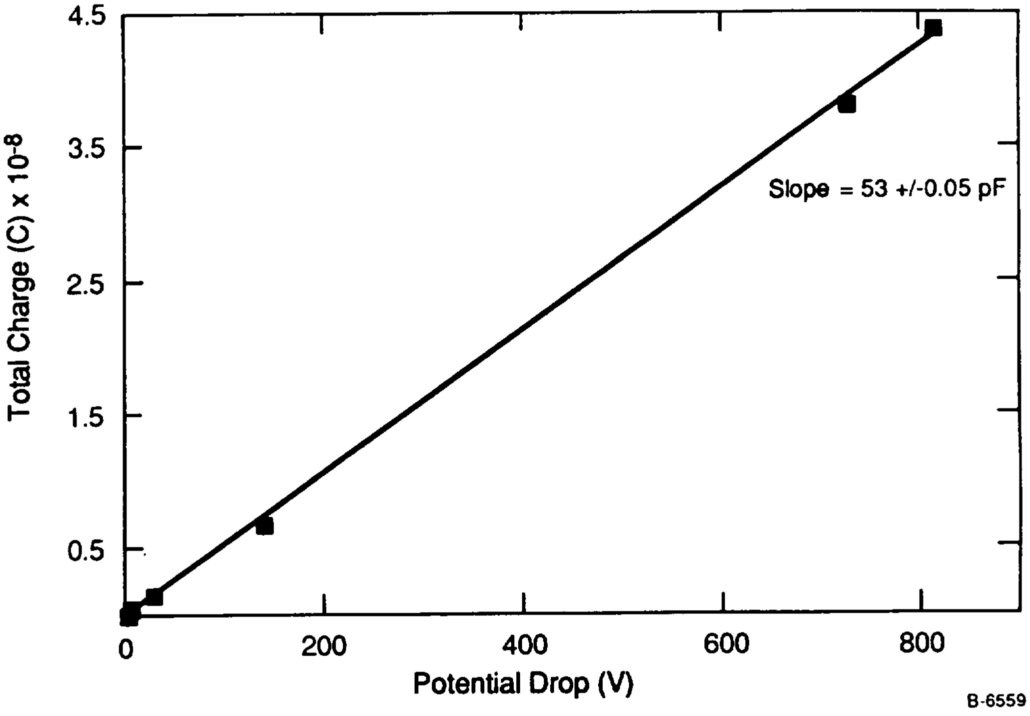

Figure 22. - The correlation of the measured charge dissipated in an arc event to the interconnect potential drop verifies the arc sensor capacitance.

Arc data recorded simultaneously using both the arc current sensor and the UV radiometer reveal a remarkable correlation between the two phenomenon. Figure 23 is a scaled overlay of arc temporal evolution as seen by both sensors. The sensors reproduce both the temporal duration of the arc as well as the fluctuations in arc intensity. Similarly, signal from the UV radiometer shows a linear correlation with voltage drop on the solar cell interconnect. This data is presented in Figure 24 for two applied cell capacitances, 70 and 780 pF. Since arc current is also linearly correlated with cell voltage drop, a linear correlation exists between arc current and optical emission from the arc. The correlation of arc current with UV emission intensity remains linear with interconnect voltage drop at higher capacitances. However, the efficiency with which UV photons are produced changes with added capacitance. At a cell capacitance of 70 pF UV photons are detected with an efficiency of 1.1×10^{-4} per electron transferred in the arc. When the cell capacitance is increased to 780 pF, the efficiency increases to a value of 2.3×10^{-4} per electron.

Two distinct conclusion can be derived from the optical emission data. The first conclusion is that the emission is derived from a region which is thin target for the electrons emitted from the arc. In a thickly absorbing region the optical emission would scale with the discharge energy, which is a quadratic function of the discharge voltage drop. The second, somewhat less substantiated conclusion, is that some fraction of the emitting species are produced from electron excitation of neutral species ejected from the arc site. This is

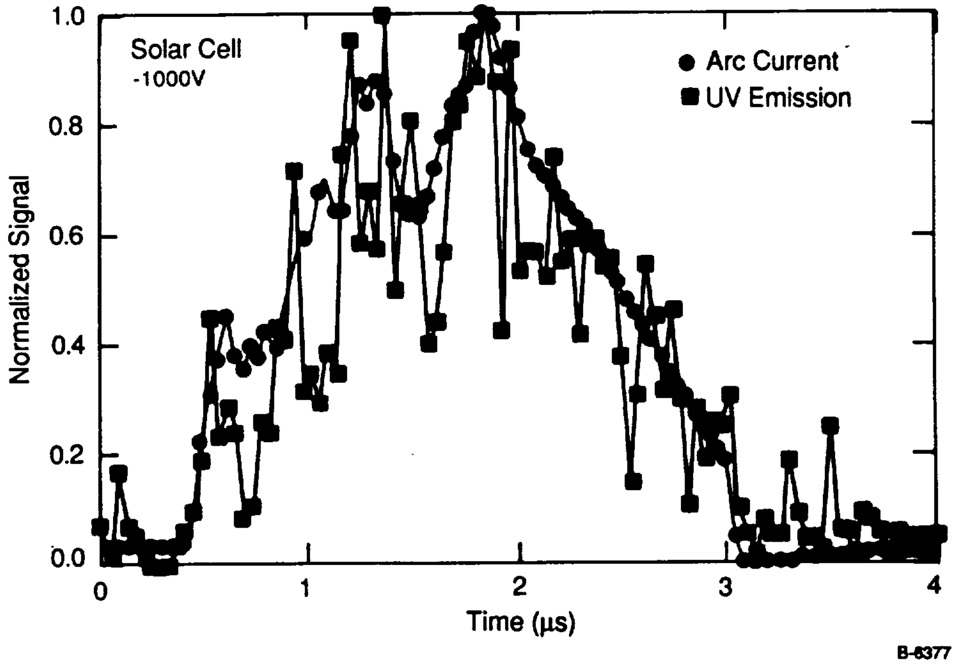

Figure 23. - Overlay of arc temporal evolution viewed by both arc current and UV light sensors

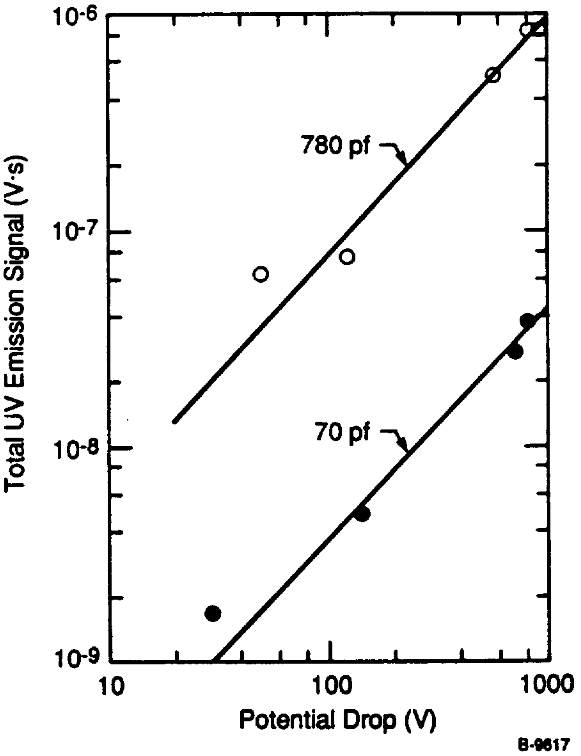

Figure 24. - Correlation of UV light emission with interconnect potential drop when circuit capacitance is increased from 70 to 780 pF.

suggested by the change in photon production efficiency with discharge energy. The production of a locally higher gas density by the higher energy arc, which remains thin for electron excitation, would result in an apparent increase in the photon production efficiency while maintaining the linearity of the emission with arc current. The data supports the idea that arc emission can be used as a quantitative emission of arc strength. **Optical emission from arcs could be used in an imaging configuration to remotely monitor arc rate, strength, and location on large space structures in orbit.**

2.4.1 Arc Spatial Imaging. - The use of an imaging system to monitor arc location played a key role in many of the conclusions drawn from our efforts. The imaging system was previously described in Section 2.2. Prior to commencing these experiments we had believed that a primary arcing site on the cell would be the region where the protective cover glass met the exposed metal interconnect. This site forms a triple junction. Images of arc originating on the Spectrolab 1 x 2 cm^2 silicon cells showed that arcs were confined to the other three edges of the cell. These edges were all characterized by a cover glass which extended beyond the edge of the cell by approximately 100 μm and the presence of excess adhesive extruded from the cell/cover glass interface. Figures 25 and 26 show arcs observed at the lower edge of a cell. Figure 25 is an image of a typical arc, showing that the arc occurs over a spatial extent of approximately 500 μm in diameter.

In Figure 26 two distinct arcs are observed spatially within a period which is characterized by a single arc pulse electrically. Since the gate duration on the camera

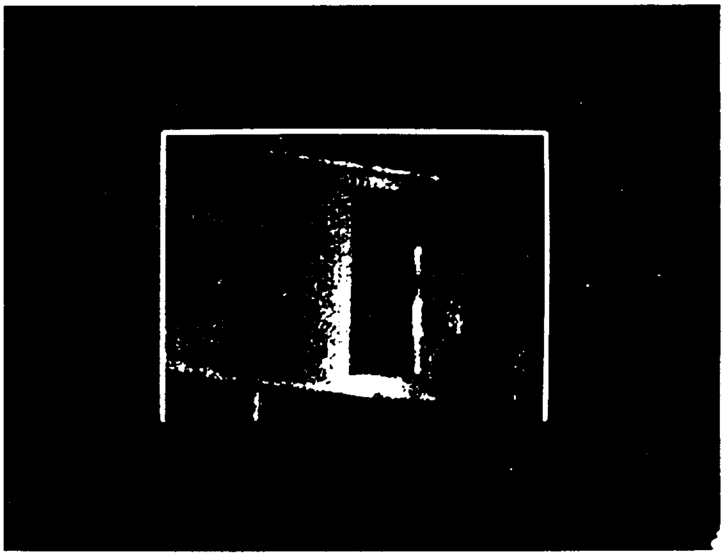

Figure 25. - Typical CCD camera image of solar cell arc.

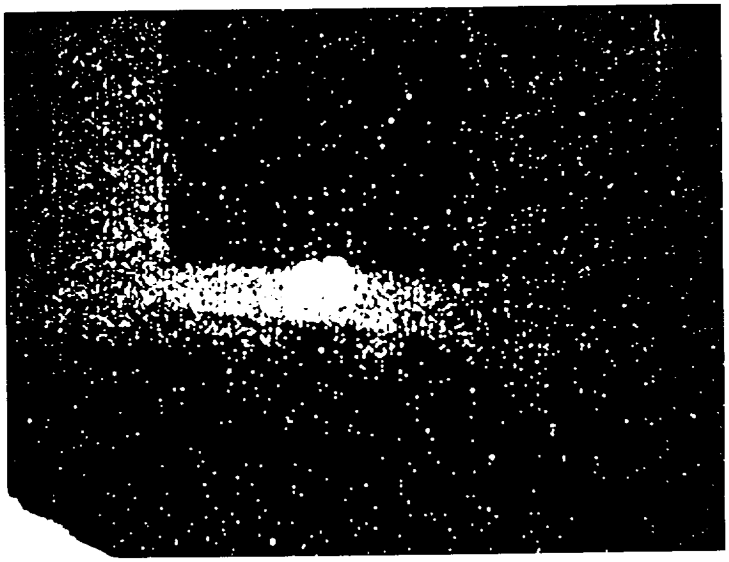

Figure 26. - CCD camera image of double arc on lower edge of cell.

intensifier is short (5 μs) compared with the period between arcs (typically 100 ms), it is unlikely that the camera simple observed two unrelated arc events occurring simultaneously. A more appropriate explanation is the triggering of a nearby arc site by the first arc event. This is an important observation since it is evidence for a mechanism of arc propagation beyond the initial site. It would be reasonable to expect that the radius over which this triggering event would occur could be related to the energy dissipated in the arc, since the arc spatial extent is determined by the range over which neutral and charges species are ejected from the substrate. **Hence, the inherent capacitance of that portion of the array coupled to the arc may have an impact on arc spatial extent through the triggering of arcs on other, electrically isolated portions of the array.**

2.4.2 Arc Spectral Imaging. - Spectra of the solar cell arcs were recorded for the 1 x 2 cm^2 spectrolab cells, as received. Figure 27 shows a weak spectrum of an arc recorded with a total system capacitance of 780 pF at a bias of -1 kV. Emission from the O-H ($A^2\Sigma$-$X^2\Pi$) transition at 308 nm is evident in the spectrum, even at low signal levels. Strong features at 350 nm and 380 nm are also observed in the spectrum. The breadth of the spectral features makes identification of the emitting species difficult. Strong emission lines are present in this region from atomic cobalt, nickel, iron, and magnesium. Emission spectra were also recorded from a solar cell arc with a capacitance of XXX pF biased at a voltage of -3 kV. Much higher signal levels are observed in this spectrum. This spectrum is shown in Figure 28. Features occuring at 328 nm and 338 nm respectively are assigned to emission from atomic silver on the ($^2P_{3/2}$, $^2P_{1/2}$ - $^2S_{1/2}$) transition, which is extremely strong. Other

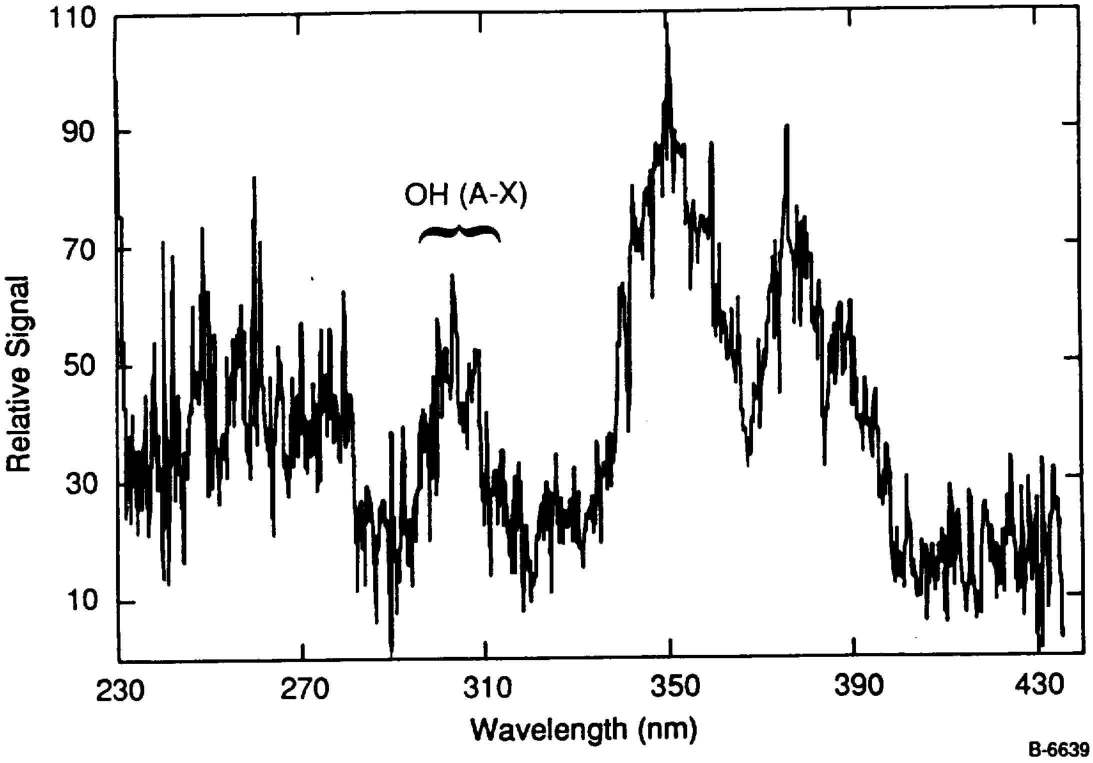

Figure 27. - Emission spectrum from low applied capacitance solar cell arc.

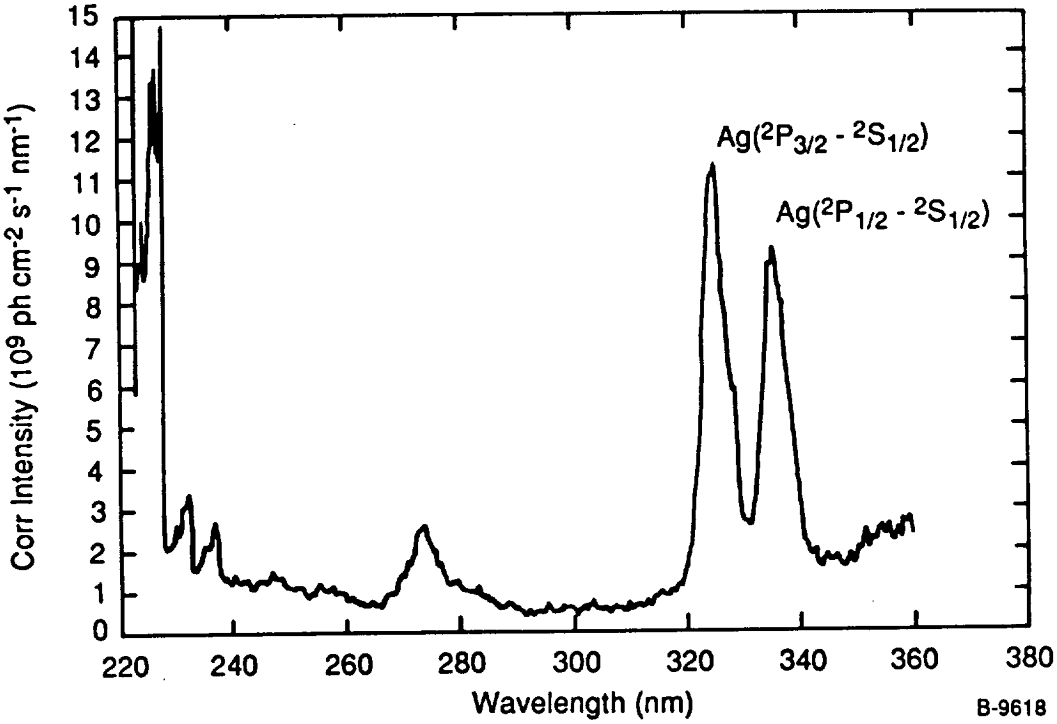

Figure 28. - Emission spectrum from high applied capacitance solar cell arc.

features are observed in the 220 to 240 nm region and at 273 nm. These cannot be conclusively assigned but may be due to molecular species. The observation of emission from Ag is significant, since all of the metallic surfaces of the solar cell arc Ag-plated for bonding purposes. Optical arc sensors based on observations at this wavelength would most likely be highly sensitive.

2.5 Environmental Effects on Arcing

Our observations also indicated that the ambient environment of the solar cell had an impact on the apparent arcing rates. The previously noted cell conditioning effects are a component of these environmental effects. Figure 29 shows the impact of solar cell heating on the arcing rate. This heating is accomplished indirectly, through the radiant heat load placed on the thermally isolated cell by the plasma neutralizing filament in the Kaufmann ion source. After thorough degassing of the solar cell in the UHV chamber (base pressure 2 x 10^{-9} torr) the cell was subjected to both the radiant and plasma loading from the Kaufmann source. The data shows a distinct decrease in arcing rate with exposure time. During this period the solar cell equilibrates to a temperature of 85 degrees Celsius.

Experiments were conducted to isolate the effects of thermal processing from plasma exposure. After cycling the cell back to atmospheric pressure with room air, the cell was again placed in the vacuum chamber for testing. In previous cycling of this sort the cell arcing rate had returned to its initial, pre-exposure, value. The cell was again exposed to the Kaufmann source operating in a manner, which did not allow plasma production. This technique allowed for the normal radiative heating of the cell without the corresponding plasma exposure. In a series of tests, the cell was heated in vacuum for a fixed period of time, following which plasma exposure was initiated and the cell arc rate was determined. Figure 29 also shows the results of such an experiment for which the cell was heated for periods of 45 minutes and 3 hours prior to arc rate measurements. The data reveals a reduction in the initial arc rate of the cell by a factor of ten for 45 minutes exposure and greater than a factor of 100 for 3 hours exposure. In fact, after three hours of exposure the cell arc rate fell below the practical detection limit of 0.1 arcs per minute. Once thermally conditioned and confined to a vacuum environment, the arc rate for these cell remained below detection limits for periods ranging from several days to weeks. Exposure to room air immediately established the pre-exposure arcing behavior while exposure to comparable amounts of pure O_2, N_2, Ar, or CO_2 had no impact on the measured arcing rates.

The data cited above indicates an airborne constituent common to both the natural air and UHV environment may play a role in cell conditioning. Furthermore, the evidence from the thermal processing studies shows that the contaminant is tightly bound to the cell, since a significant temperature increase is required to effect its removal. A strong candidate for the interacting species is H_2O. Clearly common in room air, H_2O is also the primary contaminant in UHV chambers, albeit at a much reduced level. These results are confirmed by mass spectrometer analysis of the UHV chamber background gas, which is largely a

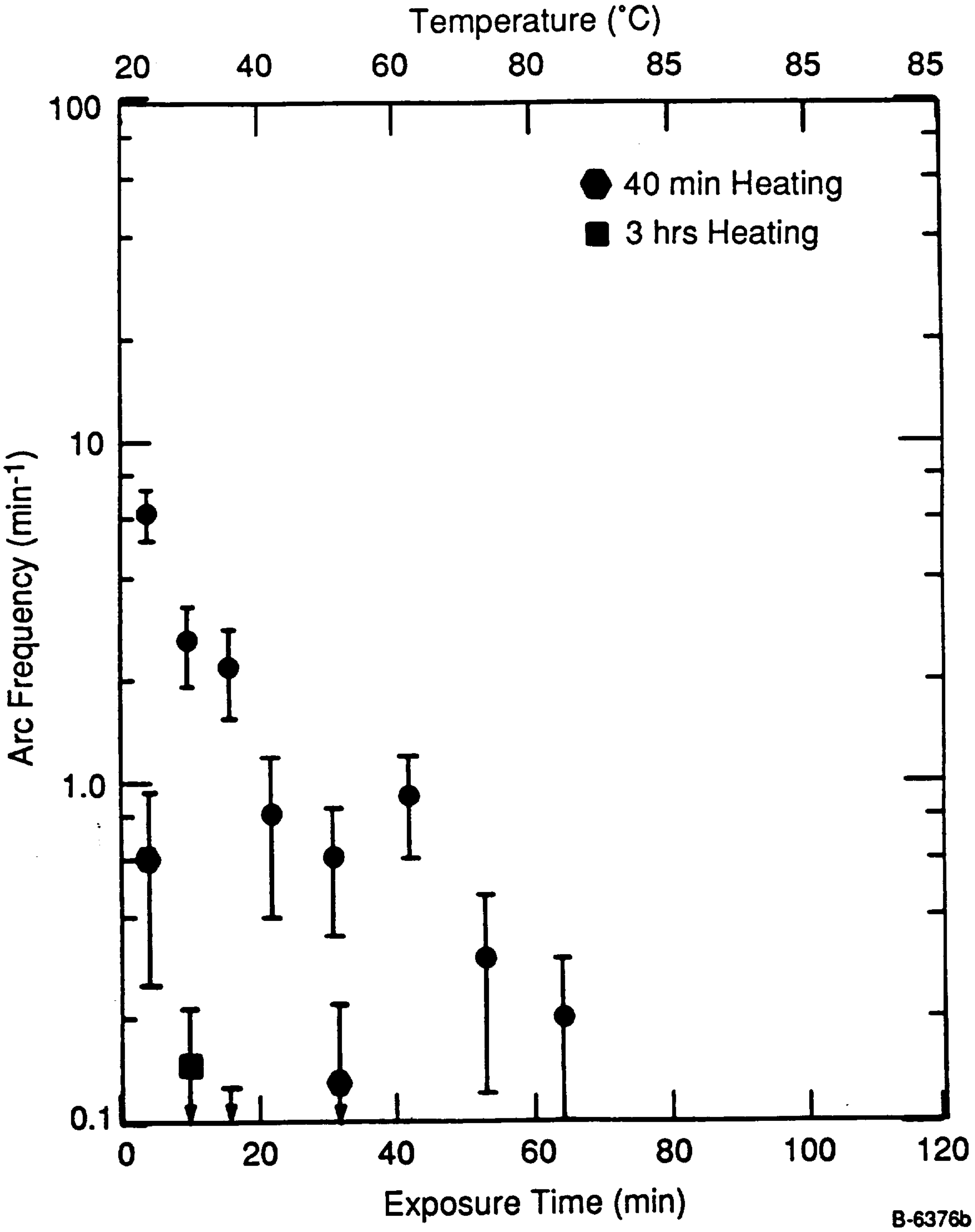

Figure 29. - Conditioning of solar cell arc frequency with plasma exposure time, showing impact of cell heating on measured arcing rates.

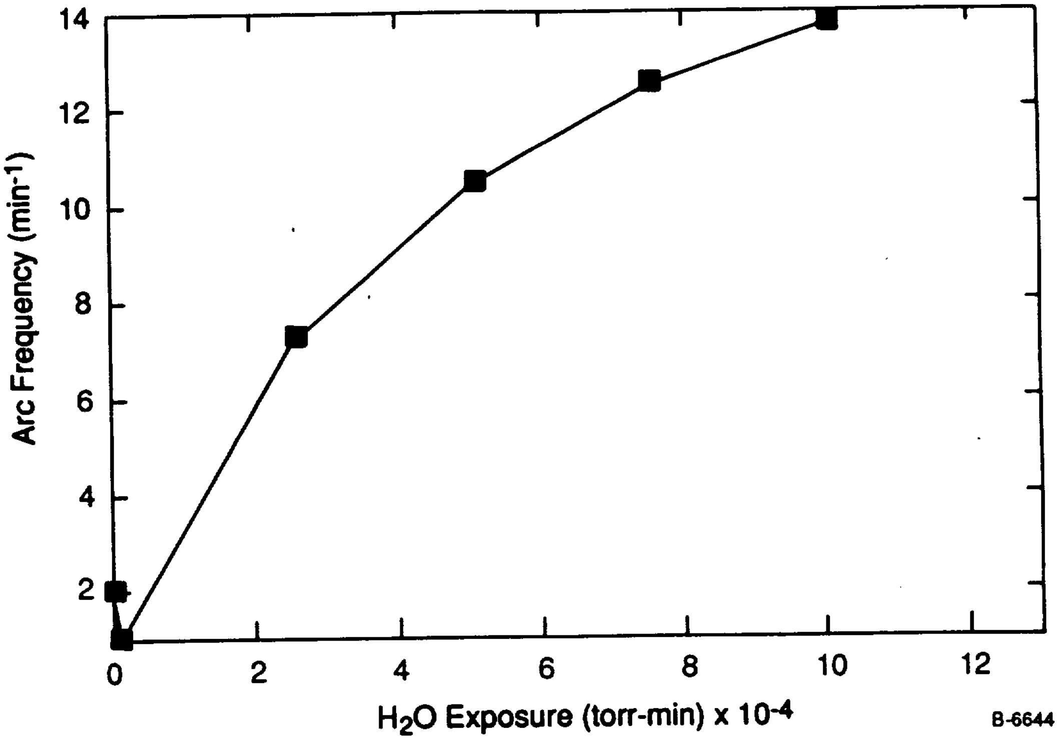

Figure 30. - Effect of water vapor exposure on observed arc rate.

mixture of H_2O and CO_2. The background water vapor concentration in the chamber is enhanced by approximately a factor of 100 during Kaufmann source operation, to a pressure of 2×10^{-7} torr. The enhancement is a result of thermal desorption of water from the walls by the charge neutralization filament. By comparison, the equilibrium vapor pressure of H_2O at room temperature is approximately 18 torr. The relative amounts of H_2O present in these two regimes accounts for the disparity in deconditioning times for the cell.

Confirmation of the role played by H_2O vapor was obtained by enhancing the exposure of the cell to the vapor in a controlled manner. In these experiments the chamber was equipped with a variable leak valve through which a thoroughly degassed flow of water vapor could be passed to the cell. Cells were conditioned and held at 85 degrees until the previously noted reduced arcing rate was obtained. The cell was then subjected to successive dosings of 2.5×10^{-4} torr-minutes, i.e. the chamber was brought to a pressure of 5×10^{-5} torr for a period of 5 minutes. Between each exposure the plasma source was activated and the cell arcing rate was measured. The data obtained from these successive exposures is plotted in Figure 30. The data shows a progressive increase in the cell arcing rate from the conditioned state to an asymptotic level characteristic of the cell prior to conditioning. This data shows clear evidence of the role played by H_2O in promoting arcing. Note that the interaction of the water vapor is with the cell and not with the plasma, since simultaneous exposures were not employed in these measurements. Furthermore, the data supports the notion that the water is held in depth within a component of the cell. This is likely because the desorption rate of water from the surface of the cell is fast compared to the observed conditioning times.

The role of the extruded adhesive layer found at the silicon/cover glass plasma triple junction was also illustrated in our measurements. A solar cell which had been modified to remove the extruded adhesive (using the solvent removal method) was subjected to the same set of experiments described above for the unmodified cells. Cells which had been modified in this manner showed none of the conditioning behavior observed for as-manufactured cells. From the inception of testing these cells exhibited an arc rate below the measurement threshold. Furthermore, treatment of the cells with additional water vapor did not raise the arcing rate. In later measurements cells which had been processed to remove excess adhesive using mechanical abrasion were tested. These cells did exhibit considerable conditioning effects. Most likely, these differences can be accounted for by the presence of small hair-like adhesive filaments remaining from the mechanical abrasion process. It is likely that these filaments are the sources of arc sites at these triple junctions and their number may be increased by this form of adhesive removal.

2.6 Plasma Scaling

Arcing rate measurements on PIX II had shown a correlation with plasma density. A scaling of arcing rate with plasma density is also predicted by the theory developed by under this contract. The theory will be reviewed in Section 5. Out laboratory tests were conducted to explore the bounds of this effect. The UHV chamber and Kaufmann plasma source were employed in their usual configuration. The test article was an array of six (6) Spectrolab 1 x 2 cm^2 cells mounted on a Kovar plate. These cells were used without removing the adhesive from the edges of the cells but were conditioned by prolonged plasma exposure at a bias of -1 kV. Tests were conducted at a bias of -1 kV. The conditioning process was continued until the arcing rate ceased to change for several observation periods. The plasma scaling experiments were conducted by varying the operating pressure and ionization characteristics of the Kaufmann source. The planar Langmuir probe was used to determine the plasma density. Figure 31 shows the variation in arcing rate obtained as a function of plasma density from 1.5×10^6 to 6.5×10^{-6} cm^{-3}. The arcing rate shows a linear correlation with plasma density over this range. In Section 5 we will compare this data with theoretical predictions of the plasma sealing conducted under this program.

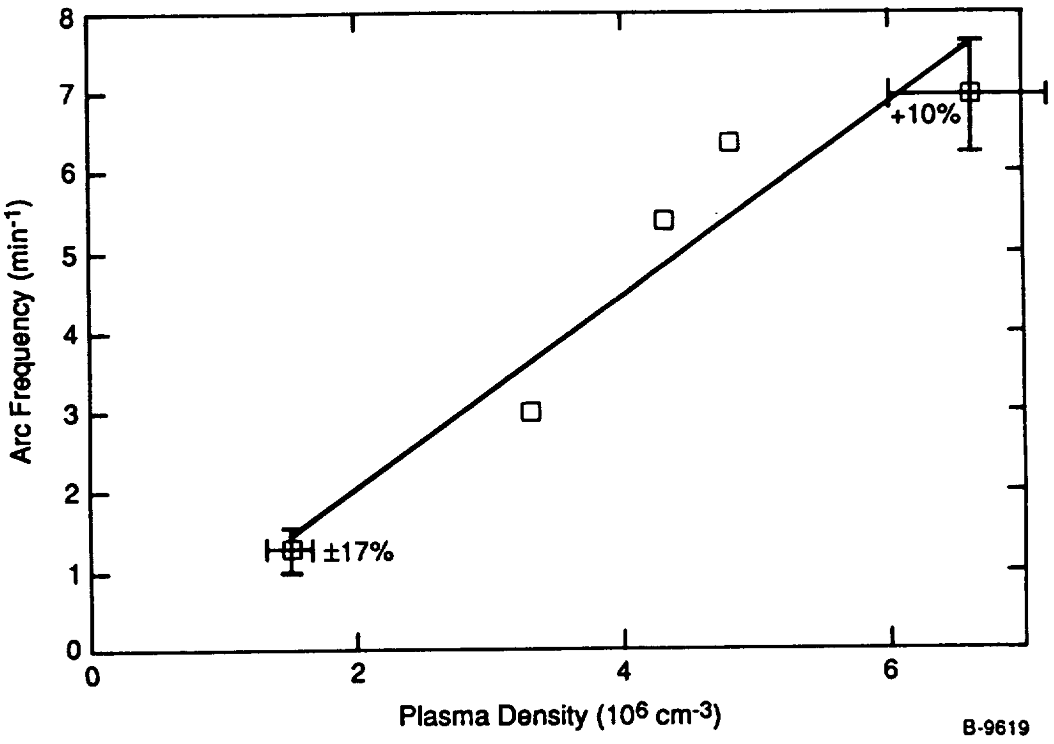

Figure 31. - Scaling of solar cell array arcing rate with plasma density at a bias of -1 kV.

3. ADHESIVE/PLASMA INTERACTIONS

Despite extensive investigations into the nature of the physical interaction between the plasma, adhesive, and water vapor, we have been unable to identify conclusively a mechanism which would explain their relationship to arcing phenomenon. As mentioned previously, the DC93-500 is a low outgassing two part room temperature vulcanizing (RTV) adhesive. Unlike commonly used RTV's, DC93-500 solidifies using a form of vinyl polymerization which leaves no volatile byproduct. Other RTV adhesives eliminate methyl alcohol as a product of the polymerization process. Specifications provided by Dow Corning[24] indicate that water absorption by the adhesive is less than 0.1 percent by weight. We can compare this water absorption level with the amount of H_2O impinging on the bead of adhesive found along the edges of the solar cell during our dosing experiments. Using simple kinetic theory we can show that total amount of water impinging on a 1 cm length of the cell edge is approximately 9×10^{-7} grams. The mass of a bead of adhesive approximately 25 μm in diameter, 1 cm in length, is 5×10^{-6} grams. Hence, sufficient water impingement can occur during one of our dosing experiments to saturate the adhesive if the absorption probability is approximately 0.005.

We conducted experiments to determine the impact of water absorption on the resistance of the thin films of the adhesive. Films of adhesive approximately 200 μm in thickness were deposited on a Pyrex glass plate. Two rectangular electrodes were then placed on top of the adhesive film, leaving an exposed area of dimensions 0.85 x 2.5 cm. The configuration is shown schematically in Figure 32. The plate was then mounted on the

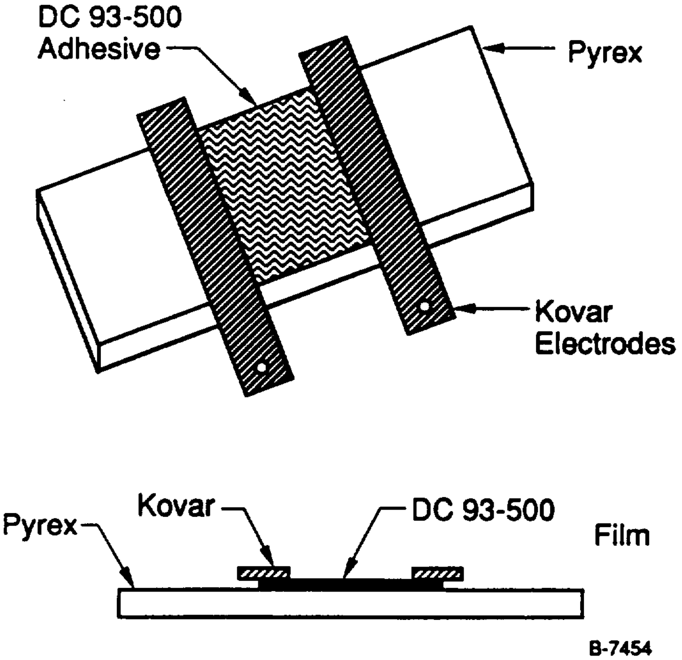

Figure 32. - Schematic configuration of adhesive film resistance measurement.

manipulator in the UHV chamber with leads attached to each of these electrodes. An external circuit was used to determine the resistance of the film in vacuum. A bias was applied to the film using a high voltage DC power supply. A sensitive current amplifier (Ithaco Model 1211) was connected in series with the power supply and the film to measure the current flow through the film. Typically, the film was biased to approximately 500 volts.

Bulk resistances measured for the film were in the 10^{13} to 10^{14} ohms. The resistance of the film was determined upon initial introduction to the chamber and after 3 hours of radiative heating using the charge neutralization filament on the plasma source (no plasma flow). During this time the film rose to a temperature of 85°C. No change in the resistance of the film was noted. Introduction of water vapor to the chamber at dosing levels similar to those employed in the solar cell measurements also produced no change in the film resistance.

Synergistic effects involving both plasma and water vapor exposure were also examined. In a series of experiments conducted using the plasma source, the film was exposed to plasma bombardment at increasing plasma energies. Figure 33 through 37 show the change in film resistance observed during exposure to the plasma at energies of 40, 100, 200, 300 and 500 eV. In each experiment the film was exposed to the plasma source for a fixed period of time. At intervals during the exposure the resistance of the film was determined. The plasma source was deactivated during the resistance measurement. The same film was used for each measurement and the measurements were conducted in order of increasing beam voltage.

Two distinct effects were noted in making these measurements. First, the resistance of the film decreases markedly on exposure to the plasma. The magnitude of the resistance loss is proportional to the incident ion energy. At low voltages the film resistance reaches an asymptotic value during the exposure period, while at higher voltage a steady state condition is never attained. The second effect observed was the recovery of the film resistance following the termination of plasma exposure. At low beam voltages the recovery period was rapid, resulting in a slow upward drift in the value during the measurement period. This drift is noted as the shaded regions in Figures 33-35. At higher voltages characteristic recovery times ranged from tens of minutes to days under ambient vacuum conditions. Two examples of this phenomenon are provided in Figures 38 and 39 for ion energies of 40 and 100 eV. Exposure of the film to room air at 1 atm pressure results in a somewhat enhanced rate of recovery of the original resistance value of the film, as does dosing of the film in situ with water vapor. We note that measurements of the film potential during the plasma dosing measurements showed no evidence of film charging. The mobility of the ions and electrons in the plasma are expected to act to maintain the film potential close to that of the plasma.

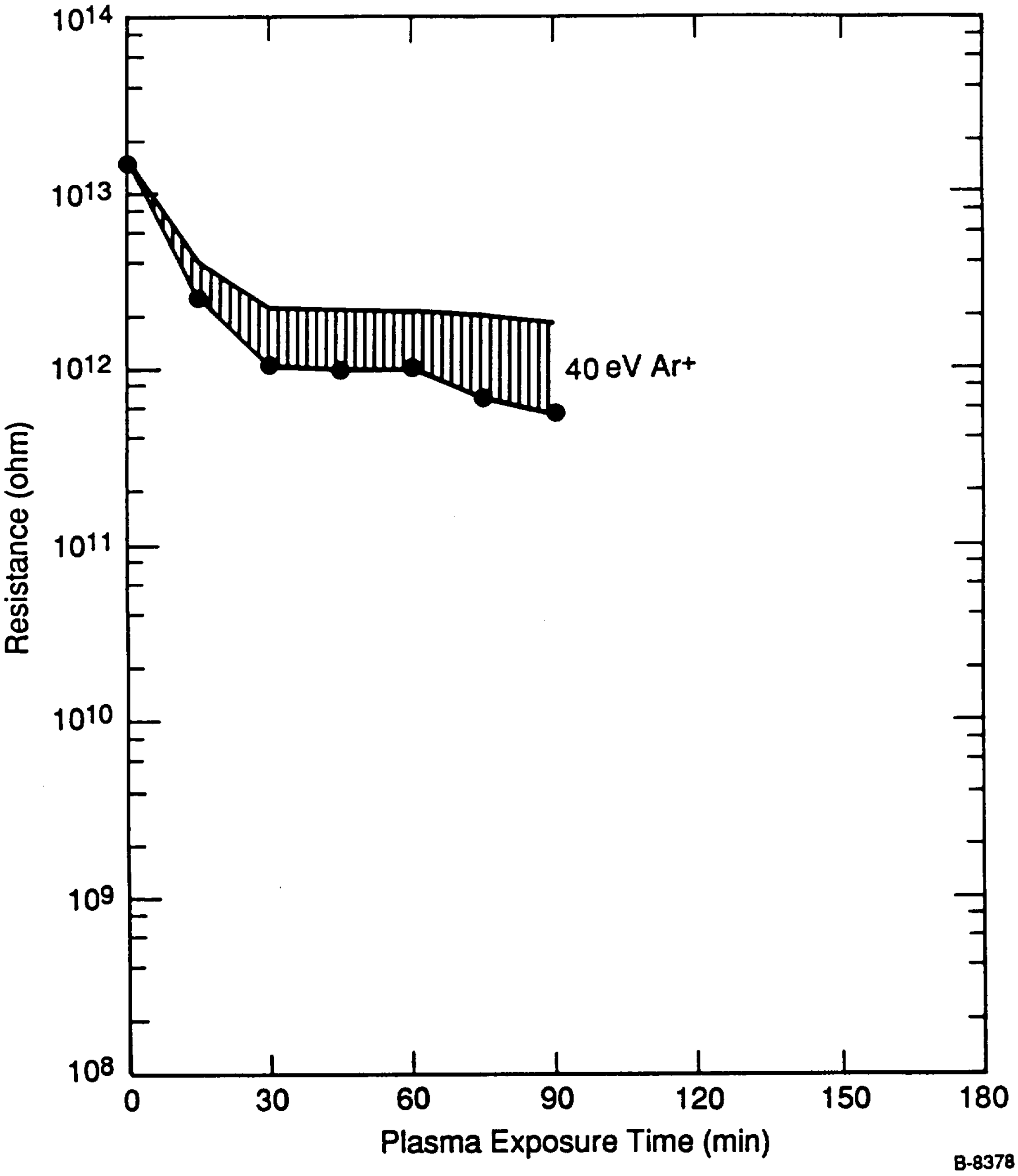

Figure 33. - Adhesive film resistance as a function of 40 eV Ar^+ Plasma Exposure

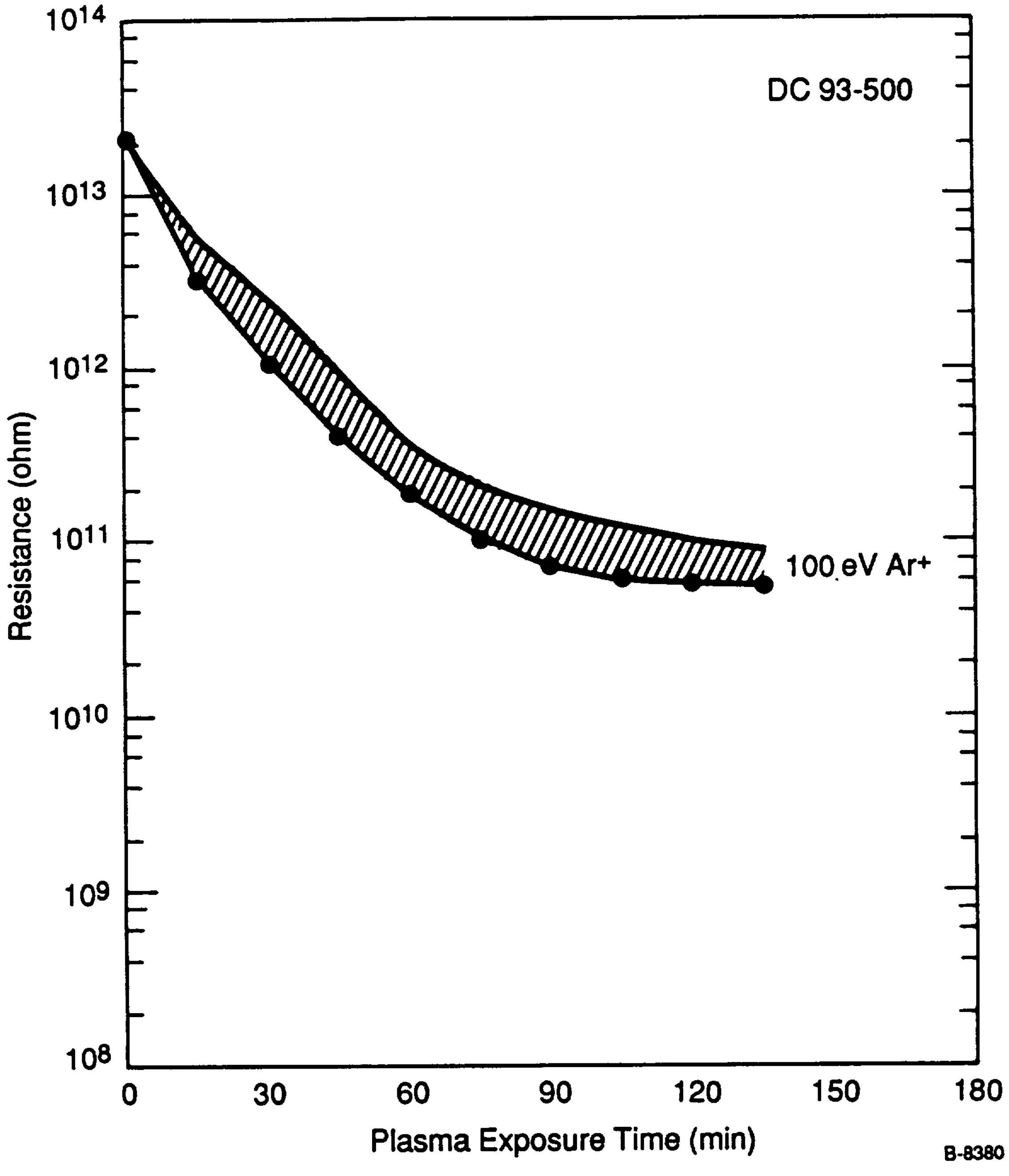

Figure 34. - Adhesive film resistance as a function of 100 eV Ar^+ Exposure Time.

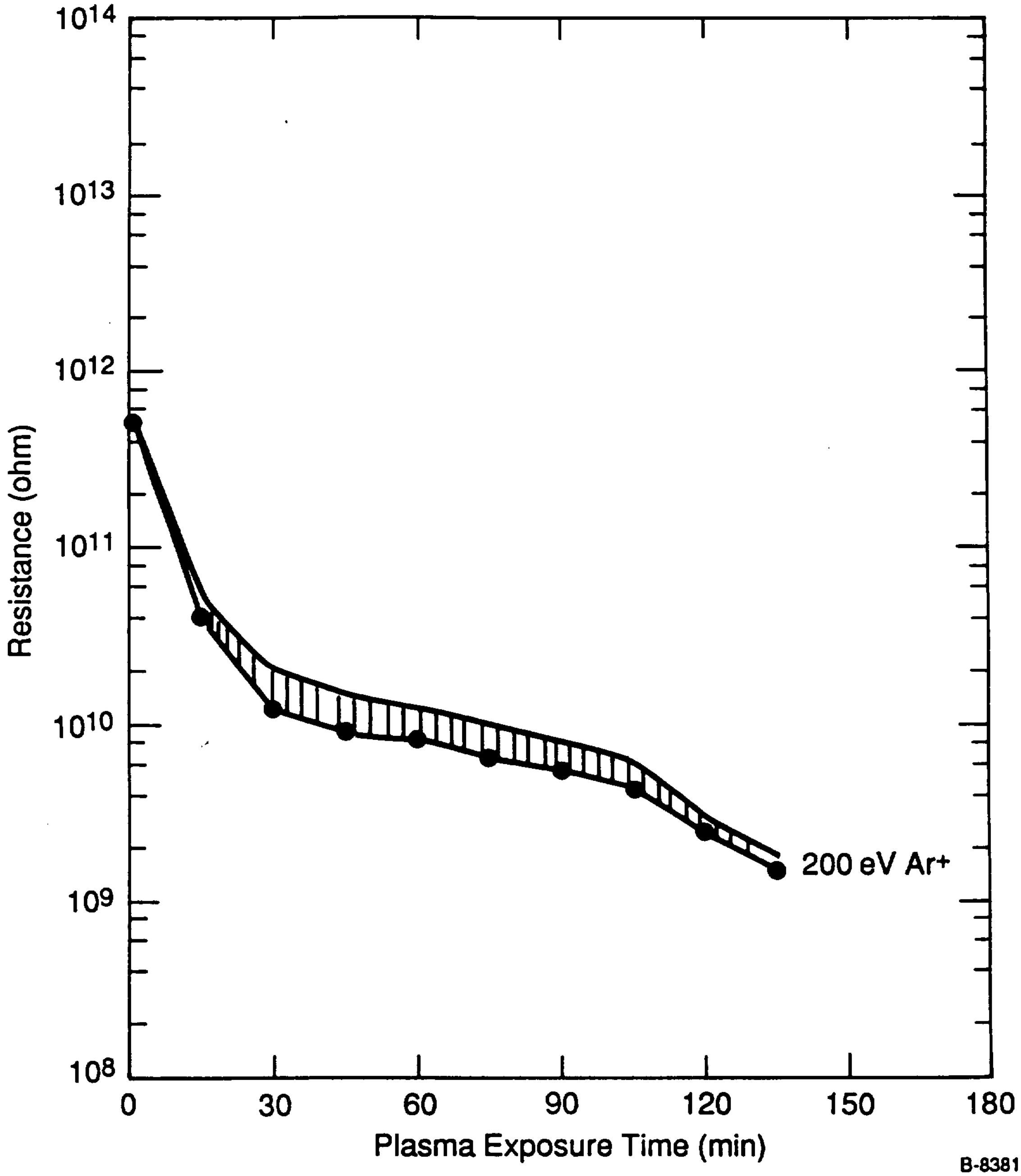

Figure 35. Adhesive film resistance as a function of 200 eV Ar^+ exposure time.

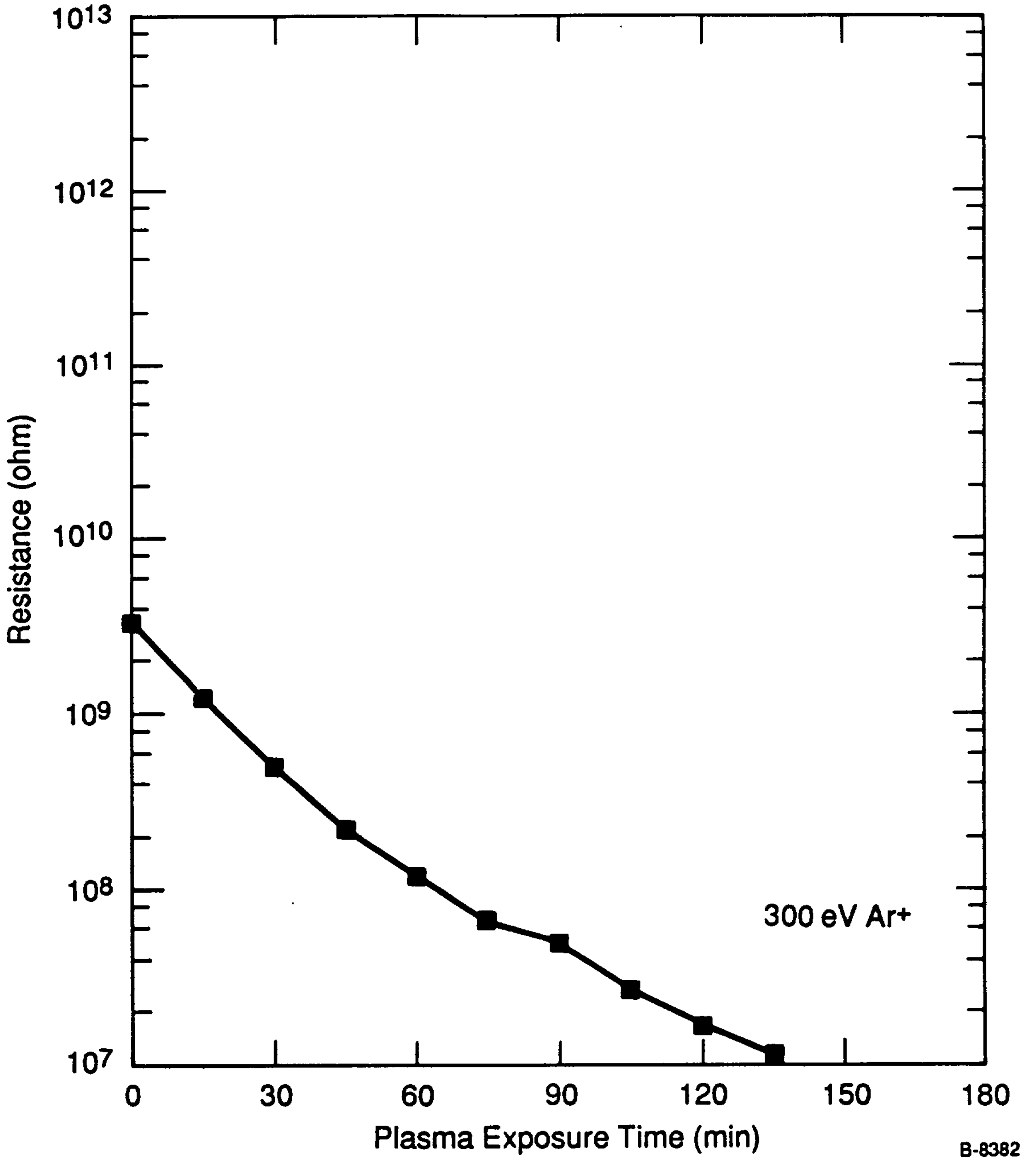

Figure 36. - Adhesive film resistance as a function of 300 eV Ar$^+$ exposure time

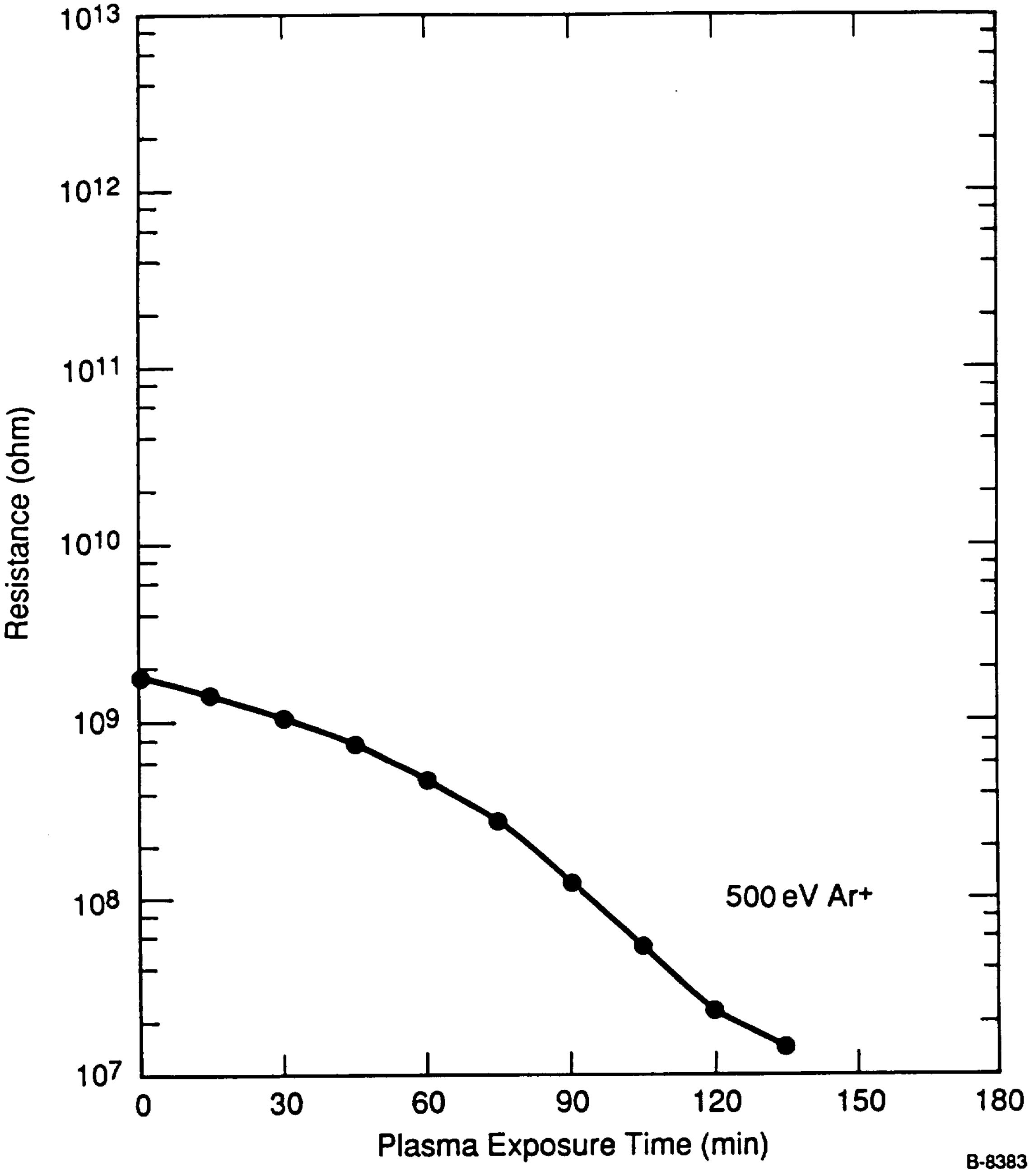

Figure 37. - Adhesive film resistance as a function of 500 eV Ar^+ exposure time.

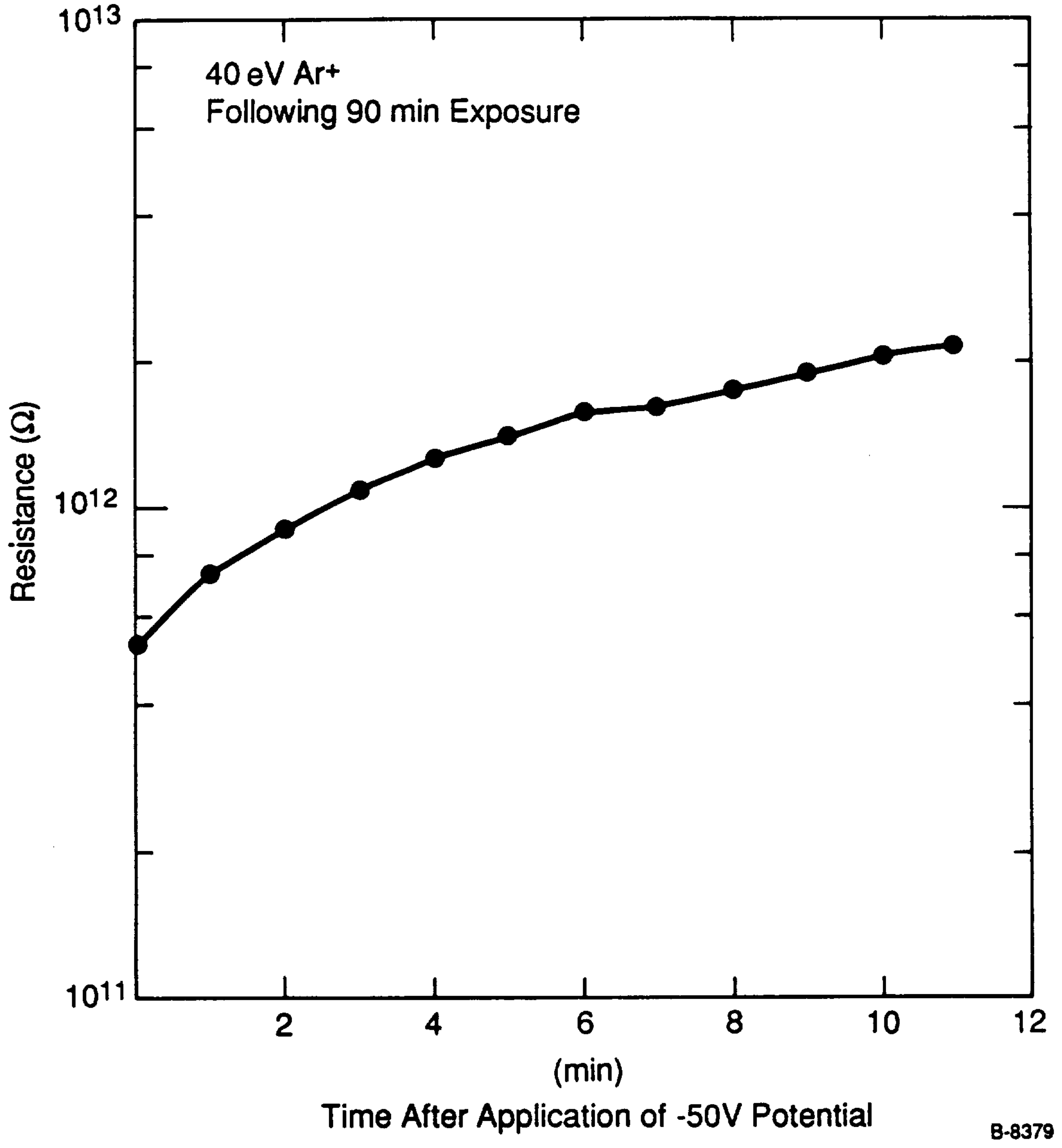

Figure 38. - Drift in the measured adhesive resistance following expsorue to a 40 eV Ar^+ plasma for 90 min.

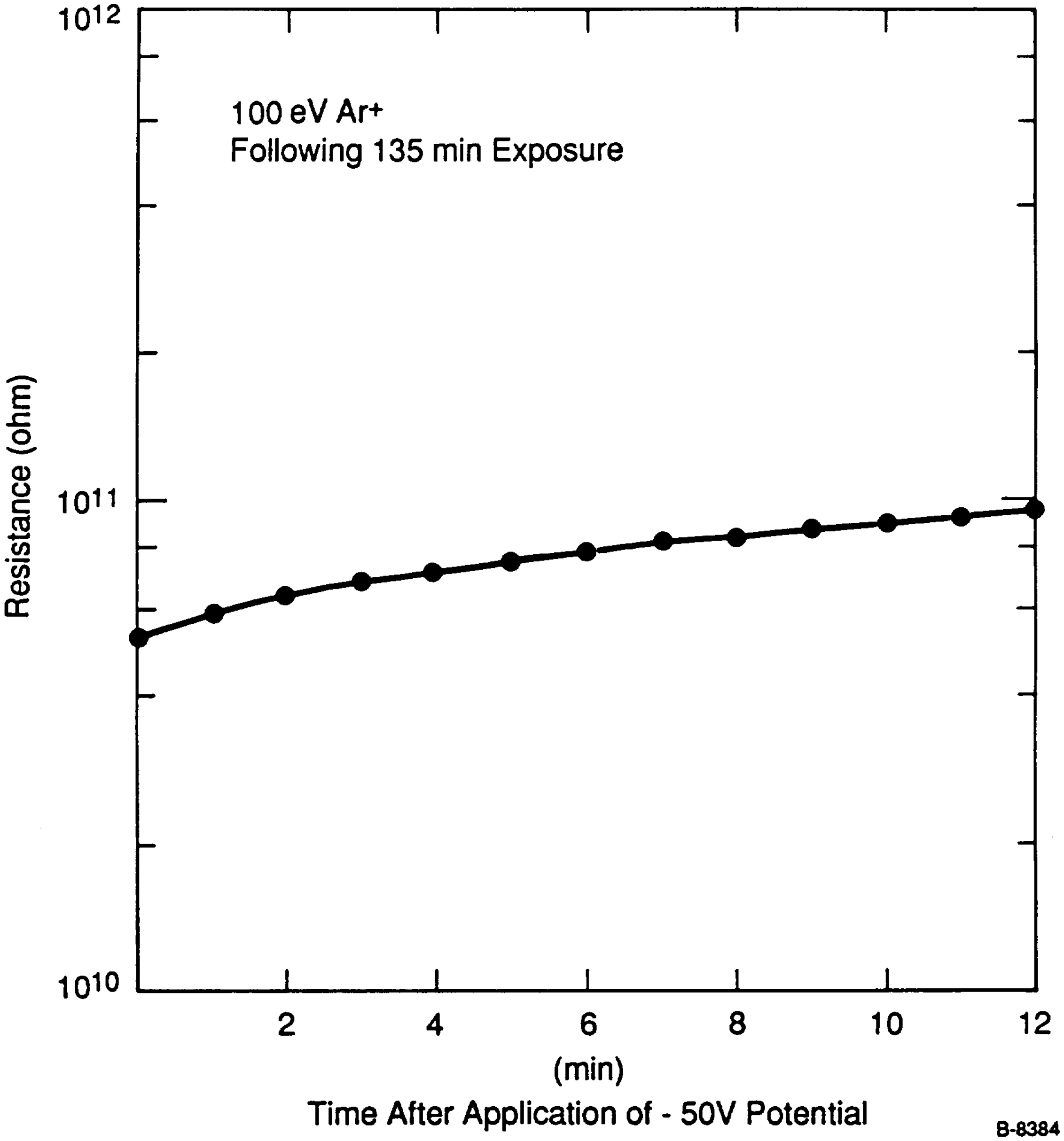

Figure 39. - Drift in the resistance of the adhesive film following 135 min. exposure to a 100 eV Ar^+ plasma.

Auger spectroscopy was used to examine any changes in surface composition resulting from plasma exposure. Since the adhesive is nominally an insulator, a grazing incidence method was used to record the Auger spectrum while limiting the charging of the film by the electron beam. A representative spectrum is shown in Figure 40. The spectrum shows the presence of Si, C, and O characteristic of the bulk material. Changes due to two different effects were possible. First, the sputtering of nearby chamber components by the plasma beam could transfer conducting species to the surface. The most likely species could be carbon from the acceleration grids in the Kaufmann source or copper from the sample holder. The presence of Cu can be verified via the observation of features at 60 eV and 920 eV. Examination of a 100 μm thick, freshly prepared and cured, film surface after a period of 1 hour of 500 eV Ar ion exposure showed no evidence of Cu features or any increase in the carbon signal above the bulk material level.

Additional experiments were conducted in which a freshly prepared and plasma-exposed beam was dosed with 10^{-3} torr-minutes of water vapor in several steps. Periodically, the dosing was interrupted and Auger spectra of the film were recorded. No change in the Auger spectra of the film was recorded. Of particular interest was the behavior of the atomic oxygen peak at 511 eV, which might be expected to increase on surface adsorption of H_2O. These results are consistent with the bulk adsorption data, which shows less than 0.1 percent weight gain when saturated with H_2O.

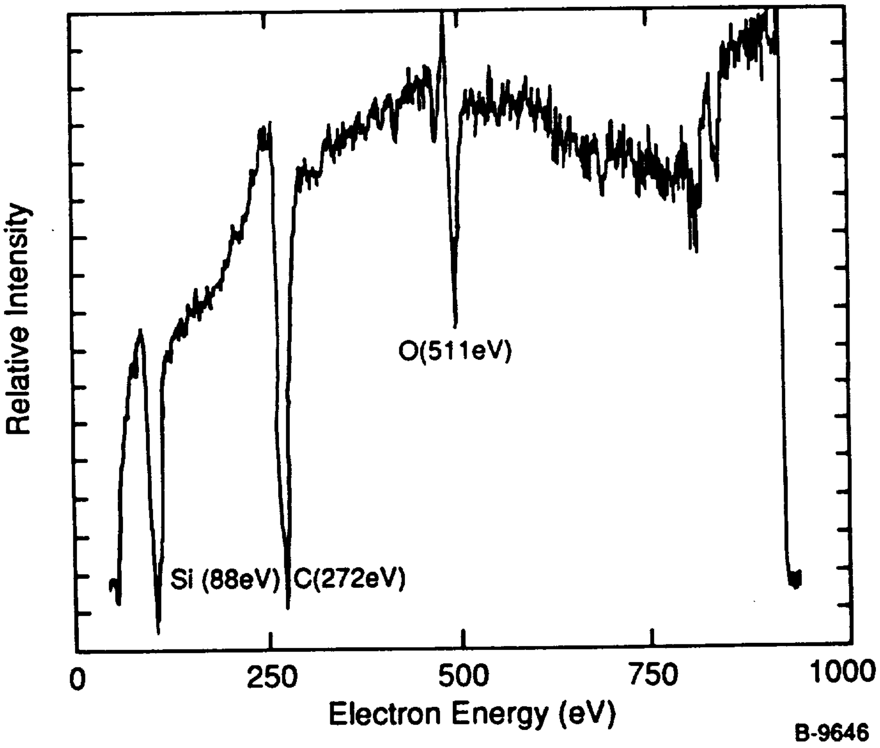

Figure 40. - Auger Spectrum of plasma-exposed DC93-500 adhesive.

Several alternatives exist which may explain this surface resistance decrease. The resistance is inversely proportional to the material conductivity. The conductivity is defined as the product of charge carrier density, N_i, times the charge carrier mobility, μ_i, in the material, and summed over all charge-carrier species, denoted by index/subscript i.

$$C = \sum_i n_i \mu_i \quad . \tag{3-1}$$

Therefore, the resistance can be decreased by either increasing any charge carrier species density or the mobility of any charge carrier. Note that it is possible for ion impact to introduce defect sites at or near the surface which trap the charge carriers. Such a process would decrease the mobility, leading to an increase in resistance. Most likely, the low energy ion impacts lead to electron-hole pair production with a yield, η, which varies with the impact energy. The asymptote to a constant resistance with continued plasma exposure, again could be explained in a variety of ways. In dielectric material it is possible to generate exciton, polaron, or electron-hole pairs by energetic ion impact. These charge carriers exist in specific electronic band structures and have recombination or relaxation times which depend on their mobility and density on the surface. One possibile explanation of the asymptotic behavior is saturation or band filling. The possibility that the surface charges to the incident ion potential and inhibits further charge accumulation was investigated using a voltage probe on the kovar electrodes. The probe showed that the adhesive potential stays within ± 2V of ground. This occurs because the plasma electrons or ions would immediately respond to any significant surface potential. Likewise, we can only speculate about the recovery or drift presented in Figures 38 and 39. A likely explanation for the drift is recombination of electron-hole pairs following tunneling out of specific bands. Alternatively, this drift could arise by recombination of moderate to weakly trapped charge carriers at surface defect sites. The weakest trapping sites, ≤ 0.5 eV, will de-trap or recombine in less than a second whereas more strongly trapped carriers will take longer. Clearly, a complete understanding of the processes at work here would require significant further research and the development of additional analytical tools.

Changes in the optical properties of the adhesive film as a result of plasma exposure were also examined as part of the effort. Adhesive films were deposited on S1-UV quartz and ZnSe optical substrates. The films were cured and then optical transmission spectra of the films were recorded. Figures 41 and 42 show the UV-visible and infrared transmission spectra of the films prior to plasma exposure. In the visible region the film is highly transparent from 1000 nm down to the oxygen absorption cut-off at 190 nm. In the IR the spectrum is naturally quite complex, consisting of feature assigned to methyl and silicon-methyl. After exposure to the plasma at an energy of 500 eV and a plasma density of 2.4 x 10^{-6} A cm^{-2} for a period of 1 hour, the UV-visible spectrum (Figure 43) shows a marked decrease in transmission below 800 nm. This decrease in film transmission is consistent with the "yellowing" of the film observed from UV light exposure. Note that we did not try to differentiate the effects of plasma exposure from the effects due to UV light emission from

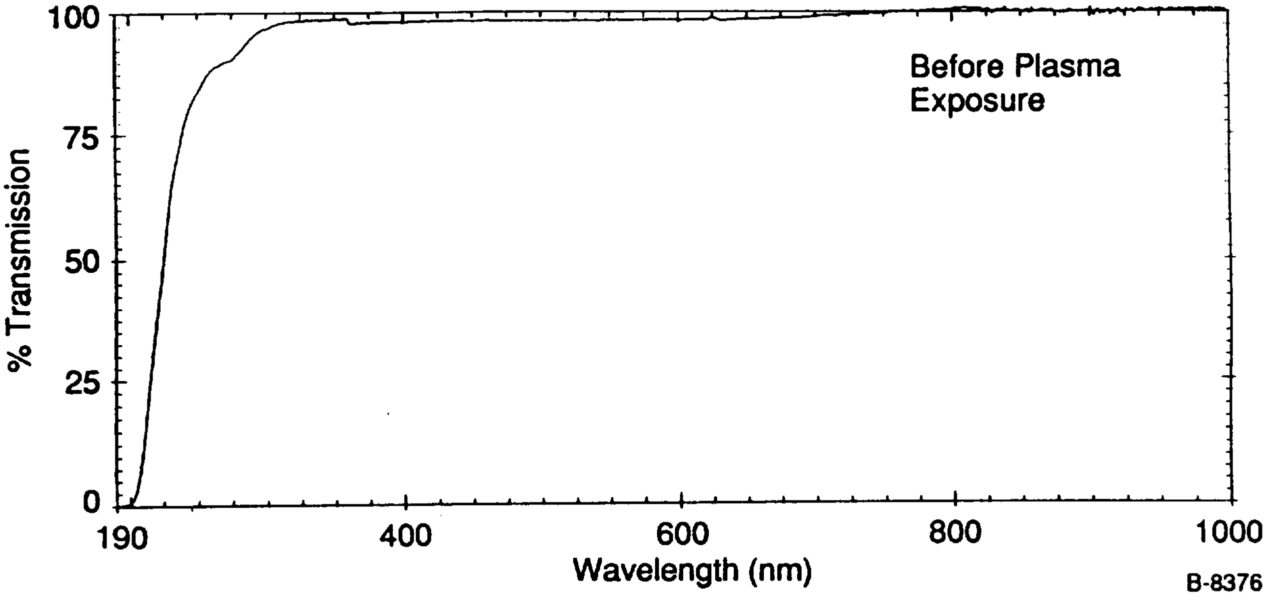

Figure 41. - Optical transmission of DC-93-500 adhesive before plasma exposure.

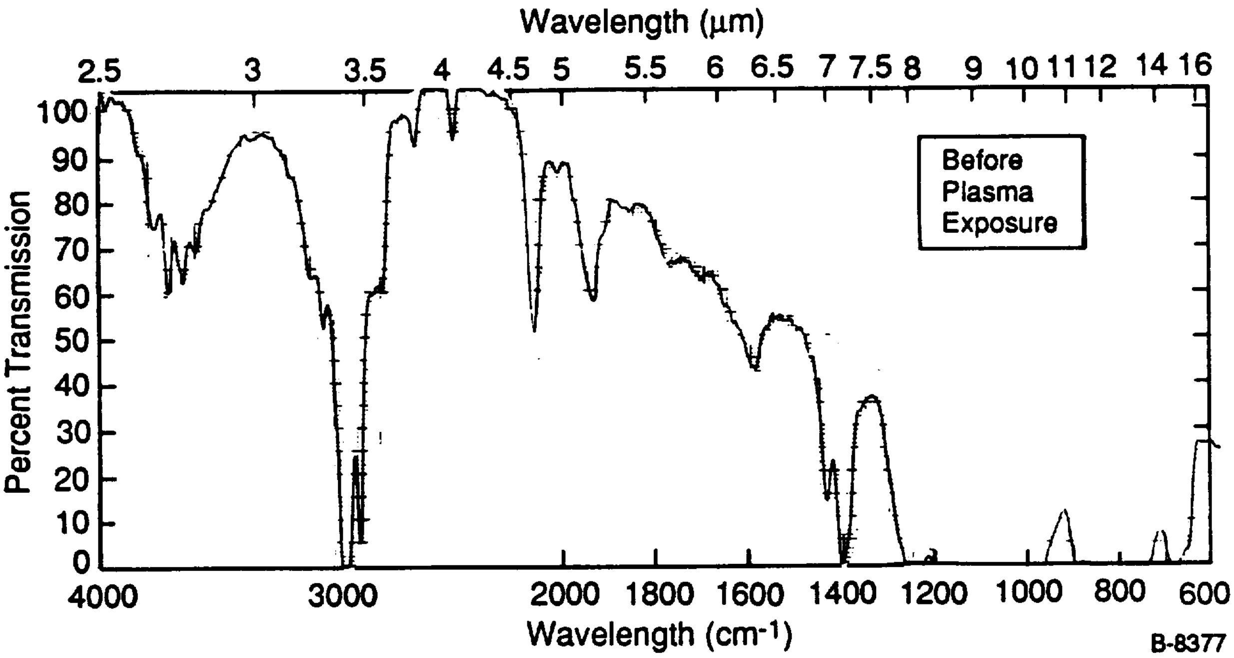

Figure 42. - Infrared transmission of DC-93-500 adhesive before plasma exposure

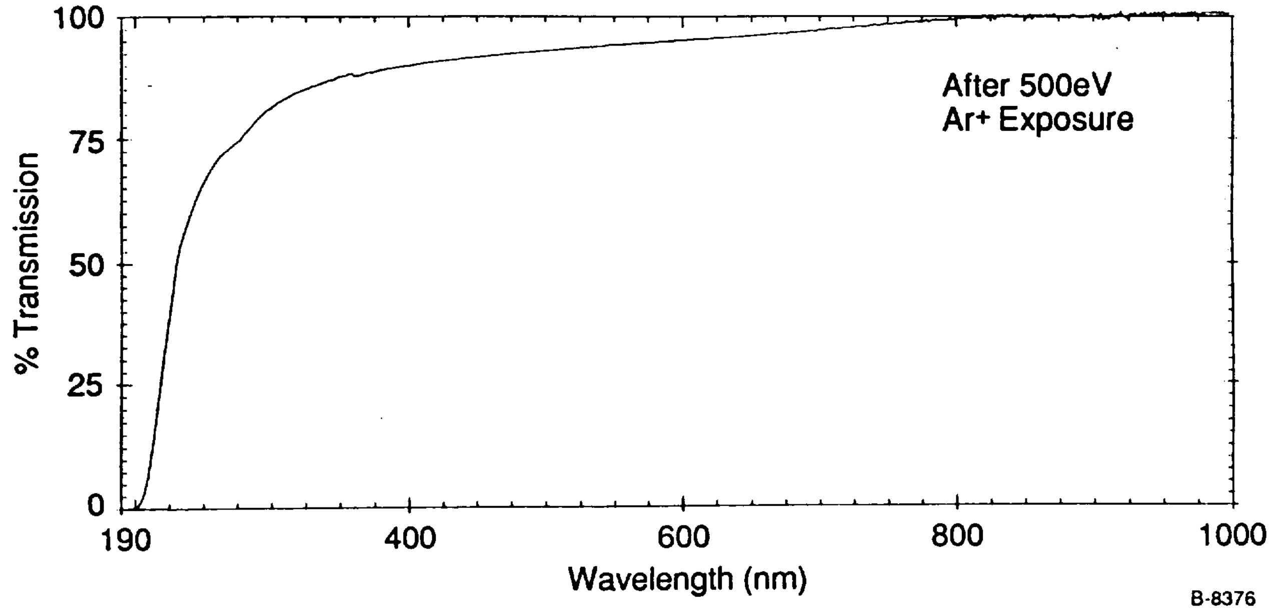

Figure 43. - Optical transmission of DC-93-500 adhesive after 500 eV Ar$^{\pm}$ exposure.

the plasma source. In contrast to the behavior in the UV-visible region, no changes in the IR spectrum of the adhesive film (Figure 44) were observed upon plasma dosing. The IR spectra are, in general, indicative of the bonding present in the film. Hence, we can say that there appear to be no gross changes in the chemical structure of the film due to the action of the plasma.

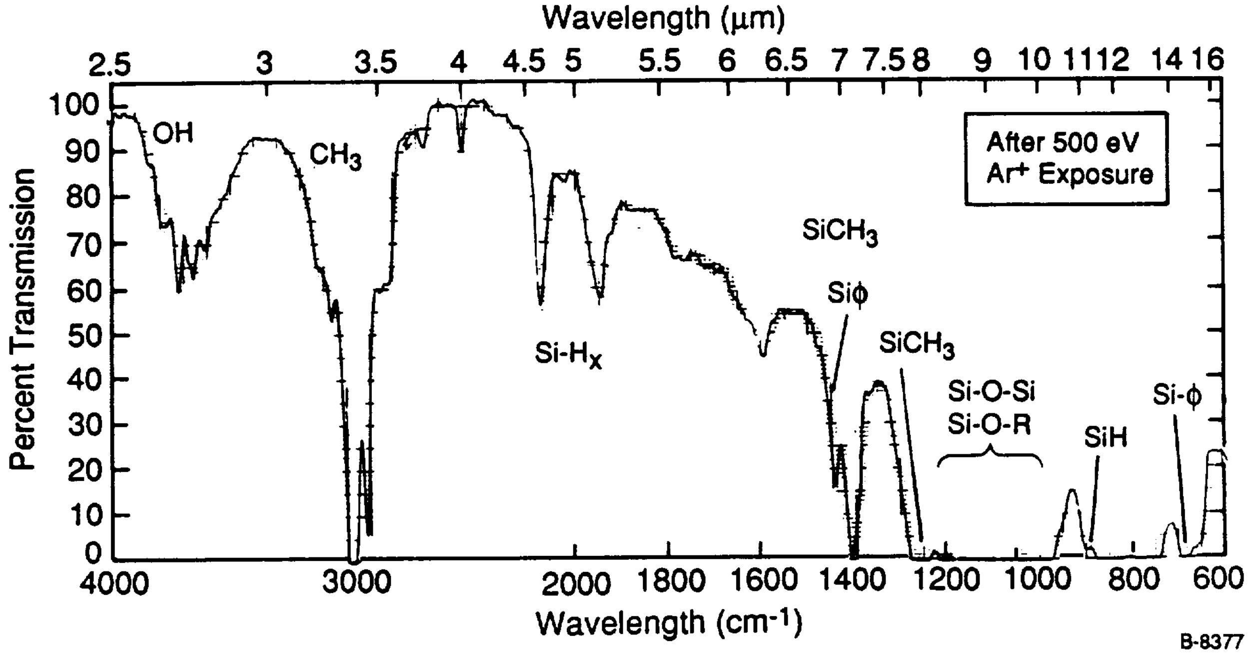

Figure 44. - Infrared transmission of DC-93-500 adhesive after 500 eV Ar^+ exposure.

4. ARCING IN ANODIZED ALUMINUM STRUCTURES

As previously described, when fully insolated, current models of the SSF environment predict that electron collection by the array cell edges and interconnects will drive the return side of the array to -130 volts. Thus the anodized aluminum coating on the truss (which is an insulator) must be capable of withstanding the -130 volt bias. Measurements of arcing thresholds for these films reported by Carruth et al.[17] at NASA Marshall and Grier et al.[18] at NASA Lewis have shown these coatings to have a breakdown threshold of -120 to -140 volts. Furthermore, extensive sputtering of the arc site is noted as is a propensity for site to arc repetitively and at lower bias voltages once formed. Measurements conducted on a somewhat thicker (0.2 mil or 50 μm) coating produced by a sulfuric acid process have been observed to arc at -500 to -600 volts[18]. The observed breakdown voltage is somewhat greater than previously determined for oxide films. The data presented in Figure 45 from Reference 26 shows a measured breakdown voltage of 225 volts for an 0.2 mil thick oxide layer produced in a 10% sulfuric acid bath. Once an arc site is formed in the oxide film, arcing is observed to occur at voltages as low as -140 volts at these sites. In our measurements we were able to determine the arcing behavior of both aluminum oxide film types.

Our experiments again employed the UHV chamber for detailed measurements of arcing behavior, particularly when environmental effects were under consideration. However, we were also quite interested in the response of the oxide surface to two additional

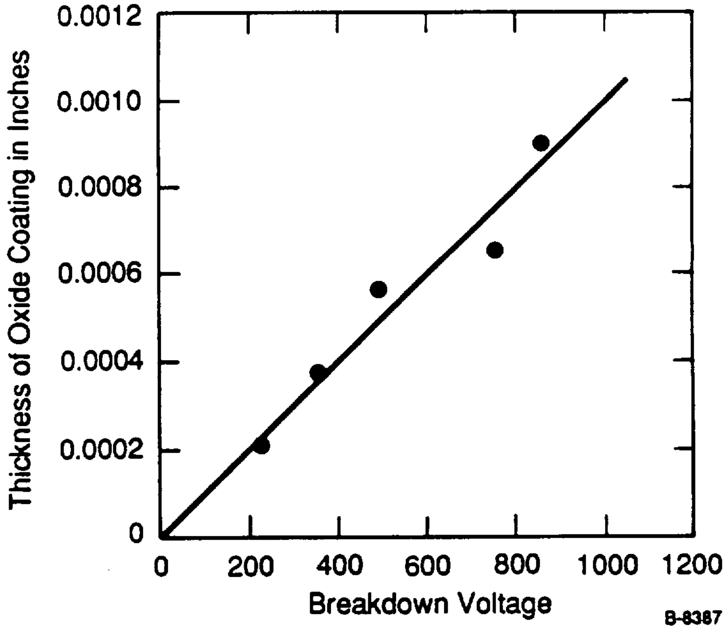

Figure 45. - Dependence of breakdown voltage on thickness of water-sealed oxide coating on aluminum.[26] Ten percent sulfuric acid at 35°C (95°F). Current density 14.4 amp per sq ft.

environmental factors - LEO atomic oxygen and micrometeorite/debris (MM/D) impact. The impact of MM/D on an oxide film would result in the removal of the oxide layer in the vicinity of the impact area. If the underlying aluminum substrate was at high voltage an immediate plasma arc would probably ensue, stimulated by the enhanced ionization and background gas present at the impact site. Actual MM/D impacts are rare and arcing at impact is probably only a minor concern. However, the impact site becomes a triple junction in direct exposure to the space plasma and therefore will have an enhanced probability for arcing in the ambient plasma environment. These impact sites are also exposed to the ambient LEO atomic oxygen flux which could, in principle, act to reform the oxide layer at the impact point. Hence, it is possible that these sites could self anneal. To examine the arcing behavior of these oxide layers in the presence of these envronmental factors we employed the PSI FAST atomic oxygen exposure simulation facility. To simulate MM/D impacts on the film we tested damage sites produced by the action of a pulsed laser.

4.1 Measurement Configuration

Our experiments conducted in the UHV chamber utilized an experimental configuration similar to those employed in the solar cell measurements. The details of the fast O-atom system have been published previously.[27] In the experiments utilizing this system (Figure 46), the aluminum plate was mounted at a 45° angle to the direction of the fast O-atom beam. The plasma source replaced the detector

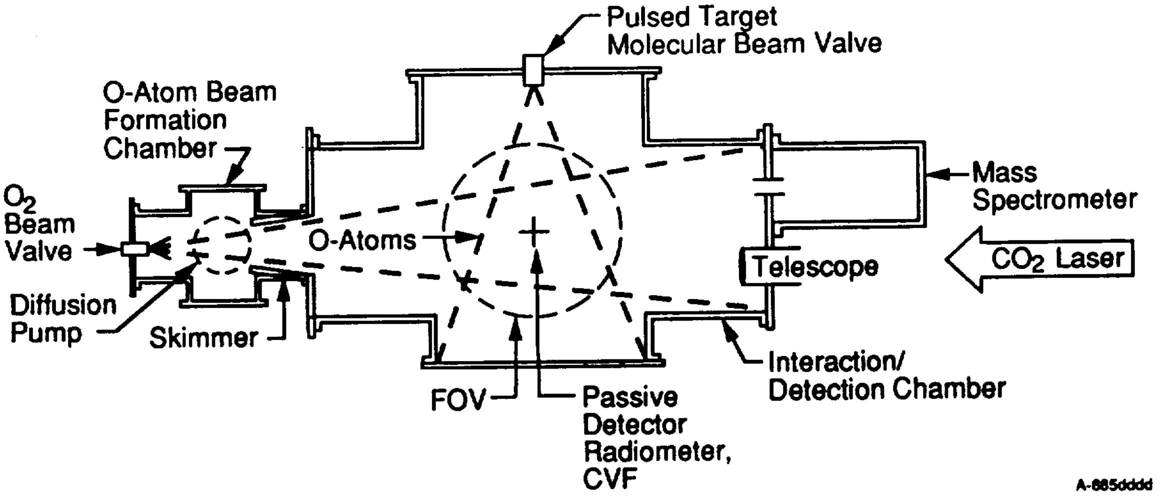

Figure 46. Fast O-atom crossed molecular beam system.

system and could also be used to irradiate the Al-plate; however, these two sources of impinging particles could not be utilized simultaneously. This restriction arises because the oxygen from the fast O-atom source quickly, i.e., ~ 1 hr, destroys the heated filaments of the plasma source. We also implemented an ultra-violet/visible viewport on the fast O-atom chamber so that our previous light sensitive diagnostics, such as the UV radiometer and CCD camera system, could be employed to provide information simultaneous with the electrical diagnostics, such as the high voltage probe and arc current sensor.

The aluminum plates were mounted in vacuum and electrically insulated from the chamber wall. For the ultra-high vacuum system we used our standard sample holder with a ~ 2 x 4 cm^2 piece of the Al-plate. Because the Al-plate surfaces are coated with the Al_2O_3 insulator it was necessary to scratch off a little of the coating at one corner so that electrical contact was made to the copper sample holder. It was also necessary to cover any cut, i.e., non-anodized, edges of the Al-plate with teflon insulator. As will be demonstrated below, this is necessary because the cut edges exhibit arcing behavior at lower potential than the uniform coating surface. The cut edges were covered by slicing open teflon heat shrink tubing and sliding it over the cut edges. In the fast O-atom system, we were able to utilize a larger piece of the Al-plate, 2.6 x 12.8 cm^2. The electrical connection and mounting is shown in Figure 47. The stainless-steel set screw was threaded into a blind taped hole in the back center of the Al-plate and a nut/washer pair locked the plate to the screw. This length of set screw allowed a coaxial micro-clip connection to be attached to the plates providing the electrical contact. A teflon rod acted as an electrical standoff and was attached to a brass

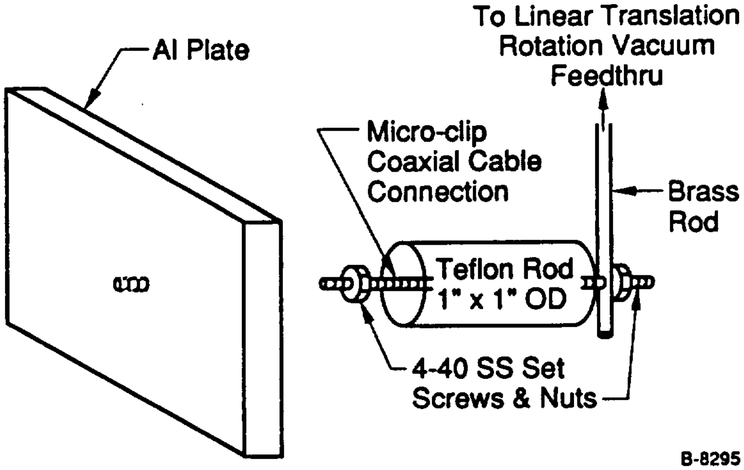

Figure 47. Mounting and electrical connection for Al-plate in the fast O-atom system.

rod for mechanical mounting, once again using a set screw/nut/washer combination. The brass rod was connected to a linear translation-rotation feedthrough so that the plate could be positioned when under vacuum. Movement was avoided in most cases so that camera views before, after, and during surface treatment or arc testing would be identical and comparable. Teflon coating of cut edges was also used when studying the uniform or controlled damage coating.

4.2 UV-Light, Current, and Voltage Measurements of Al-Plate Arcs

The electrical signature of the Al-plate arc and the correlation to UV light emission is somewhat different than observed on solar cells. Figure 48 presents the data acquired for a modest arc event initiated at -400V, on a uniform coated surface, with a small damage spot (650 μm diameter). The arc-sensor, using a total capacitance of 220 pf, (Figure 48a) traces current flow in the arc event and shows that the event lasts several microseconds, but exhibits a very fast rise at arc initiation and a sharp current reversal at about 3.9 μs. Both of these features are reproducible for nearly every Al-plate arc we have examined and for all edge, damage spot, or uniform coating arc events. The fast rise was previously noted with solar cell arcs, but the current reversal was not previously observed. The high voltage probe (Figure 48b) confirms the current reversal, showing a fast negative progression of the plate potential simultaneous with the current reversal. The bias power supply is decoupled on this time scale and cannot contribute to the observed currents. This negative progression of the plate potential near arc termination is also not observed in solar-cell arc phenomena. The UV-light emission (Figure 48c) is easily observable but does not correlate as well with the arc current sensor signal. Good correlation between the two diagnostics was observed in solar cell arcing. The light emission start matches with the arc initiation, but does not peak at maximum current flow. Ultraviolet light emission also ceases at the time of current reversal. Figure 49 presents similar data collected for an edge arc initiated at -230V. The same features are observed, but note that the event lasts nearly 7 μs. The correlation between the arc-sensor and the high-voltage probe is presented in Figure 50. The HV-probe data has simply been normalized. The arc current sensor data is presented as the running integral which has also been normalized. These two traces should match (by definition) and are closely correlated. The UV-light running integral (total photons emitted) (Figure 50(c)) does not correlate with total charge transferred.

The most unique new observation from the electrical diagnostic measurements is the arc current reversal. After some thought and analysis, we believe we have a reasonable explanation for the deserved phenomenon. In Figure 51 the data from the arc occurring at the edge of the plate is again presented, but with specific points, A and B, and regions I, II, and III designated. We will attempt to explain, qualitatively, the phenomenon occurring at each of these locations. Point A represents arc initiation, probably due to dielectric breakdown. This could be ionization or avalanche initiation in the dielectric coating. The important aspect of Point A is two-fold. First, arc ignition is rapid, and we believe generates a gaseous ionized atomic/molecular plume above the surface.

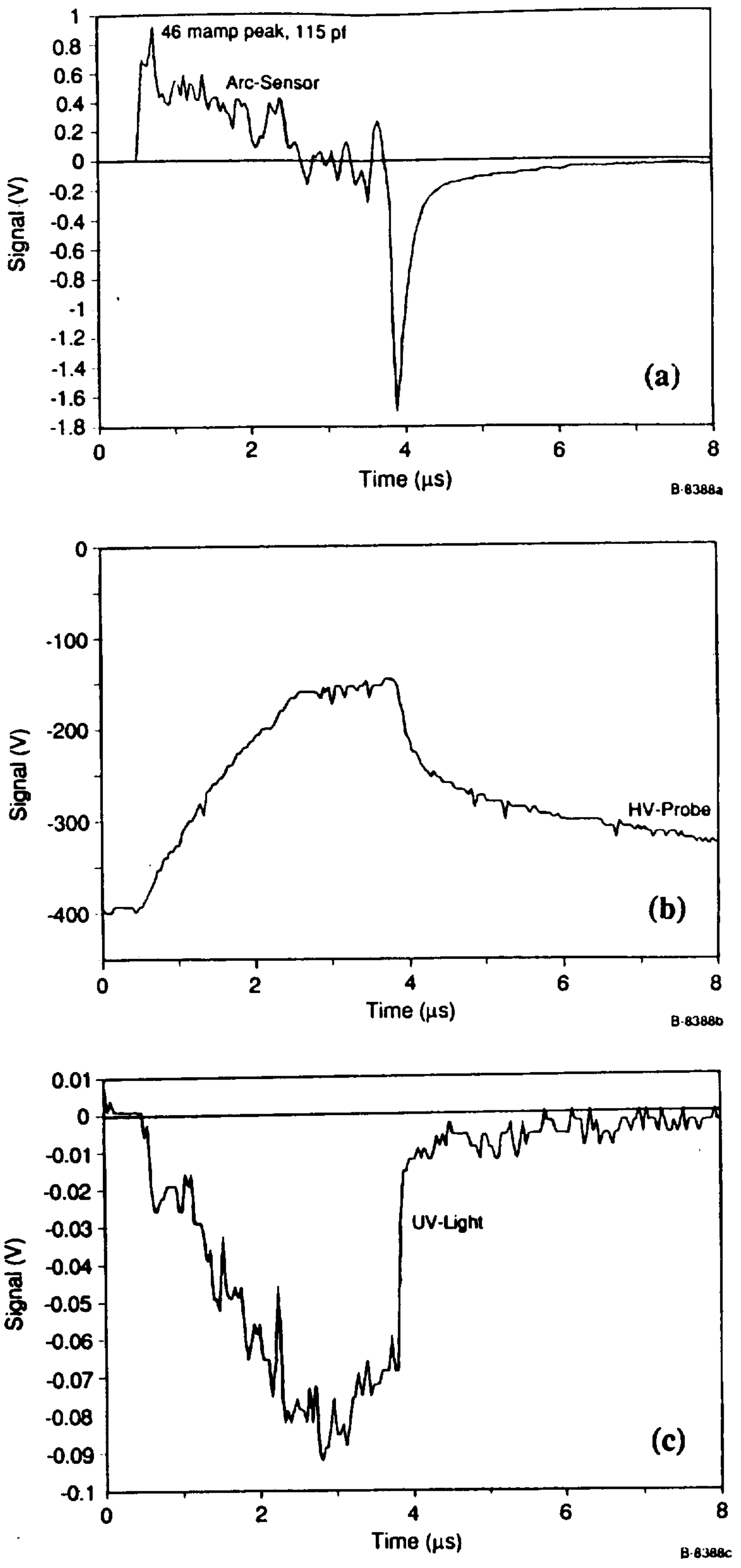

Figure 48. Electrical and UV-light emission characteristics of a uniformly coated Al-plate.

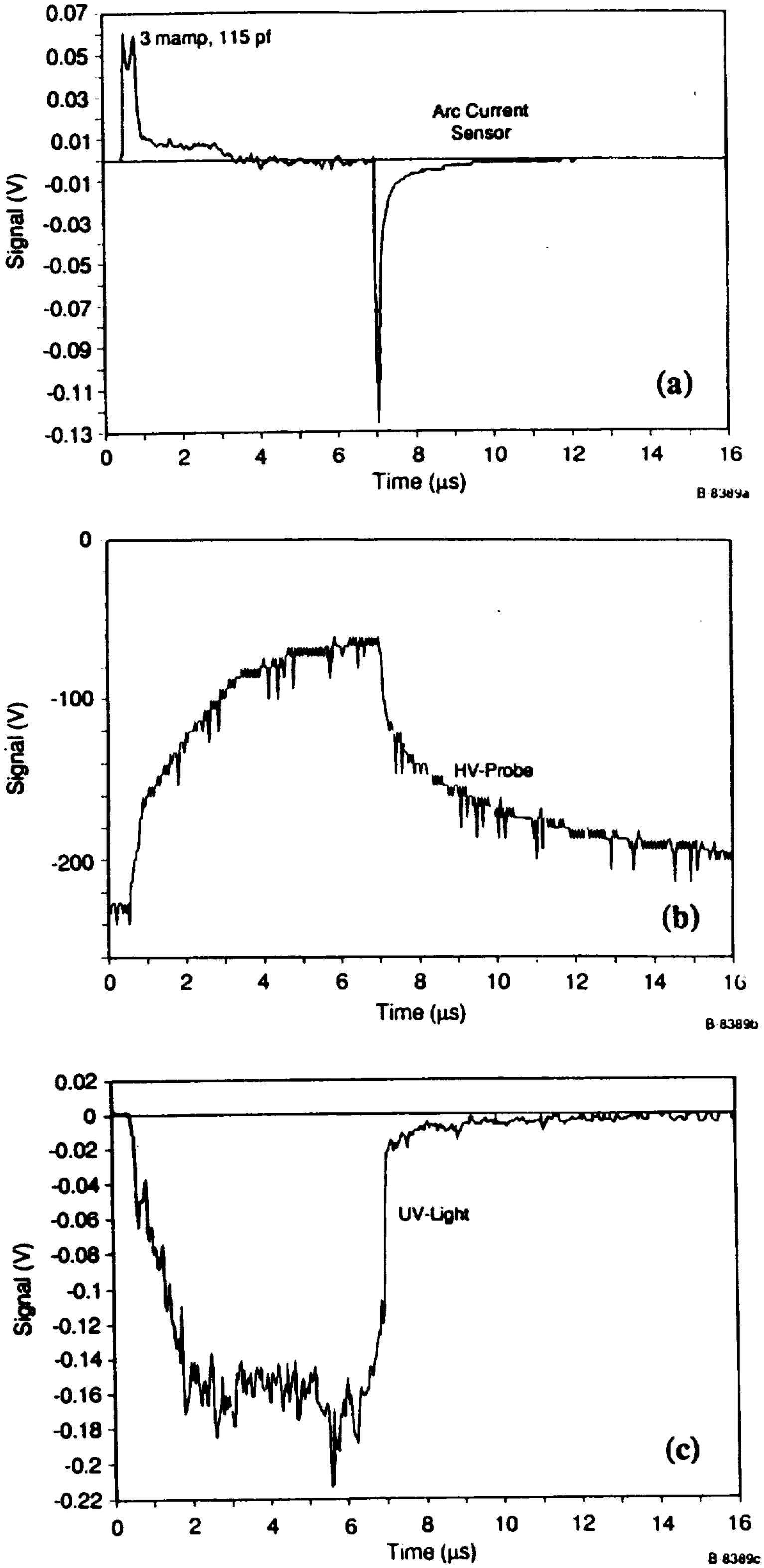

Figure 49. - Electrical and UV-light emission characteristics of a cut edge Al-plate arc event.

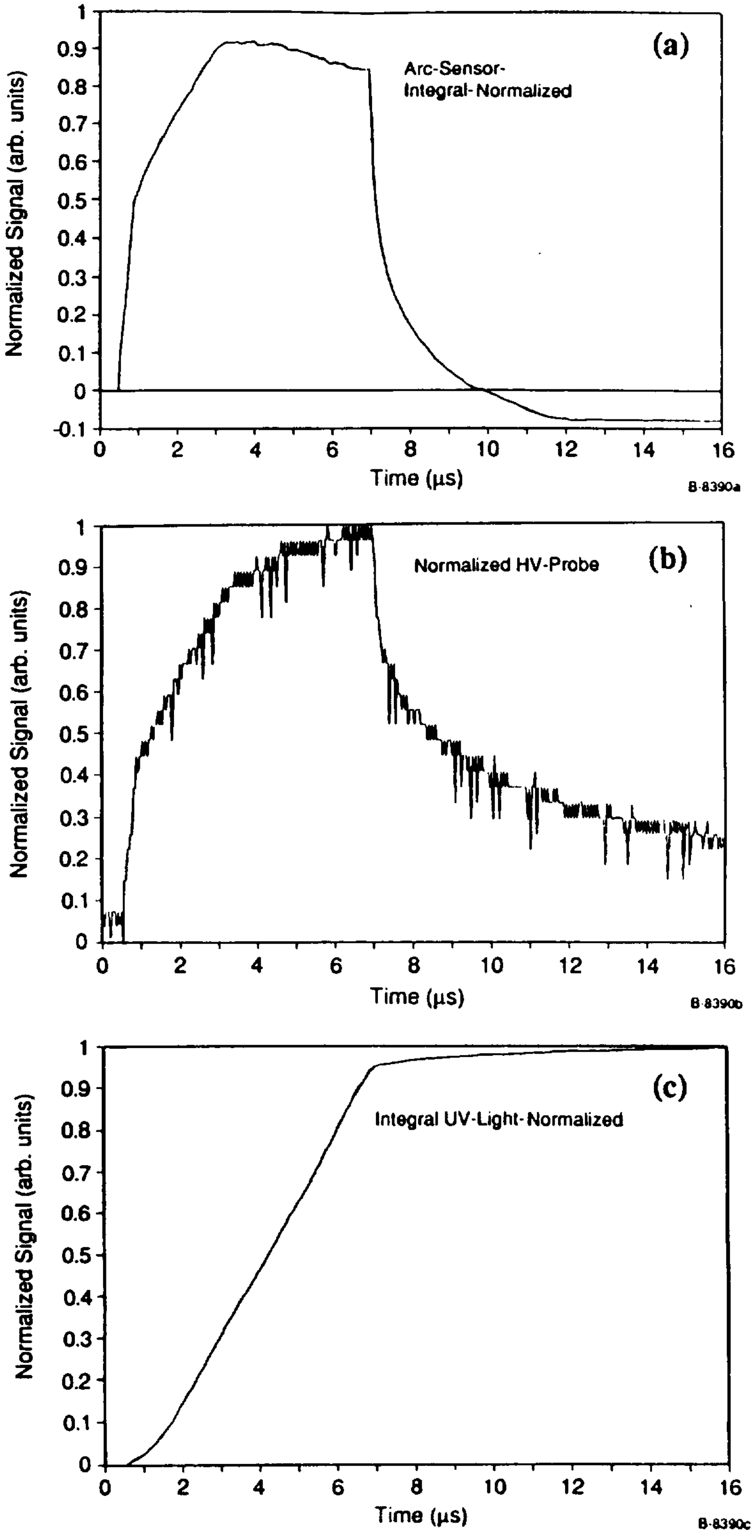

Figure 50.- Correlation comparison of electrical and UV-light emission time profiles for a cut edge Al-plate arc.

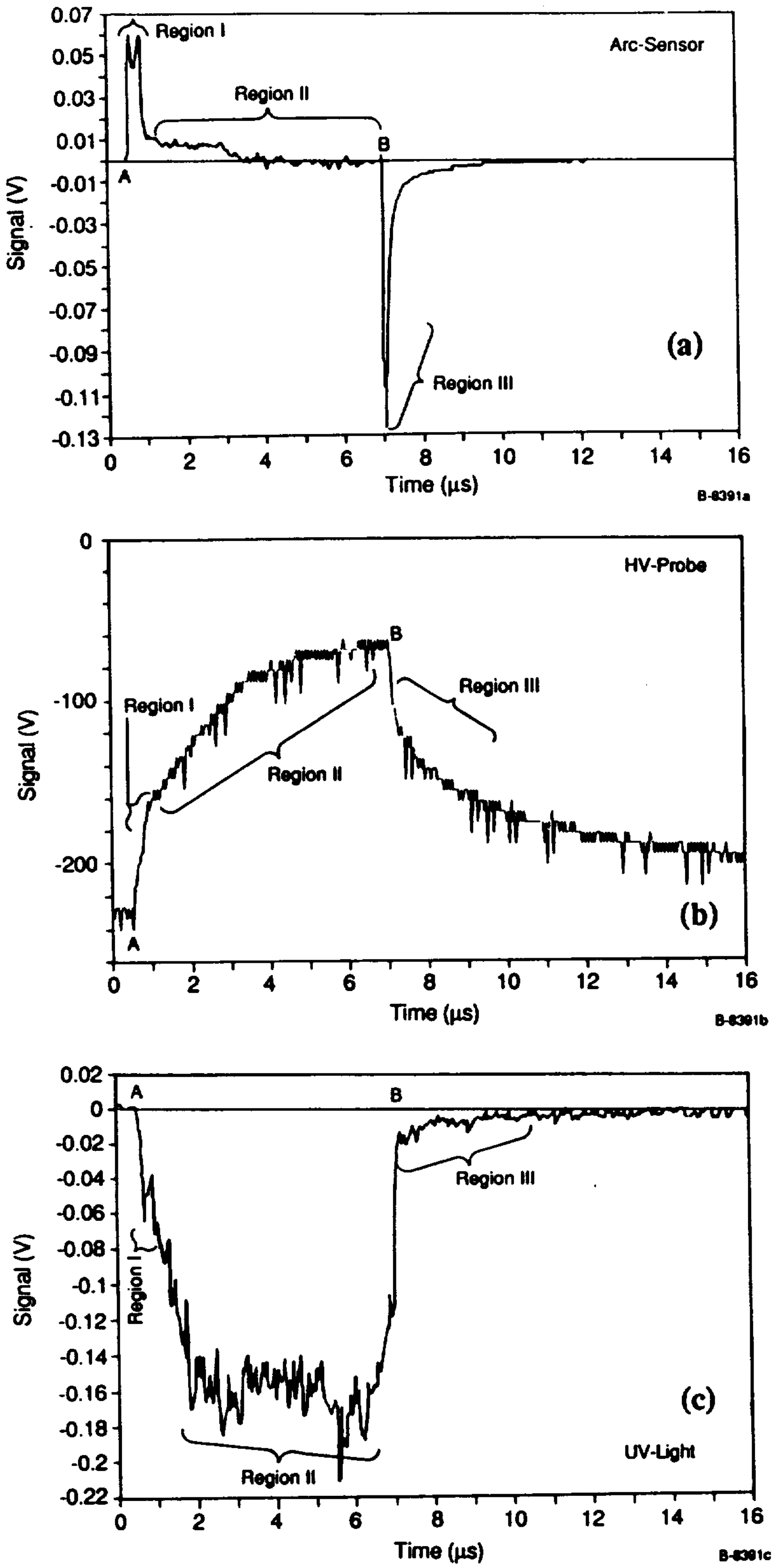

Figure 51. - Qualitative description of specific points and regions in the arc process (see text).

Region I incorporates several key changes. Current flow from the initiation causes secondary electron emission from the Al-plate and from the coating edges along the breakdown track. The secondary electrons accelerate sufficiently to further ionize the gas plume generated at arc initiation. Hence, a dense (much denser than the plasma source contributions) conducting plasma is formed above the arc site. Electron flow through the dense plasma to the surrounding weak plasma causes the Al-plate potential to rise. The Al_2O_3 coating begins to rise in potential, but is immediately fed electrons from the plasma sheath above the entire area of the surface. Very quickly, ($\leq$200 ns) the sheath electrons are depleted and the coating surface potential rises to match the rising Al-plate potential. Calculations show that the sheath contains less than 10 percent of the charge that is used in the discharge.

Region II involves a fully developed gaseous breakdown. We believe this region shows a reduction in the arc current flow because the arc ceases to couple strongly to the surroundings. Only the current flow to the chamber plasma and walls is detectable. Because the sheath has been depleted of electrons and the coating surface has risen positively, we believe that the arc now couples strongly to the local anodized surface. The continuing current flow and light generation can be thought of as arising either by DC charge flowing between the positive coating surface and the negative Al-plate, through the gaseous plume/plasma generated by the arc initiation event. The surface and bulk potentials only slowly rise compared to Region I, and the observed current flow decreases to nearly zero. However, UV-light generation continues due to the continued current flow between the arc site and the anodized surface.

Point B involves the collapse of the local high density arc plasma. Continued ionization and recombination of the plasma heats the gas to high temperature forcing it to expand very rapidly. As plasma density falls, ionizing collisions between secondary electrons and neutral atoms or molecules become less probable. Hence, the ion-electron recombination shuts off, terminating the UV-light emission.

In Region III, relaxation of the local high density plasma is observed. The secondary electrons, generated from the Al-plate and coating, were initially confined in the dense plasma during the arc event. The gas expansion and collapse of the plasma discharge releases these electrons. The electrons flow toward the most positive potential in the system, which at this time is the Al_2O_3 coating surface. The electron flow to this surface forces the coating potential more negative, which forces the Al-plate more negative. This effect is observed as a current reversal in the arc sensor.

4.3 Al-Plate Arc Location

Using the CCD camera system, we were able to observe arc events at several different locations. The location can be closely correlated to the "quasi" threshold voltage, and the type of surface at that location. The following pictures are of UV-light emission, no observable visible light was detected. Figure 52 presents a composite of four arc events

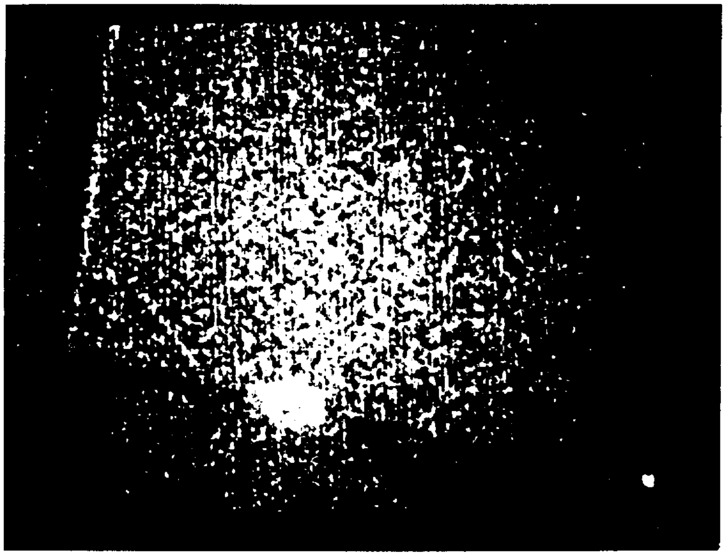

Figure 52. - Composite of 4 edge arc events.

along a cut edge of the Al-plate. These events have been electronically overlayed for display purposes; they did not occur simultaneously. The perimeter of the plate is barely discernable, but note that a vertical edge is within the camera field of view on the left side. This was an anodized edge and we did not observe arc events at that location. Figure 53 shows the arc event observed at a damage spot generated by drilling too deeply into the back of the plate for the mounting set screw. The arc is exactly overlayed with the damage spot. Figure 54 is a microscope view of the damage spot generated on the front surface. The bright vertical edges are the teflon coated edges. These edges are not observable in the UV arc event, but are seen in the overlay of the visible picture on the UV-arc picture. The "quasi" threshold for this damage spot arcing is slightly higher than for edge arcing. Figure 55 shows a composite of two arc events in regions of uniform/undamaged Al_2O_3 coating. Again a visible overlay shows the teflon coated edges. The dark mask in the center was placed on the camera to avoid viewing the arc events at the damage spot in the plate center. These arc events required the highest potential or "quasi" threshold. In no case were we able to later identify surface damage which might have initiated or which was generated by these events. At voltages more negative than -500V, arc events could be observed at all three types of locations; edges, damage spots, and uniform coating regions, implying all could occur at the same time.

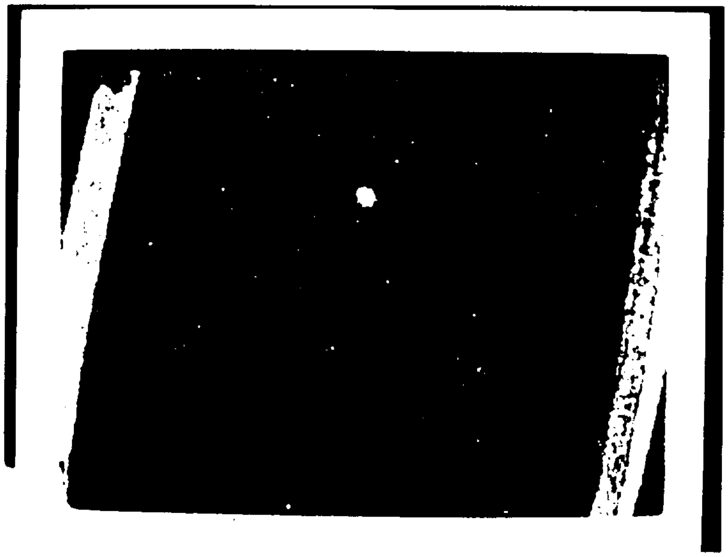

Figure 53. Arc event at damage spot caused by drilling.

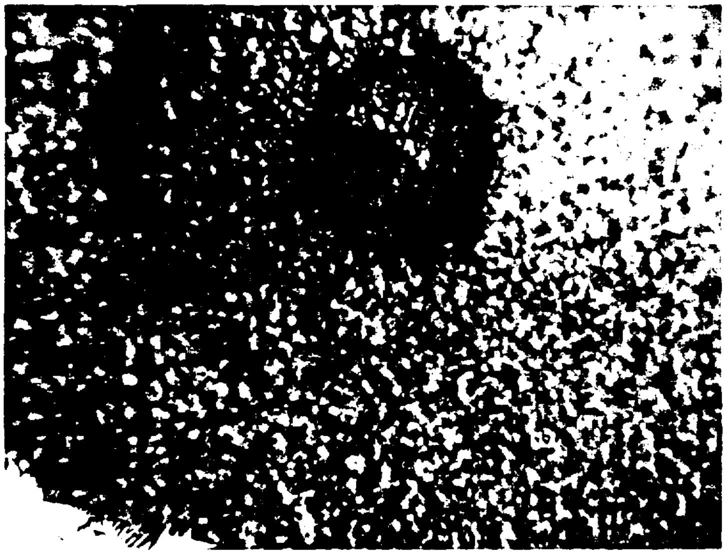

Figure 54. Protrusion damage generated by drilling the Al-plate back side.

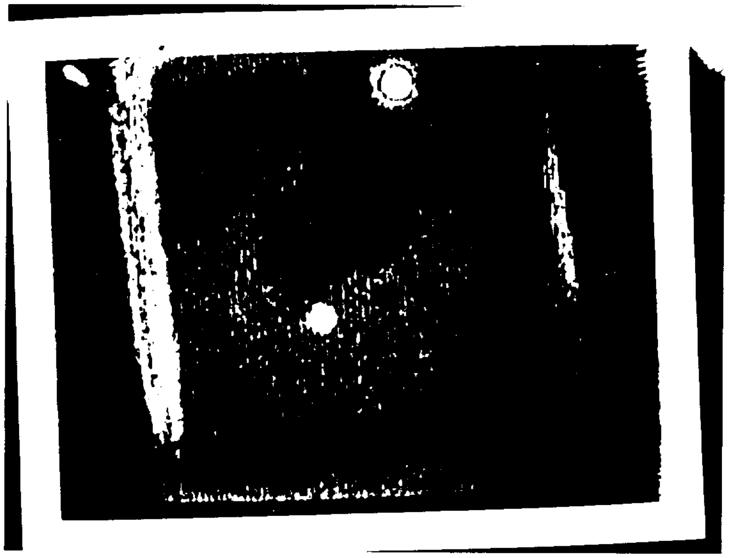

Figure 55. Composite of two arc events in regions of uniform Al_2O_3 coating.

4.4 Arc Thresholds on Al-Plate

Arcing thresholds are difficult to measure. For our purposes we have defined the arc threshold as the voltage corresponding to an arc frequency of 0.1 min^{-1}. At arcing rates below 0.1 min^{-1}, statistical considerations require countings times approaching the lifetime of the filament in the Kaufmann ion source. Typically we count arc events for periods ranging from 10's of minutes up to one hour near the threshold, with the objective of detecting at least five events for statistical confidence. Figure 56 shows the arc frequency versus voltage measurements for two different uniformly coated and unchanged 2 x 4 cm^2 Al test plates. The thresholds are -490 to -650V. In addition, we tested a uniform coated plate for H_2O sensitivity at -900V. The results are presented in Figure 57. Only with massive doses of H_2O were we able to see any arc frequency variation outside statistical uncertainty. This suggests very little, if any, H_2O arc frequency sensitivity. The arc frequency of the drill point damage spot is present in Figure 58. It appears the threshold is between -250 and -200V. The cut edges of the Al-plate showed the lowest arcing threshold (see Figure 59). The threshold is around -70V.

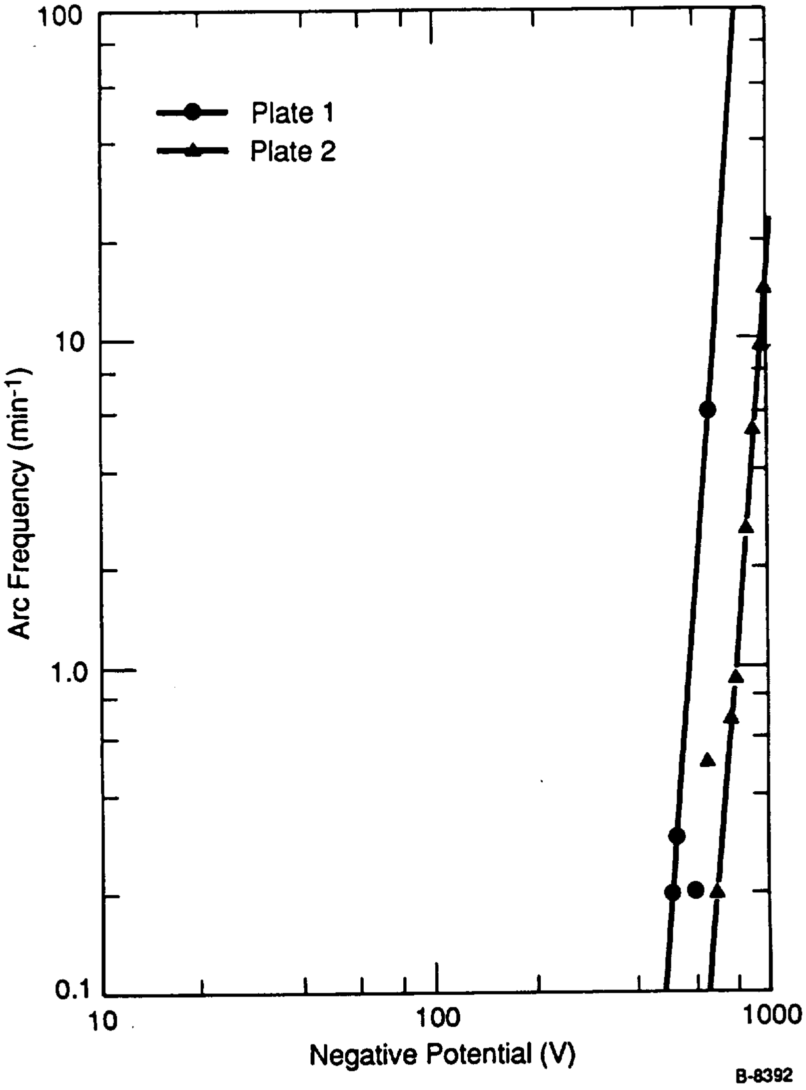

Figure 56. - Arc frequency of uniformly coated Al-plate.

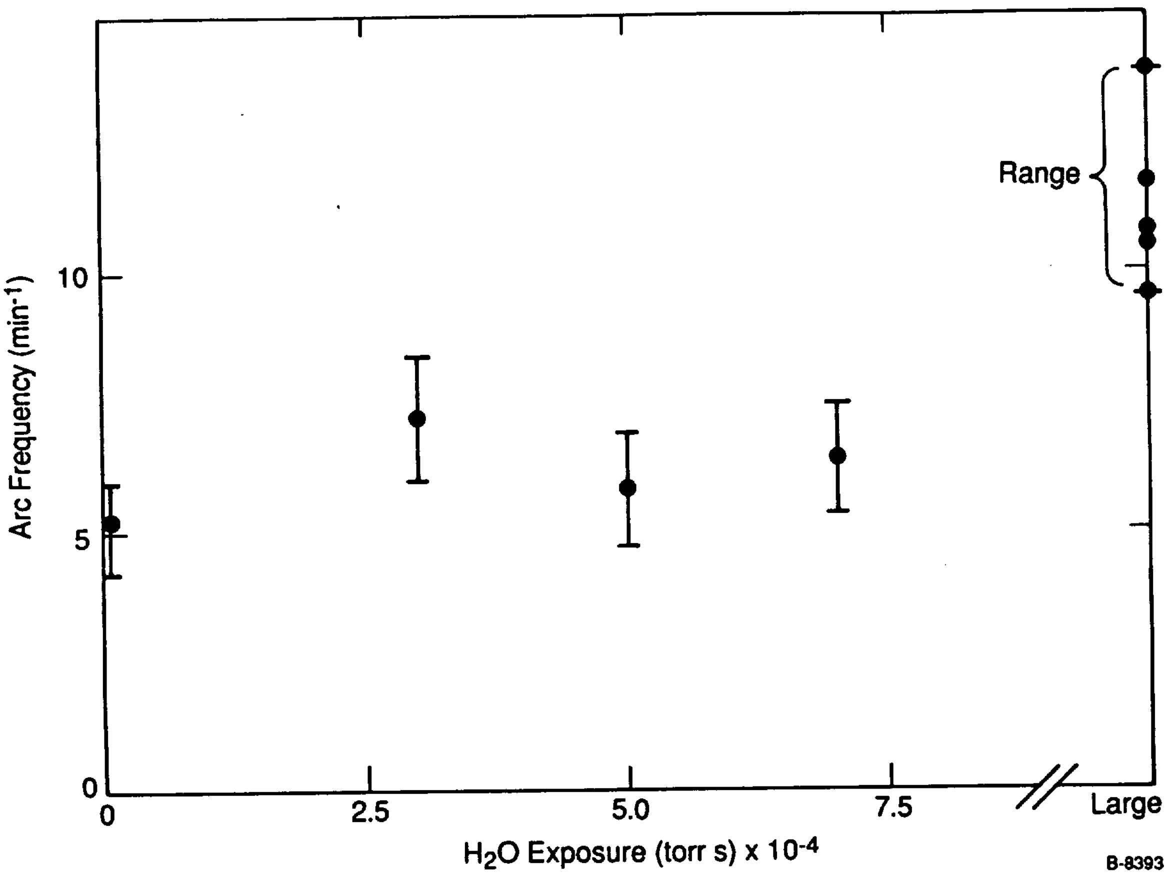

Figure 57. - Al-plate arc frequency sensitivity to H_2O exposure.

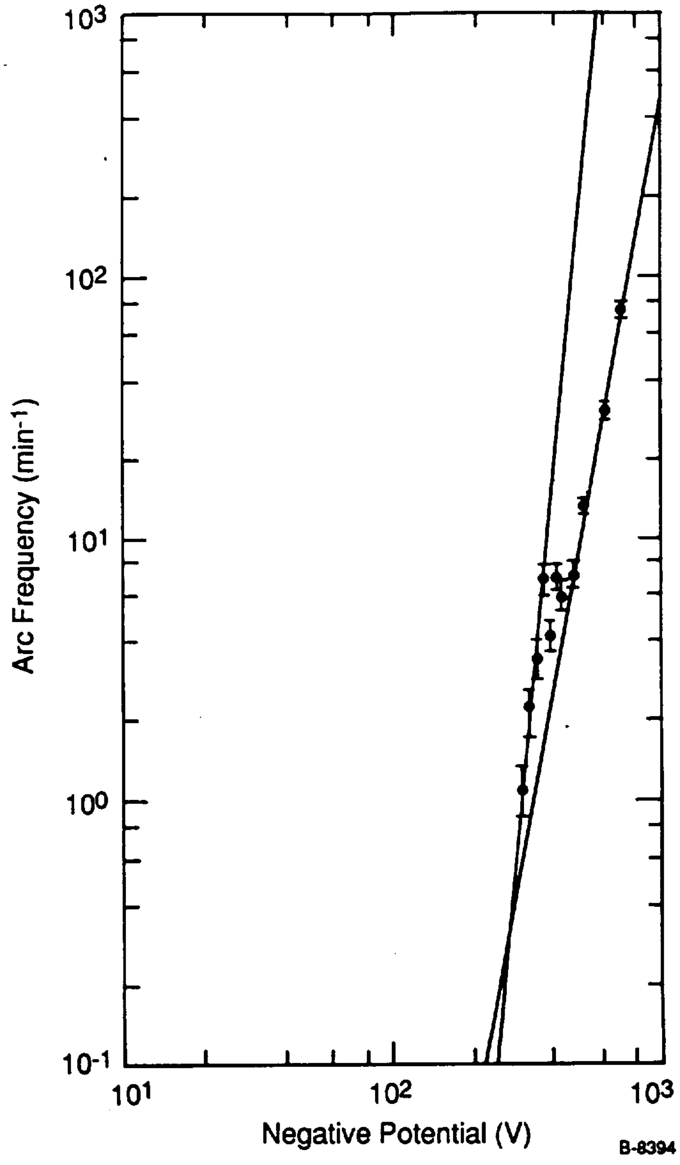

Figure 58. - Arc frequency of drill induced damage spot on Al-plate.

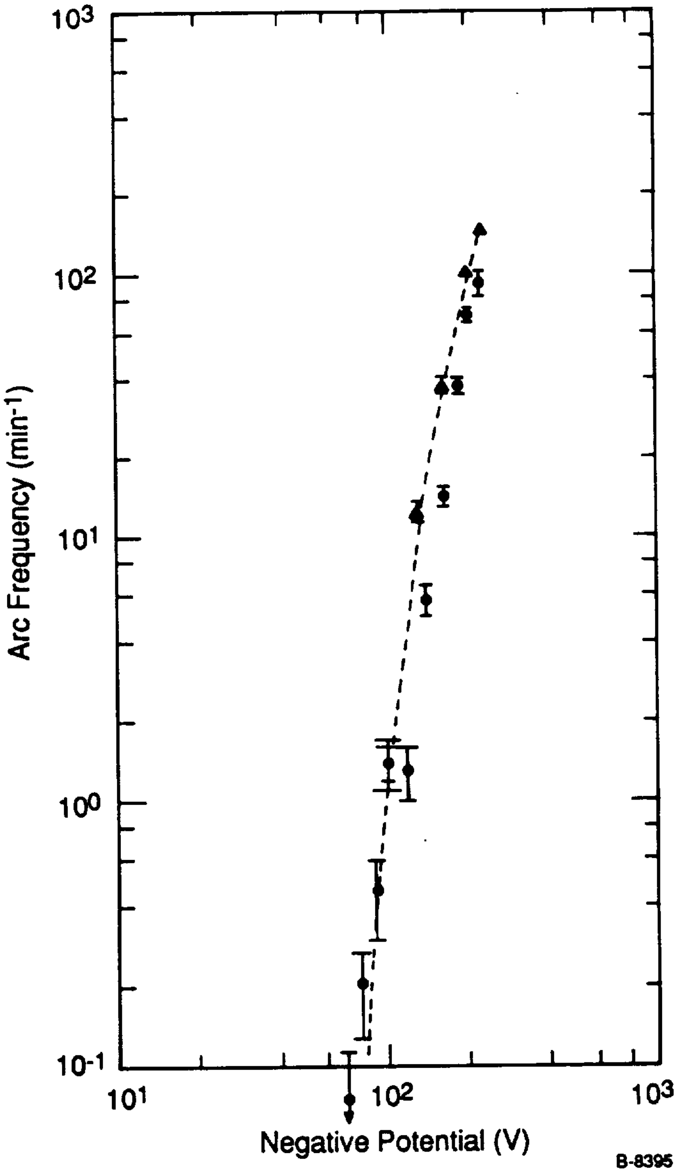

Figure 59. - Arc frequency of Al-plate cut edges.

The anodized aluminum plate arcing thresholds are consistent with the information provided by Grier and Snyder[28] when we received this test plate, but additional information was obtainable. Testing a drill bit induced damage spot and the cut Al-plate edges clearly shows that arcing is sensitive to coating imperfections. The arcing threshold progressed to smaller negative potentials as the coating damage became more severe. Hence, even a perfectly coated plate in a space environment could become damaged by debris or micrometeorites and begin to exhibit arcing at potentials as low as -70V.

4.5 Micrometeorite Impact Simulation and Arcing

A utilized a pulsed Nd:YAG laser system operating at 1.06 μm was used to simulate a micrometeorite impact on our Al test plate. Laser simulation of micrometeorite damage is not new.[29] In fact, PSI personnel performed some pioneering work in this area[30-32] in the mid 1970's. The key factors required for accurate impact simulation are: 1) matching the laser pulse energy to the kinetic energy of the incoming particle; and 2) matching the momentum of the material ablated from the surface by the laser to the momentum of the incoming particle. The latter objective is most difficult to achieve since the momentum coupling will be a function of the heat of ablation of the material and the absorption depth at the laser wavelength. Often it is not possible to satisfy both the energy and momentum requirements simultaneously while preserving the size scale of the impact site. Typical damage sites are characterized by cratering and spallation. In our single test plate, we focused the output of the laser to a spot size of ≤ 500 μm. Utilizing an intensity of 2.4 J/cm^2 in a single Q-switched pulse, we generated a damage spot ~ 650 μm in diameter. The damage appeared to penetrate through the Al_2O_3 coating (absorption depth ~ 25 μm), but caused very little underlying Al removal or spallation. A microscope picture of the damage is shown in Figure 60.

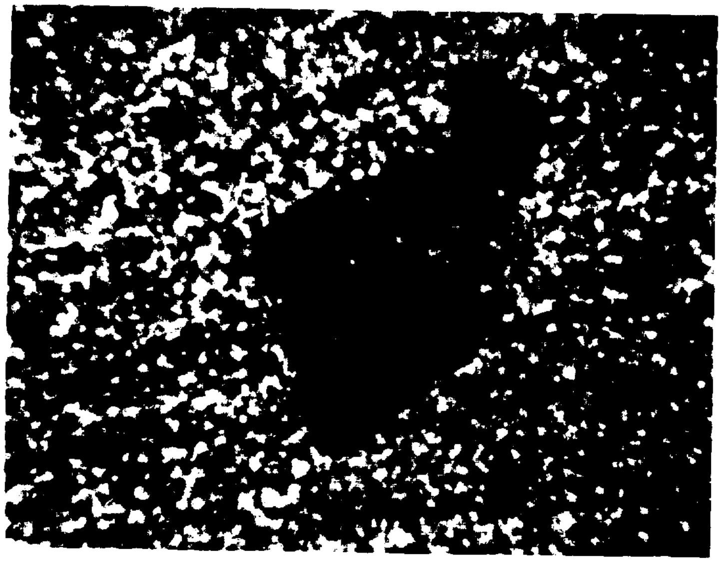

Figure 60. Laser simulated micrometeorite impact damage (~ 650 μm) on the Al test plate.

Our failure to create typical spallation is a result of using too large a spot size compared to the surface absorption depth. The damage generated is less severe than that anticipated by the impact of a 0.17 μg iron core micrometeorite colliding with the same Al-plate at a velocity of 7.6 km/s. The frequency of such impacts in space in this size/velocity range is 1 to 10 m^{-2} $year^{-1}$. The subsequent arc testing of this damage spot is presented in Figure 61. The threshold is between -120 and -130V. Damage generated by even small, 0.2 μg, micrometeorite impacts on this Al-plate will exhibit arcing at voltages significantly below the uniform/perfect plate test potential and below the expected floating potential of the space station truss. It is likely that arcing at a true micrometeorite impact point would occur at a voltage more similar to the cut edge, -70V.

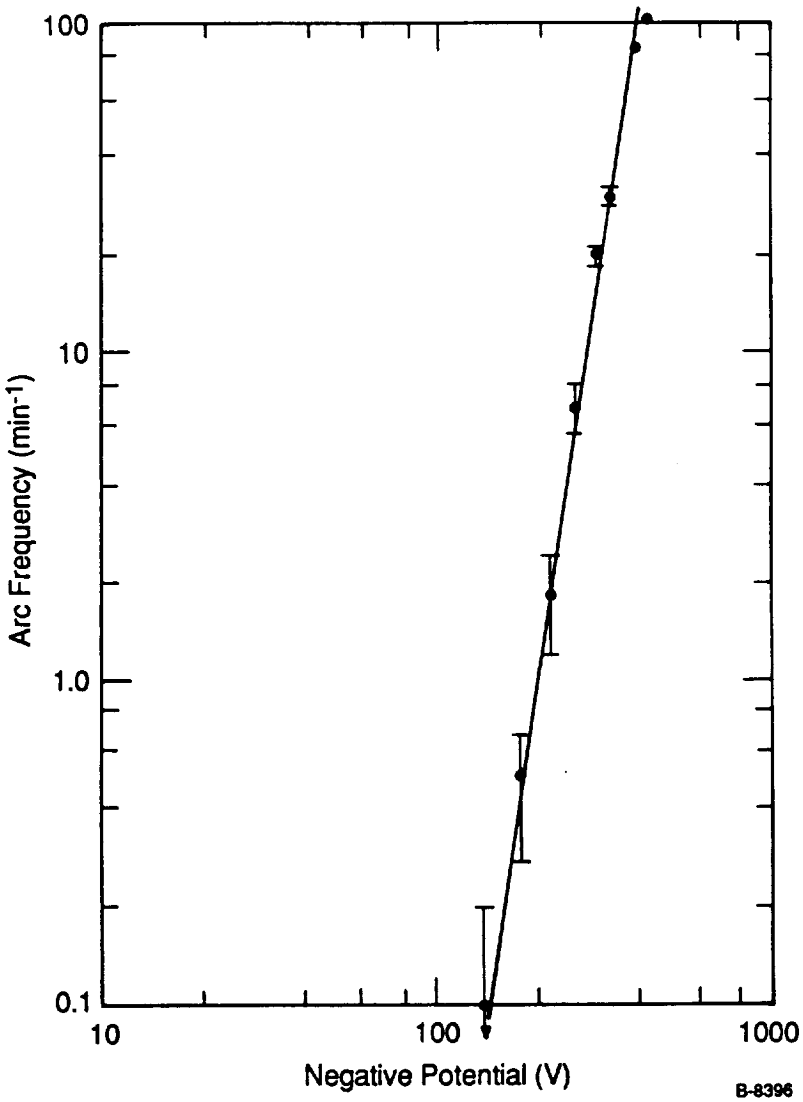

Figure 61. Arc frequency of laser simulated micrometeorite damage on Al-plate.

4.6 Atomic Oxygen Healing of Al-Plate Damage Sites

Two different damage spots, laser simulated micrometeorite and cut edges, were subjected to a fluence of more than 10^{19} O-atoms/cm^2 impinging at a 45 deg angle from the atomic oxygen source. This is roughly the equivalent of ~6 hr on orbit. These damage spots were subsequently tested for arcing and compared to arcing rates observed before O-atom exposure. Figures 62 and 63 present the post O-atom exposure arc frequency versus voltage curves for cut edges, and micrometeorite damage, respectively. There is a slight indication that the threshold may have shifted to smaller negative potentials in each case, but the uncertainty is sufficient to argue that no change was induced by O-atom impact. Microscope inspection of these damage spots after O-atom exposure showed no discernable

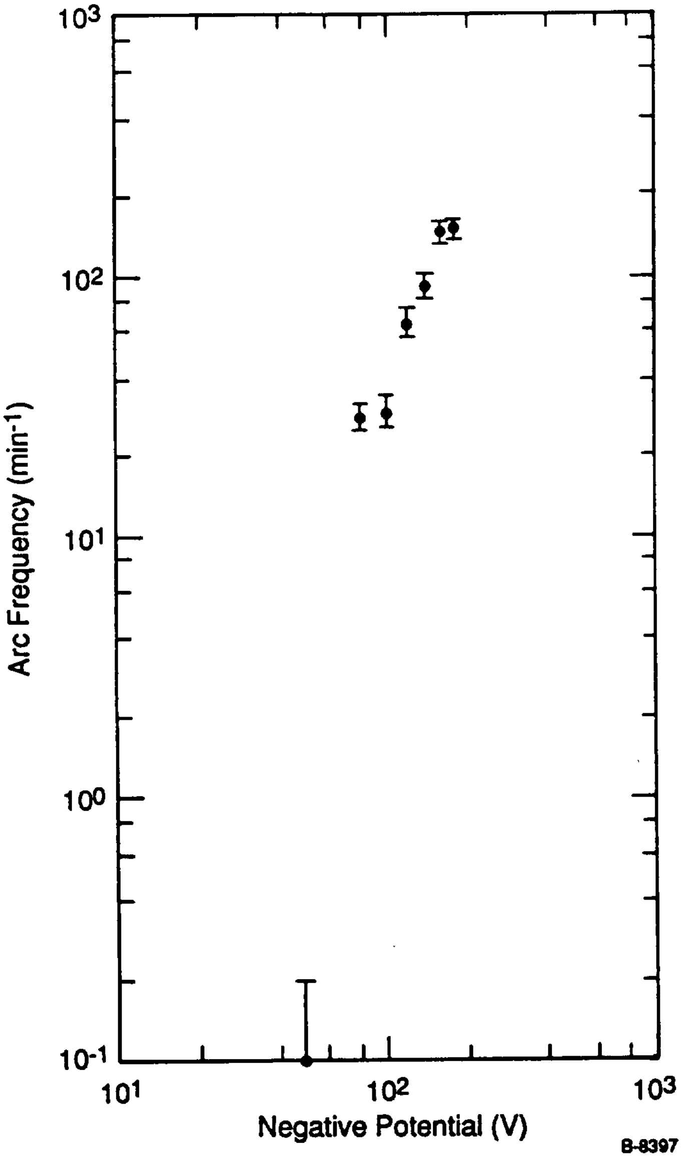

Figure 62. Arc frequency of cut edges of Al-plate after O-atom exposure.

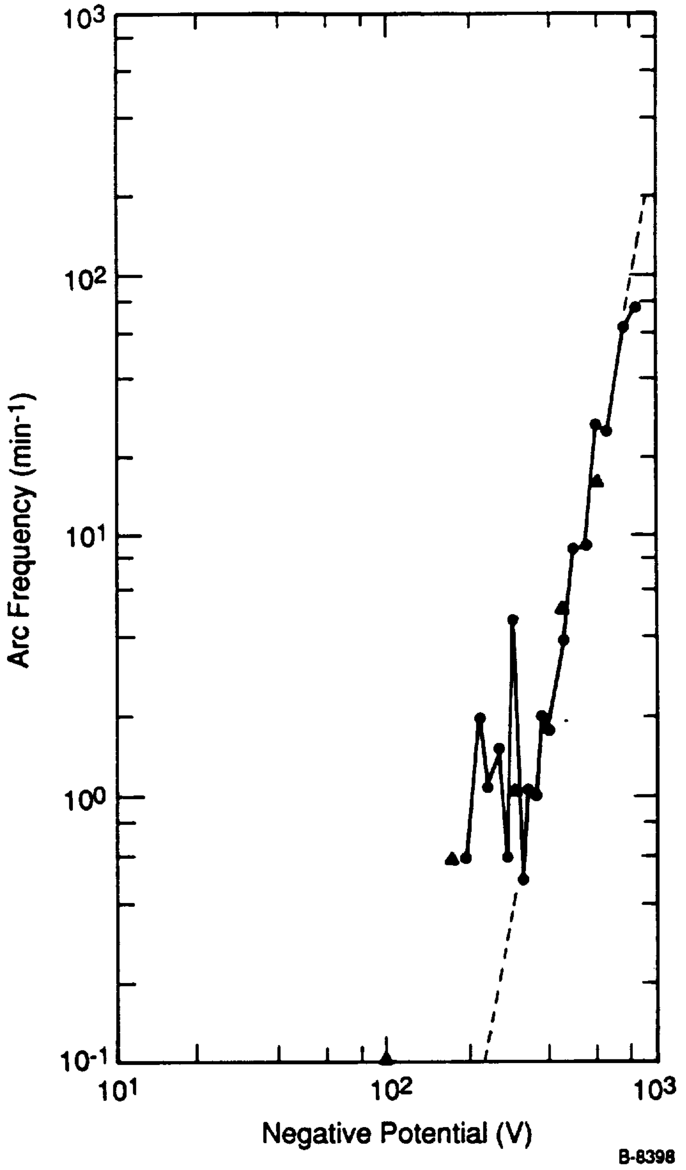

Figure 63. - Arc frequency of laser simulated micrometerorite damage after O-atom Exposure.

changes. These results are consistent with our knowledge about the properties of thermal oxide layers. These films seldom grow thicker than 30Å and there is little reason to believe that the translational energy found in orbital atomic oxygen would have an order of magnitude impact on the diffusion processes which control film growth in depth. Data presented in Figure 45 for the breakdown voltage of oxide coatings clearly demonstrate a threshold well below 100V for a thermally grown oxide layer.

5. THEORY AND MODELLING OF SOLAR CELL ARCING

In Phase I of the effort SBIR we identified two mechanisms for initiation of the arcing:[15,16] field emission followed by explosion of whiskers protruding from the interconnect surface, and dielectric breakdown of a thin insulating layer (e.g., oxide layer). The initiation would occur near the triple junction, which is the line where insulator and conductor meet. Once the arc is ignited, the maintenance of the discharge would occur through a complex mechanism involving desorption of gas off the cover plate surface. Electrons leaving the interconnect would hop along the surface of the dielectric and avalanche, with new electrons generated by secondary electron emission, and by impact ionization of molecules/atoms desorbed from the surface.

The theoretical effort that was carried out during the first year of the Phase II effort was geared to validating both the ignition and the maintenance mechanisms that had been postulated. For the whisker hypotheses to be valid there must be a field in excess of 10^8 V/cm at the tip of the whisker.[15] At such a field the field emission current flowing through the whisker is sufficient to make it vaporize and initiate a discharge. Since the field amplification factor at the tip (based on previous experimental studies) cannot exceed 300, there would have to be an average field of $10^8/300 = 3 \times 10^5$ V/cm in the vicinity of the triple junction. Now, the experimental threshold for arcing of negatively biased solar cells has been found to be $\simeq 300$V. For a cover slip thickness $d \simeq 0.15$ mm, the field at the triple junction would be $\bar{E} = |V|/d = 2 \times 10^4$ V/cm, i.e., more than a factor of one hundred too small. Some charging mechanism of the side of the cover plate such as ions from the plasma impinging on the side surface or secondary electron emission from the surface could be the cause of much larger field strengths near the triple junction. We modified and implemented a particle in cell (PIC) code to study the charging of the cover plate and see whether enhanced fields near the triple junction were possible. The results of the computer calculations described below were negative. However, all possible charging mechanisms were implemented in the code. Later efforts considered the effect of secondary electrons leaving the interconnect. These electrons could, after hitting the side of the cover plate, cause a positive charging due to secondary electron emission. The implementation of that effect was conducted during the second year and is described in Section 4.4.

The model of a neutralization front moving along the surface of the cover glass that was developed earlier[16] requires that the ions generated in the desorbed gas flow to the interconnect and not fall onto the cover plate. We solved Poisson's equation for the field above a partially neutralized cover plate and found that the electric field behind the neutralization front is directed into the dielectric, thus ions will fall onto the cover glass. The calculations that are presented below thus put in doubt the previously developed model. A careful reading of the literature on vacuum arcs has led us to believe that there must be a plasma flare in the vicinity of the initial ignition site where all the ions and electrons necessary to maintain the discharge current are generated.

5.1 Calculation of Fields Around the Triple Junction

Initial investigation involved the implementation of a particle-in-cell (PIC) code. This code was developed at MIT by Mengu Cho, who modified a 1D code as described in Reference 33, in order to make the code two-dimensional in space. The code named REPDWG is a 2-1/2D (two-dimensional in real space, three-dimensional in velocity space) particle in cell code. Use of a two-dimensional in space code is justified if the thickness of the cover plate and the sheath thickness (once the cover plate is charged) are much smaller than the length of the triple junction (width of interconnect or width of solar cell). In a solar array the length of the triple junction is equal to the width of the interconnect which is typically 2 to 3 mm, i.e., an order of magnitude less than the thickness of the cover plate. The sheath thickness, however, under LEO conditions will be in the range of 0.3 to 3 cm, which is not smaller than the width of the interconnect. The use of a two-dimensional code is therefore not truly justified under such conditions. The laboratory experiments, however, have been carried out with plasma densities in the 10^6 to 10^8 cm^{-3} range. The length of the interconnect for the samples tested will be the length of the cover plate, i.e., 1 cm. The two-dimensional code will be well suited, therefore, for modeling the laboratory experiments. One must note, however, that before the cover plate is charged the array is attracting ions from a much larger distance than the final sheath dimensions. The initial charging of the cover plate, and especially of the side of the cover plate will not be well modeled by a two-dimensional particle in cell code. Near the end of the charging period, however, ions are attracted over distances of the order of the final sheath dimensions, so that the final charging phase and final charge distribution on the cover plate should be adequately modeled by the code. Conditions for arcing near threshold, when the cover plate sits for a long time in its charged state before initiation of a discharge, should be well described by the two-dimensional PIC code.

The code REPDWG allows a plasma flow in the x direction and takes periodic boundary conditions in the y direction, which is along the cell (or cover plate). At one of the boundaries perpendicular to the flow two dielectric plates are placed, separated by a recessed conductor as shown in Figure 60a. REPDWG solves Poisson's equation both in the plasma and in the dielectric as well as the equations of motion of the charged particles. Since the fields are expected to be very large and to vary appreciably inside and outside the dielectric near the triple junction, a variable mesh has been incorporated in the grid structure. When a charged particle is incident on the dielectric the dielectric will charge and also, possibly, emit secondary electrons. This has been incorporated in the boundary conditions.

REPDWG has the capability to start with some assumed charge density on the dielectric as well as to restart from the results of a previous run.

5.1.1 Code results. - Figure 64b shows a typical computational grid for REPDWG. The grid is a 48 x 48 non-uniform mesh. Grid cells are highly clustered in the dielectric and near the triple point. In Figure 64, the dielectric plates are at the bottom, start at cell boundary 21 in the y direction and have 16 cell boundaries in each plate in the y direction.

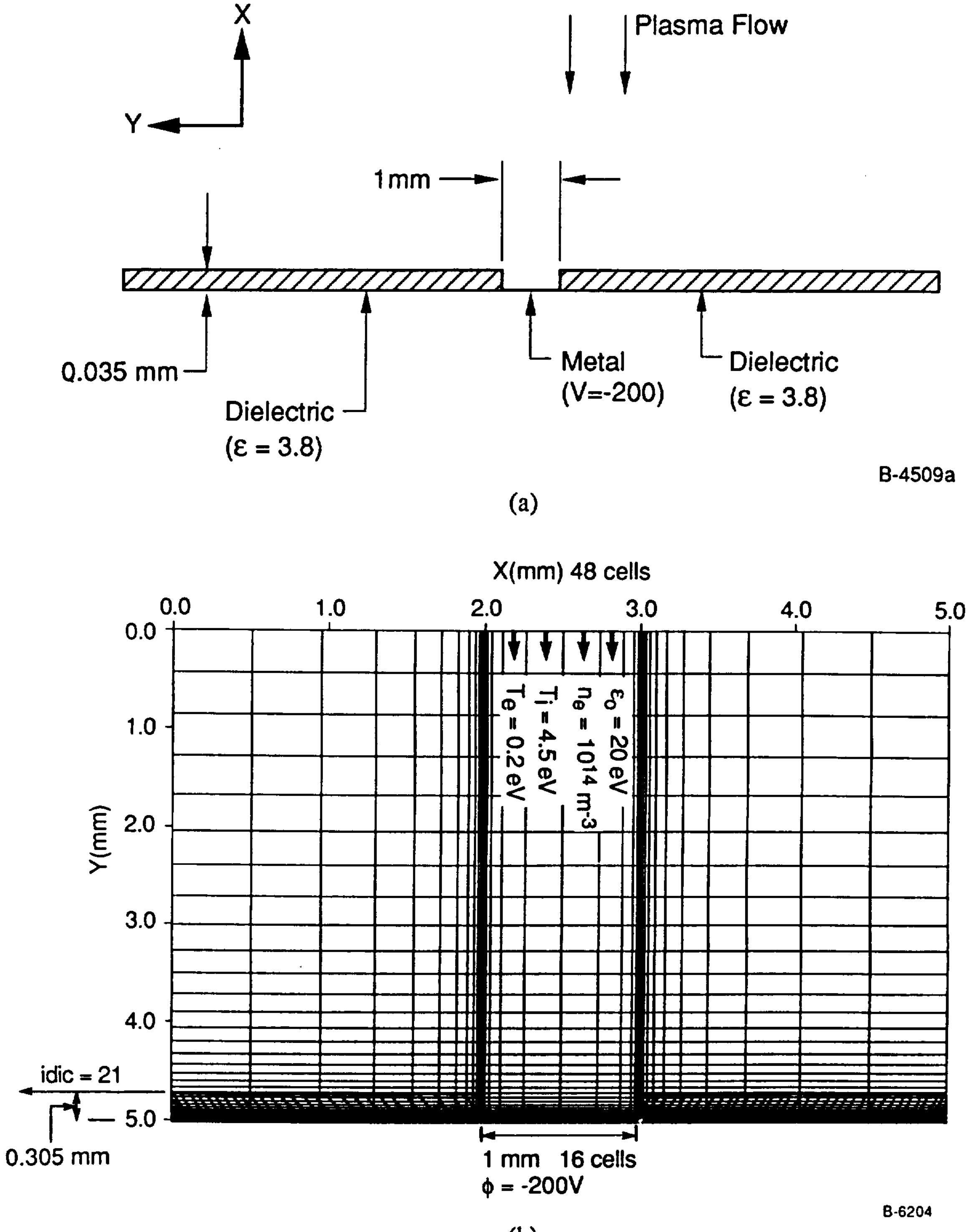

Figure 64. - Geometry for calculating charging of cover plates. (a) Geometry; (b) Grid structure.

The length of the computational region is 48 mm in the x direction and 21 mm in the y direction. The spacing between adjacent cells was taken to be 1 mm and the dielectric constant of each cell was taken to be $\epsilon = 3.8$, corresponding to SiO_2. The plasma conditions were: ion directed energy, 20 eV; ion temperature, $T_i = 4.5$ eV; ion density, $n_i = 10^{14}$ m^{-3}; electron temperature, $T_e = 0.2$ eV. The size of the computational box was 5 mm x 5 mm which is large compared to the electron Debye length $\lambda = 0.33$ mm. The sheath thickness based on the Child Langmuir's current density limitation for ions,[34]

$J_i = n_i e\sqrt{T_i/2\pi m_i}$, was 1.8 mm, which is also smaller than the size of the box chosen. Simulations were run with ion-to-electron mass ratio $m_i/m_e = 25$ and a time step of $0.2\ \omega^{-1}_{pe}$, where ω_{pe} ($= 5.6 \times 10^8$ s^{-1}) is the electron plasma frequency.

We studied the charging of the dielectric when the ion beam velocity was normal to the cells and at an angle of 45 deg with respect to the normal. We also studied the effect of secondary electron emission on the charging. Results for ions incident normally are shown in Figures 65 through 72. Figures 65 and 66 show the equipotential contours and the potential along a horizontal line in the x direction just grazing the top of the dielectric at a time $t = 10\ \omega_{pi}^{-1}$. One sees from Figure 65 that the sheath edge is 1.8 mm above the interconnect and that the lateral width of perturbed potential due to the exposed interconnect is 1.46 times the width of the conductor. We see from Figure 66 that at time $t = 10\ \omega_{pi}^{-1}$ the areas of the cover plate near the interconnect have charged up enough so that the potential is near 20V and the cover plate is starting to repel ions. For a voltage change of ΔV the time to charge is $\Delta t = C\Delta V/I = (\epsilon/\epsilon_0)(\epsilon_0/d)\Delta V/j$. For the plasma simulated, $\epsilon/\epsilon_0 = 3.8$, $\epsilon_0/d = 2.9 \times 10^{-8}$ F/m^2, $j = 0.16$ A/m^2 so we have $\Delta t = 7.03 \times 10^{-7}\ \Delta V$ seconds.

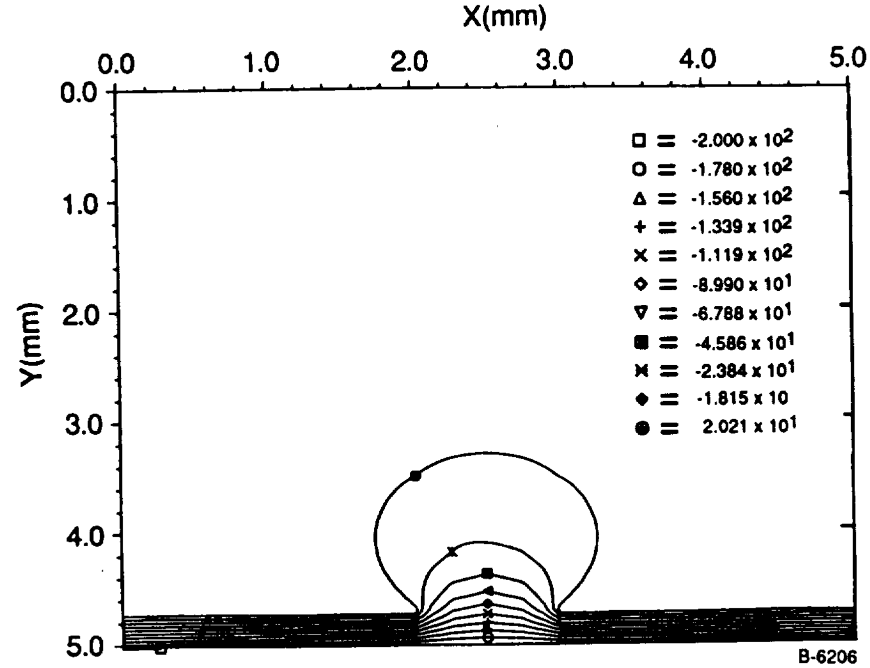

Figure 65. - Potential contours at $t = 10\ \omega_{pi}^{-1}$.

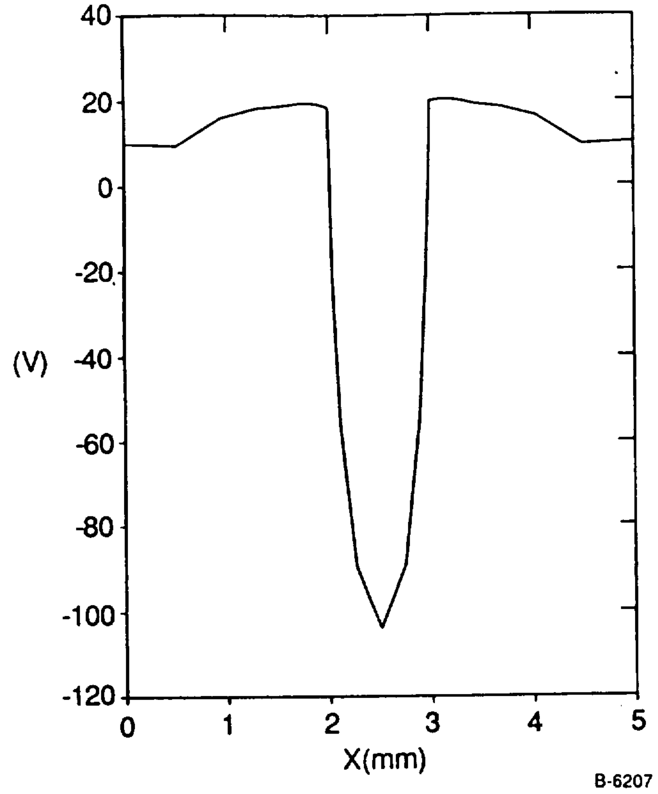

Figure 66. - Potential along a line grazing the surface of the cover plate at $t = 10\ \omega_{pi}^{-1}$.

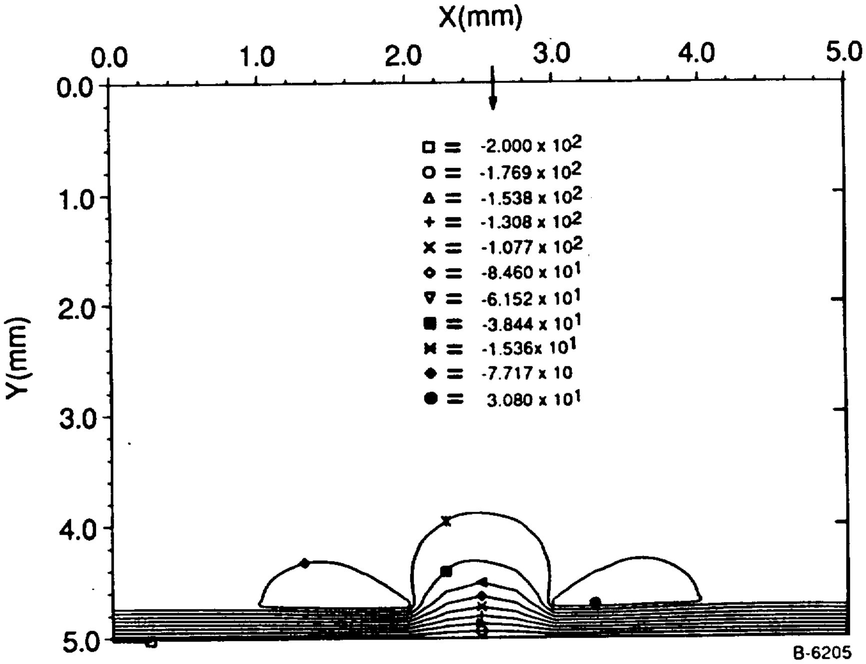

Figure 67. - Potential contours at $t = 100\ \omega_{pi}^{-1}$.

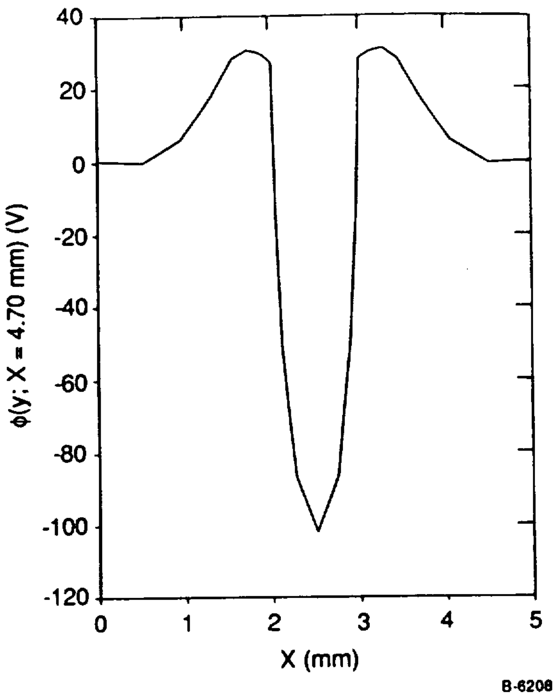

Figure 68. - Potential along a line grazing the surface of the cover plate at t = 100 ω_{pi}^{-1}.

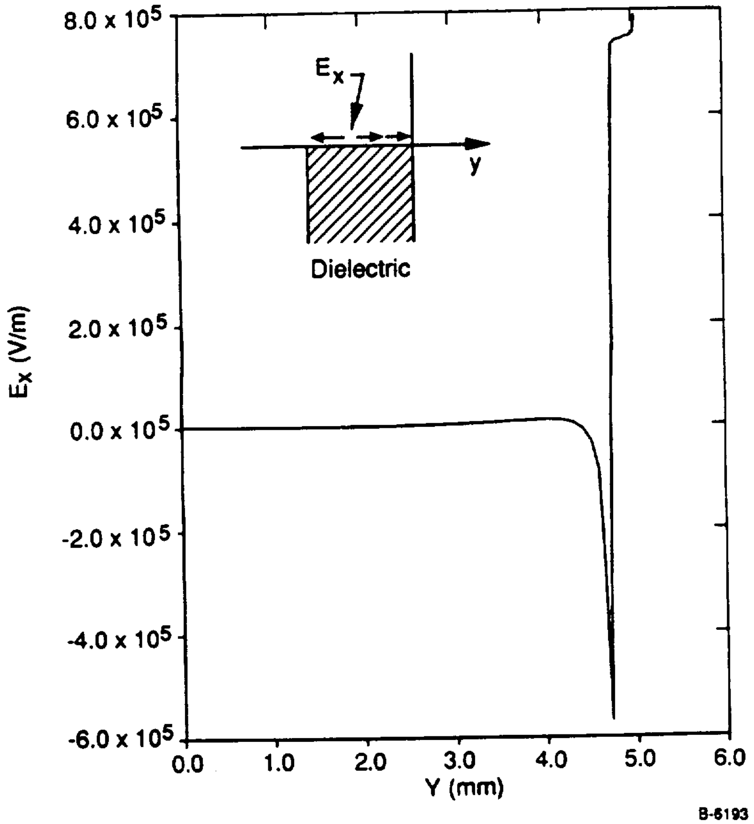

Figure 69. - Electric field in y direction along a vertical line passing through the triple junction, t = 100 ω_{pi}^{-1}.

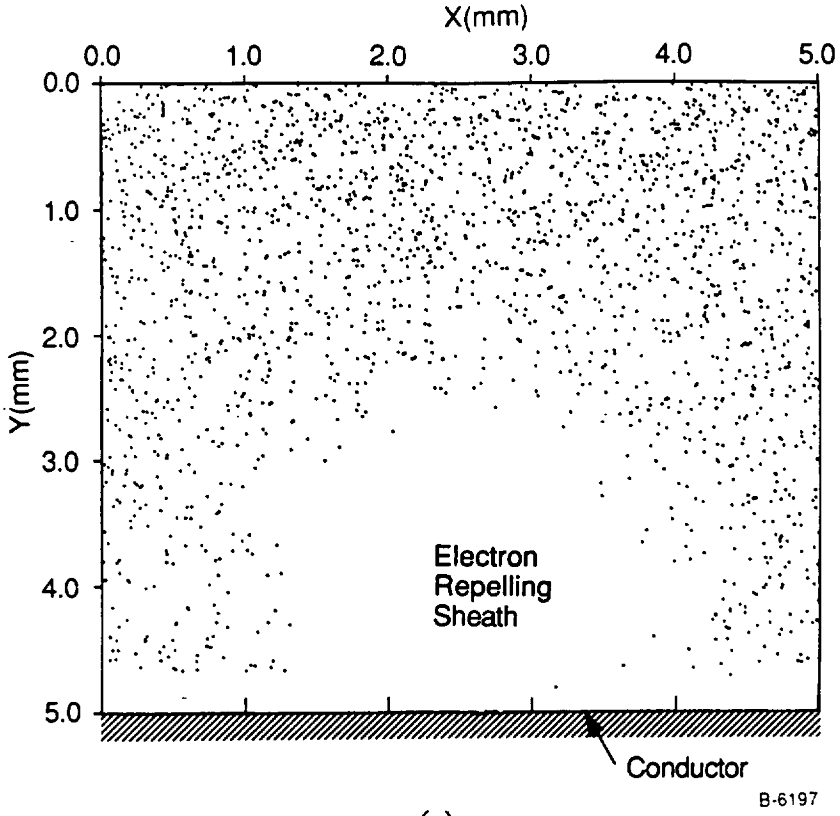

(a)

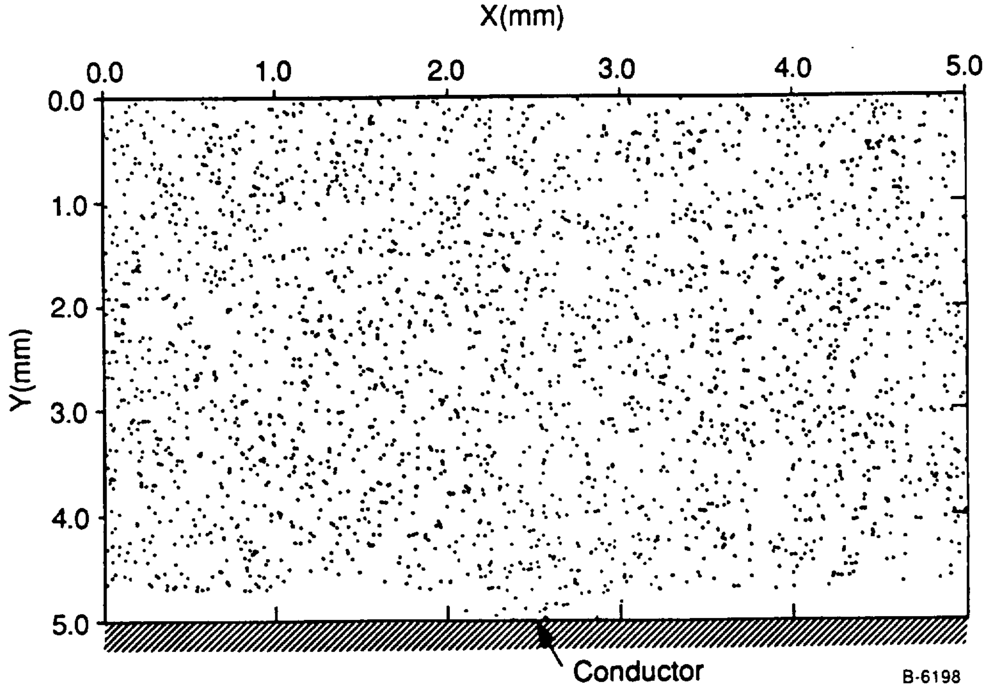

(b)

Figure 70. - Distribution in space of particles. (a) Position of electrons at t = 100 ω_{pi}^{-1}; (b) Position of ions at t = 100 ω_{pi}^{-1}.

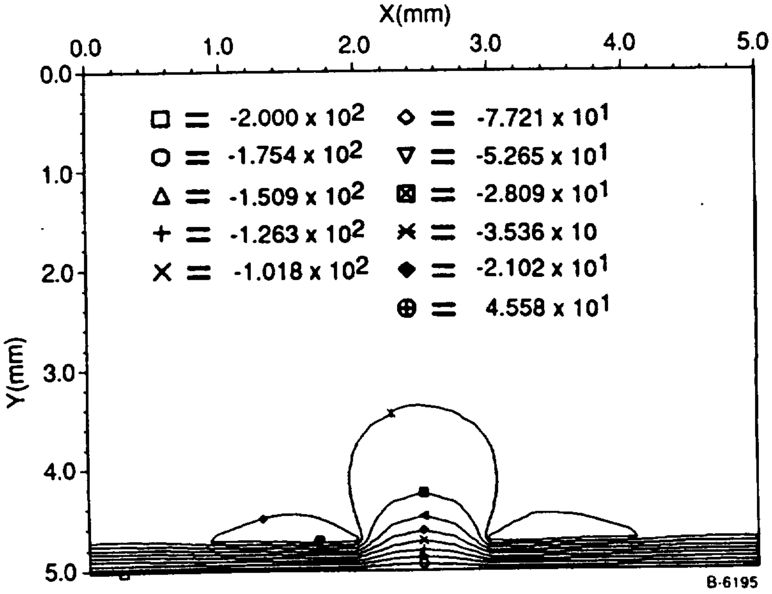

Figure 71. - Potential contours with secondary electron emission at t = 100 ω_{pi}^{-1}.

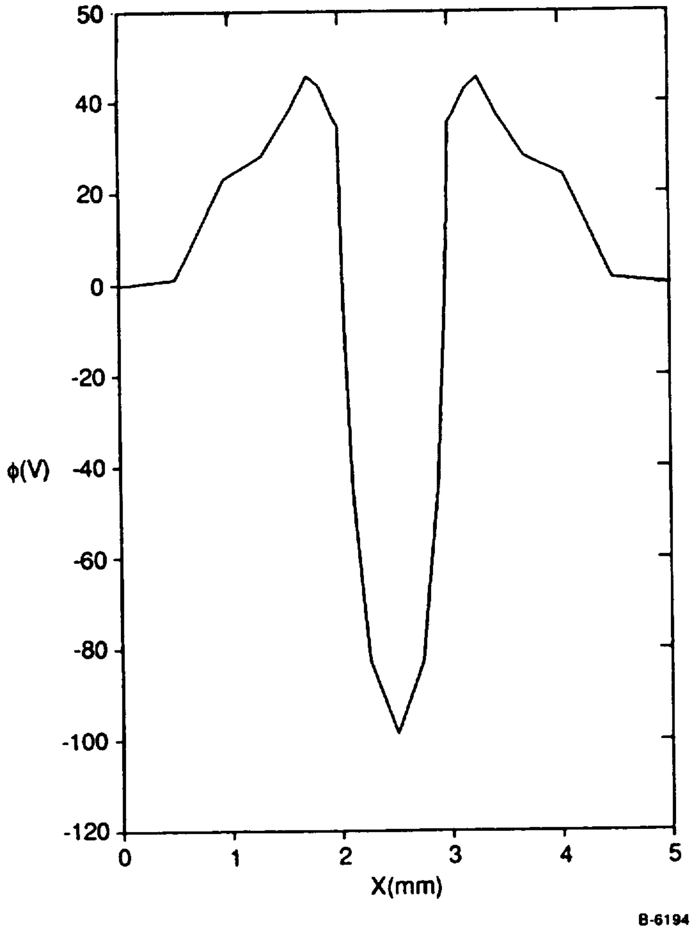

Figure 72. - Potential along horizontal line grazing the top surface of the cover plates, at t = 100 ω_{pi}^{-1} with secondary electron emission.

For this plasma, $\omega_{pi} = 2.09 \times 10^6$ rad/s so $\Delta t\omega_{pi} = 1.47\ \Delta V$. Therefore, since the dielectric surface is expected to have a potential of about 20V, to see a change to this potential from ground would take approximately 30 ω_{pi}^{-1}.

In order to ensure that the dielectric had enough time to charge and come to equilibrium, simulations were run to 100 ω_{pi}^{-1}. A comparison of Figures 65 and 67 indicates that maximum positive potential has increased. This is due to the (relatively) high ion temperature which means that the dielectric has to come to a sufficiently positive potential to reduce the ion flux. In addition, the maximum lateral range of the potential contours from the conductor has diminished. For Figure 65, the effective area of the conductor was 1.46 times the actual area. This enhances the collected current to the conductor. In Figure 67, the effective area of the conductor is the same as the actual area. There has been a pitching of incoming ions due to the enhanced charges collected by the cover plate in the vicinity of the triple junctions. The potential along a horizontal line grazing the surface of the cover plates is shown in Figure 68, and clearly indicates the presence of excess charge near the interconnects. Figure 69 shows the electric field along a vertical line passing through the triple junction. The electric field reaches a maximum value of approximately 8×10^5 V/m. The initial electric field along the side face of the dielectric was $E_x = -V/d = 6.6 \times 10^5$ V/m. Therefore an increase in potential of the top surface of the dielectric results in an increase in the electric field. In Figure 70a and 70b, the particle positions are shown for $t = 100\ \omega_{pi}^{-1}$. The electrons in Figure 70a are excluded from the sheath region but do strike the outer edges of the dielectric.

In Figure 71, we show the potential contours for the two dielectric plates when allowance is taken for secondary electron emission from the dielectric. We used the following expression for secondary electron emission:[35]

$$\eta = 0.66\ \eta_{max} \frac{E}{E_{max}} \exp - \left(\left[\sqrt{\frac{E}{E_{max}}} - \sqrt{2} \right] \right) , \qquad (5\text{-}1)$$

where η is the secondary electron emission coefficient and E the energy of an electron hitting the surface. For SiO_2, we have $E_{max} = 240$ eV and $\eta_{max} = 2.4$. For the calculation presented here the source of electrons is the space plasma, and the electron energy upon impact is quite small ($E << 1$ eV). At the beginning of a discharge, however, the main source of electrons will come from field emission sites near the triple junctions. This emission was considered in later calculations. The effect of secondary electron emission is seen to be quite noticeable, as can be seen by comparing Figures 68 and 72. The overall sheath distance increases with secondary electron emission as the low energy electrons emitted from the dielectric to some extent neutralize the incoming ion current.

The effect of angle of irradiance is shown in Figures 73 and 74. These figures correspond to calculations where the ions are coming in at an angle of 45° with respects to the surface. The potential distribution is skewed along the dielectric but remains symmetric

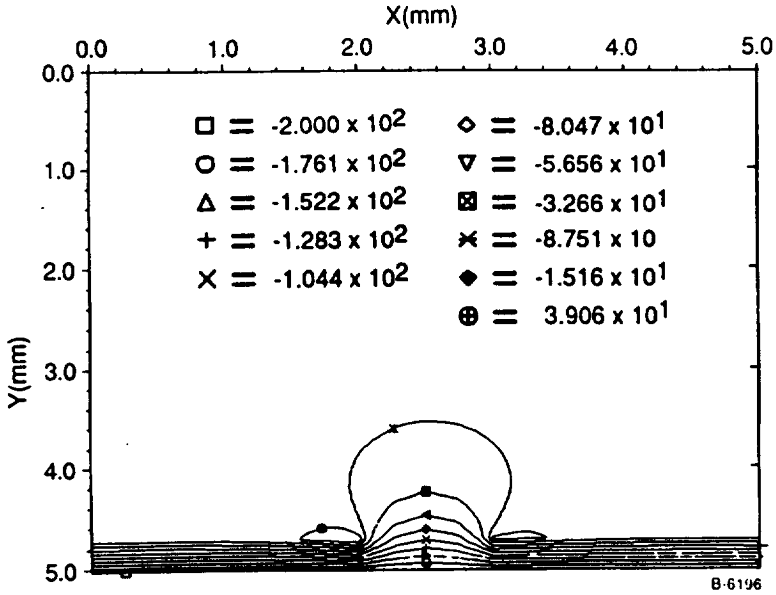

Figure 73. - Potential contours at $t = 100\ \omega_{pi}^{-1}$, 45 deg angle of irradiance.

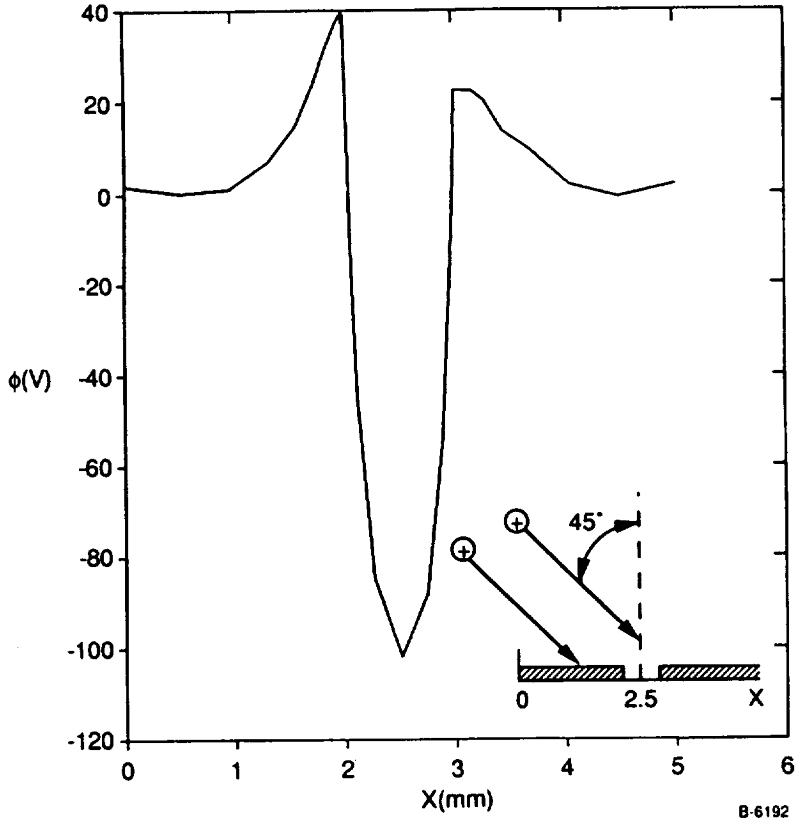

Figure 74. - Potential along horizontal line grazing the top surface of the cover plate at $t = 100\ \omega_{pi}^{-1}$, 45 deg angle of irradiance.

over the conductor. This is clearly seen in Figure 74 where the dielectric struck last by the ion flow does not rise to such a high positive potential because it is, to some extent, shielded from the ion stream. The y directed electric field along the side of dielectric was found to differ insignificantly from the previous simulations with normal incidence of ions.

We used the results of the PIC code to determine whether the fields in the vicinity of the triple junction are large enough to trigger a discharge. The code results indicate a field strength of 8 x 10^3 V/cm in the vicinity of a triple junction when the interconnect voltage is -200V. If we assume that a whisker is present near the interconnect with a field enhancement factor at its tip of 200, then the field at the tip would be 1.6 x 10^6 V/cm which is a factor of 20 below the value (E ~ 3 x 10^7 V/cm) where field emission currents begin to appear. The code results therefore seem to negate field emission and whisker explosion as a possible cause of discharge ignition at V = -200V., Even at a bias voltage of -800V, where we have experimentally observed arcing, the field is a factor of five lower than required for arc initiation via the proposed mechanism.

It was recognized that this factor of five could be due to positive charging of the side of the cover plate by secondary electron emission. It has been well established that energetic ions ($\epsilon \geq 200$ eV) hitting a metal surface (interconnect) can generate secondary electrons with an efficiency of 10 to 15 percent. These secondary electrons would be accelerated away from the interconnect and those few hitting the side of the cover plate could cause it to charge positively by secondary electron emission. This effect was considered in taler development of the theory.

Another result of the PIC calculations is the determination of the capacitance of the array with respect to the space plasma. The charge density, σ, on the interconnect is related to the electric field E through the relation $\sigma = \epsilon_0 E$ where ϵ_0 (= 8.84 x 10^{-12}) is the permittivity of space. Thus, integration of the electric field over the surface of the interconnect will yield the total charge, and, after division by V, the capacitance. A rough estimate of this capacitance by taking the upper bound value E = 8 x 10^5 V/m, which is the value at the interconnect (Figure 65) and taking E to be constant over the 1 mm x 1 cm area of the interconnect. This gives a charge Q = 7 x 10^{-11}C and a capacitance C = Q/V = 7 x 10^{-11}/200 = 0.3 pF. A more exact result, obtained by averaging the field over the area of the interconnect, is a factor of three lower, C = 0.1 pF.

5.2 Calculation of Potential and Electric Fields as a Function of Surface Charge on the Cover Plate

The discharge model that we proposed in our early work was based on a surface discharge front propagating along the cover plate. The front is triggered by a burst of electrons emanating from the interconnect triple junction. These electrons, upon hitting the surface of the dielectric, desorb gas which is rapidly ionized by electron impact. Ionization of the gas is essential in maintaining the discharge. There are two primary conditions that have to be met for the validity of the model. First, the direction of the electric field in the front has to be such that the secondary electron emission coefficient of the surface for electrons is near unity. Second, the ions generated in the gas layer above the surface must find their way to the interconnect without falling back onto the surface of the cover plate. In order to verify whether such a front can satisfy these two conditions, we calculated the field above the cover plate assuming the existence of such a front. The details are presented below. The results of our calculations show that the field behind the front is directed *towards* the surface, pulling the positive ions back onto the surface. Because of this finding we believe that most of the ionization, the source of the neutralization current, must occur on the interconnect, near the triple junction.

In the calculations we consider the geometry of a dielectric of thickness d and length L lying above a conducting plane biased to a negative potential, -V. We assume a two dimensional problem, i.e., that the width of the cover plate is infinite. The surface of the cover plate has a charge density σ_+, which is a function only of the coordinate x. The geometry is shown in Figure 75. If we neglect the effect of charges on the edges of the cover plate at x=0 and x=L, we find that the potential inside the dielectric is given by (in e.s.u. units):

$$\phi(x,z) = \frac{1}{\epsilon}\int_0^L \sigma_+(x') \ln\left[\frac{(x-x')^2 + (2d+z)^2}{z^2 + (x-x')^2}\right] dx' - V \quad . \qquad (5\text{-}2)$$

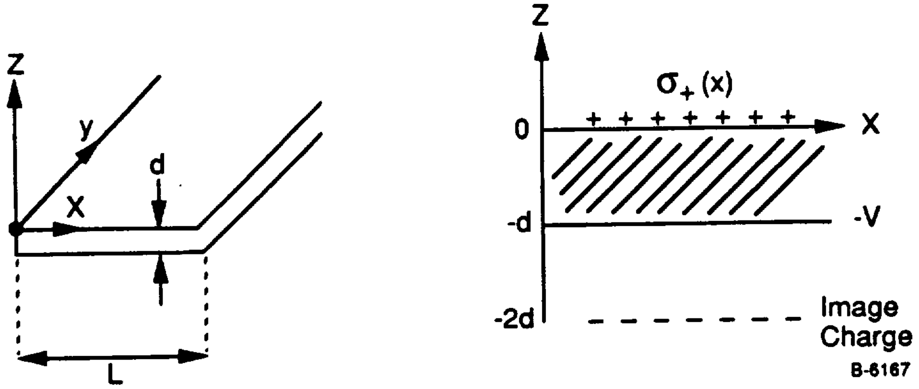

Figure 75. - Geometry for calculating electric field and potential on the cover plate.

The electric field just above the cover plate, has components E_x and E_z given by (in e.s.u. units)

$$E_x(x) = \frac{8d^2}{\epsilon} \int_0^L \frac{\sigma_+(x')dx'}{4d^2(x-x') + (x-x')^3} \tag{5-3}$$

$$E_z(x) = -4d \int_0^L \frac{\sigma_+(x')dx'}{4d^2 + (x-x')^2} + 2\pi\sigma_+(x) \quad . \tag{5-4}$$

The derivation Eqs. (5.2) through (5.4) can be found in Reference$^{\mathrm{REF}}$. Equations (5.2) through (5.4) are expected to be good approximations to the potential and fields of a solar cell having finite dimensions in the x and y direction if $d/L << 1$ and if the location x is not too close to the edge, i.e., $x/d >> 1$ and $(L-x)/d >> 1$. Our derivation neglects the effect of polarization of the dielectric near its edges. This could eventually be corrected for by an iterative proce-dure, i.e., by evaluating the fields at the edge of the dielectric from the gradient of Eq. (5.2) and evaluating the resulting polarization, which would then be used for the next iteration.

We evaluated Eqs. (5.2) through (5.4) for the specific charge density profile

$$\sigma_+(x) = \frac{\sigma_M}{2}[1 + \tanh\alpha(x-x_0)] \tag{5-5}$$

where

$$\sigma_M = -\frac{\epsilon V}{4\pi d} \quad . \tag{5-6}$$

σ_M is the surface charge density that a fully charged capacitor of dielectric constant ϵ and having distance between plates d would have if it were sustaining a voltage V. The profile given by Eq. (5.5) is expected to be representative of a discharge front propagating along the surface of the dielectric, with $\sigma_+ \simeq 0$ for $x << x_0$. The parameter α represents the inverse of the scale length of the front. The profile given by Eq. (5.5) is plotted in Figure 76. Results for the conditions $V = 800V$, $\epsilon = 3.8$, and $d = 0.3$ mm for which $\sigma_M = 26.87$ e.s.u. $= 8.96 \times 10^{-9}$ C/cm^2 are shown in Figures 77 through 79. We have considered three profiles with the parameter $\alpha d = 0.1$, 1, and 10, corresponding to a discharge front length $l = \alpha^{-1}$ of 3, 0.3, and 0.03 mm, respectively.

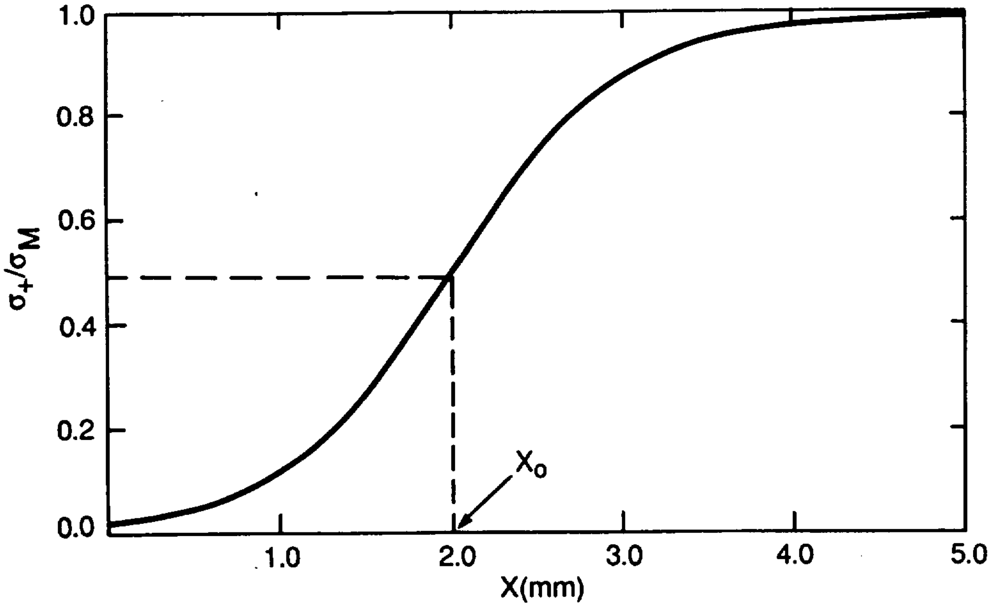

B-6199

Figure 76. - Charge density profile given by Eq. (5.4).

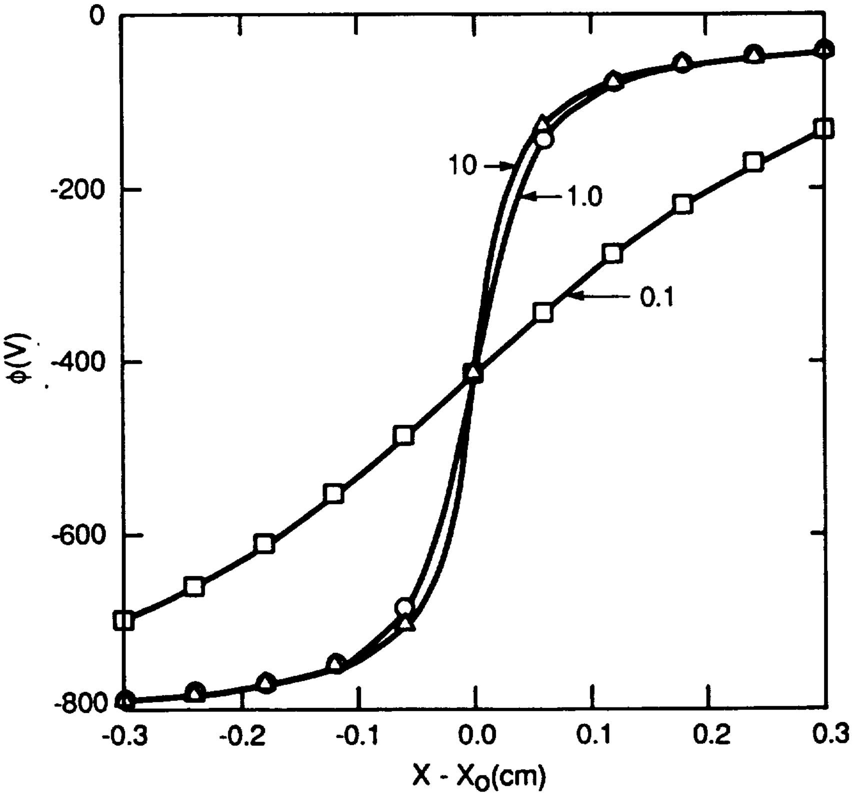

B-6200

Figure 77. - Potential along cover plate.

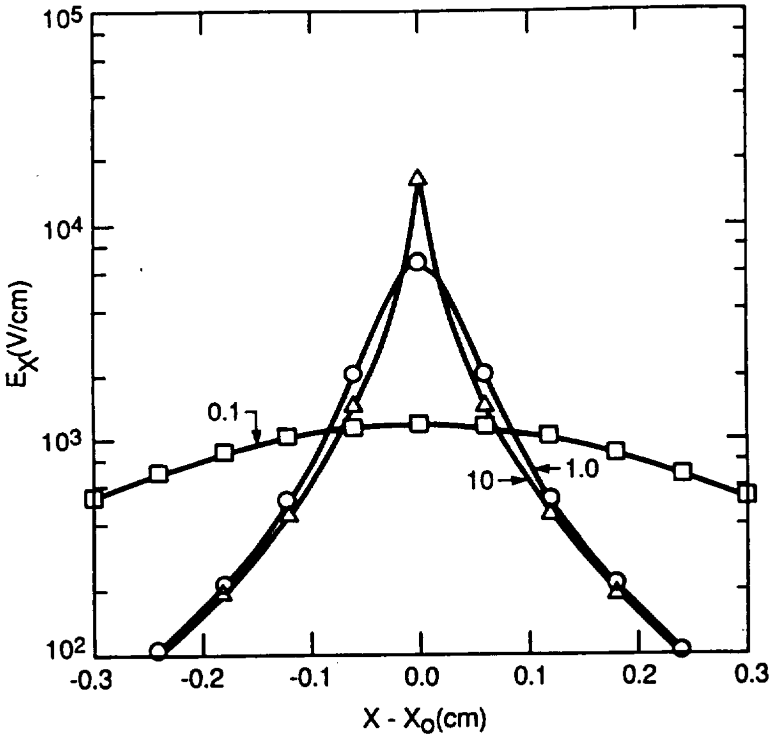

Figure 78. - Electric field in x direction.

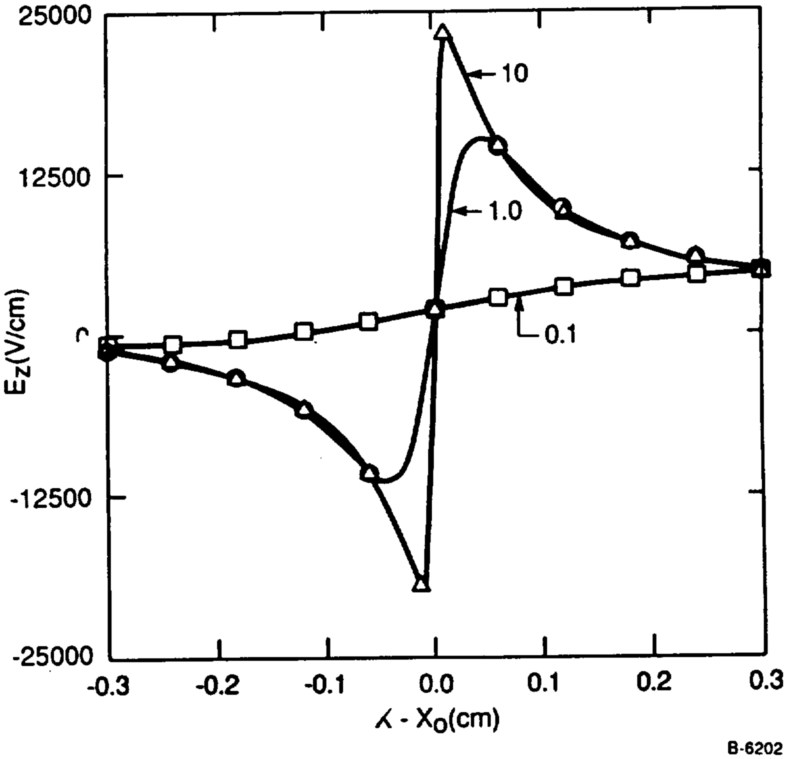

Figure 79. - Normal component of electric field along the surface.

Figure 77 shows how the potential varies along the surface. The potential is seen to rise from -800V, well downstream of the discharge to 0V way upstream. The presence of the plasma above the cover plate, which was not considered in our calculations, should not effect the results significantly if the net charge density over a distance d away from the surface is much less than σ_+. The discharge current, if carried by one charged species, could affect the results, however, if the (2D) charge density (when projected on the surface) is comparable to σ_M. Figure 78 shows the component of E field in the x direction. It is directed toward negative x and peaks at $x = x_0$. As shown in Ref.[36], when $\alpha d < 1$, we have, with good approximation,

$$E_x = \frac{-8\pi d}{\epsilon}\frac{d\sigma_+}{dx} = \frac{-\alpha V}{\cosh^2(\alpha x)} \quad . \tag{5-7}$$

The normal component of electric field is plotted in Figure 79 and is seen to change sign at $x = x_0$, with E_z pointing into the surface downstream of the discharge. $|E_z|$ asymptotes to zero when $(x-x_0)$ becomes large. In Figure 80 we plot E_z versus E_x. This figure is of interest for finding the region in the discharge where the secondary electron yield of the surface exceeds unity. This occurs in a region of space where E_z is positive and $|E_x/E_z| > 5$. This condition is satisfied in the hashed zone shown in Figure 80, corresponding to a very small region in physical space where $x \gtrsim x_0$.

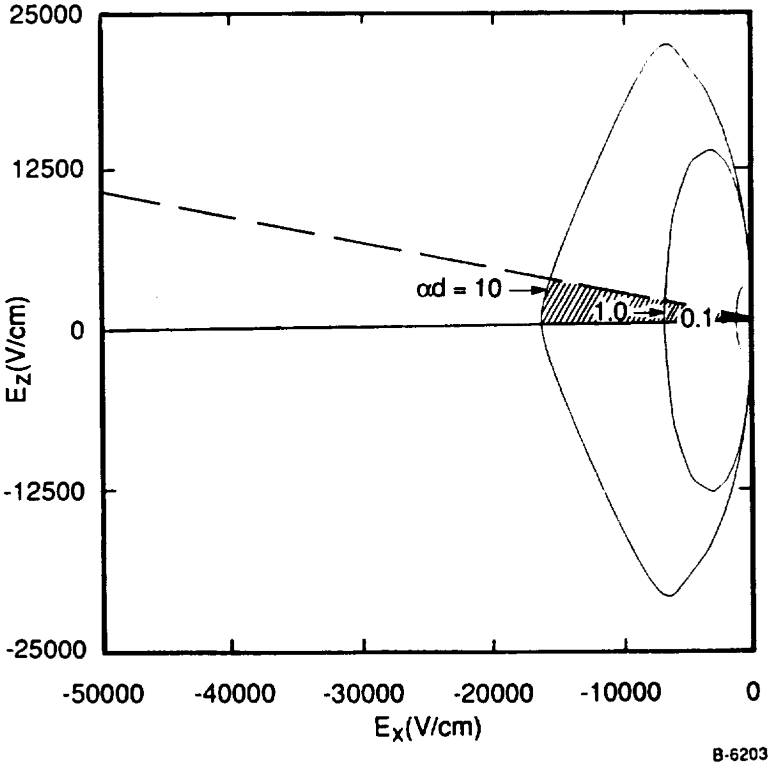

Figure 80. - E_z versus E_x.

It is clear from Figures 77 and 79 that the model of a neutralization front traveling along the surface, with secondary electron emission and electron impact ionization of desorbed gas playing a major role in maintaining the front, is not adequate. First of all, as is clear from Figure 79, the surface behind the front attracts ions. The ions generated in the front and accelerated toward the interconnect will fall back onto the surface of the insulator before they reach the interconnect. Secondly, there is a large potential drop along the surface, leading us to believe that the potential drop in the vicinity of the triple junction would not be large enough to sustain the discharge. For if ions generated during the discharge fall back onto the cover plate then the only means for continuing the discharge is for electrons to be continuously generated near the triple junction. It seems more plausible that the discharge of the cover plate is occurring more uniformly with the source of the discharge current occurring at hot spots near the triple junction around which most of the potential drop is occurring. We examine the necessary requirements for maintenance of the discharge in the next section.

5.3 Study of Arc Maintenance Requirements

If we discount ionization build-up on the surface of the dielectric, then all the ionization allowing current to flow from the interconnect, will occur in specific locations on the interconnect, called cathode hot spots. The arcing will behave as a vacuum arc which has been extensively studied in recent years.[36] An understanding of these arcs can be gleaned from analyses of low pressure discharges[37] where it is found that most of the voltage drop occurs in the dark zone adjacent to the cathode. Electrons are accelerated through the dark zone until they can generate, by impact ionization of the gas, a sufficient number of electron-ion pairs to sustain the discharge current. It is found that low pressure discharges cannot be maintained if the applied voltage is less than the cathode fall voltage. This voltage drop is of the order of 100 to 150V for argon and 200 to 300V for air depending on the cathode material. A table of cathode fall voltages, taken from Cobine[38] is shown in Table 2.

The extension of these findings to the high vacuum arc is the following. As in the case of a low pressure discharge, energetic ions that have been accelerated through the cathode fall region near a hot spot eject a certain number of electrons with an efficiency $\gamma_T = 0.1$. These electrons are accelerated away from the surface and impact ionize the metal vapor. Here the metal vapor plays the role of the gas in a low pressure discharge. Hot spots are localized regions of the cathode where the ion current is constricted and where heating of the surface to vaporization occurs. Several conditions must be satisfied for an arc to be maintained.

1. The voltage drop must exceed the cathode fall voltage for the vapor composed of cathode atoms.

2. The power incident on the cathode spot must be sufficient to maintain a vapor that is dense enough for significant electron impact ionization to occur.

TABLE 2. - NORMAL CATHODE FALL* (V)

Cathode	Air	A	He	H_2	Hg	Ne	N_2	O_2	CO	CO_2	Cl
Al	229	100	140	170	245	120	180	311			
Ag	280	130	162	216	318	150	233				
Au	285	130	165	247	...	158	233				
Ba	...	93	86	...	...	...	157				
Bi	272	136	137	240	...	...	210				
C	...	...	...	240	475	...	...	...	525		
Ca	...	93	86	...	...	86	157				
Cd	266	119	167	200	...	160	213				
Co	380										
Cu	370	130	177	214	447	220	208	...	484	460	
Fe	269	165	150	250	298	150	215	290			
Hg	...	...	142	...	340	...	226				
Ir	380										
K	180	64	59	94	...	68	170	...	484	460	
Mo	...	...	...	...	353	115					
Mg	224	119	125	153	...	94	188	310			
Na	200	...	80	185	...	75	178				
Ni	226	131	158	211	275	140	197				
Pb	207	124	177	223	...	172	210				
Pd	421										
Pt	277	131	165	276	340	152	216	364	490	475	275
Sb	269	136	...	252	...	...	225				
Sn	266	124	...	226	...	...	216				
Sr	...	93	86	...	...	...	157				
Th	...	...	...	...	...	125					
W	...	...	...	...	305	125					
Zn	277	119	143	184	...	...	216	354	480	410	
CsO-Cs	...	...	...	...	...	37					

*A.V. Engel and M. Steenbeck, "Elektrische Gasentladungen, ihre Physik u. Technik," Vol. 2, p. 103. J.J. Thomson and G.P. Thomson, "Conduction of Electricity through Gases," Vol. 2, pp. 331-332.

The cathode hot spots will occur, most likely, at those locations where, initially, a whisker (or a thin dielectric layer) generated the initial electrons through field emission (or dielectric breakdown). We have already modeled the emission from whiskers and determined the critical parameters (electric field strength, whisker height-to-width ratio) for a whisker to melt, vaporize and then trigger the discharge through breakdown of the whisker vapor. We also showed that a single whisker could not generate a sufficient current and total charge to neutralize the charge on a cover plate. We believe that, after initiation, the discharge will proceed due to the energy input onto the cathode surface by the ions generated in the vapor.

The geometry of the cathode hot spot is shown in Figure 81. The hot spot, of diameter 2a, is vaporizing at a temperature T_S. Secondary electrons (generated by ion impact) leave the surface and are accelerated through the dark zone over a distance r_c until they have gained enough energy to ionize the gas. The ions formed above the dark zone fall to the surface. Charge separation of ions and electrons is the cause of the potential drop in the dark zone. A more detailed analysis of the problem is given below.

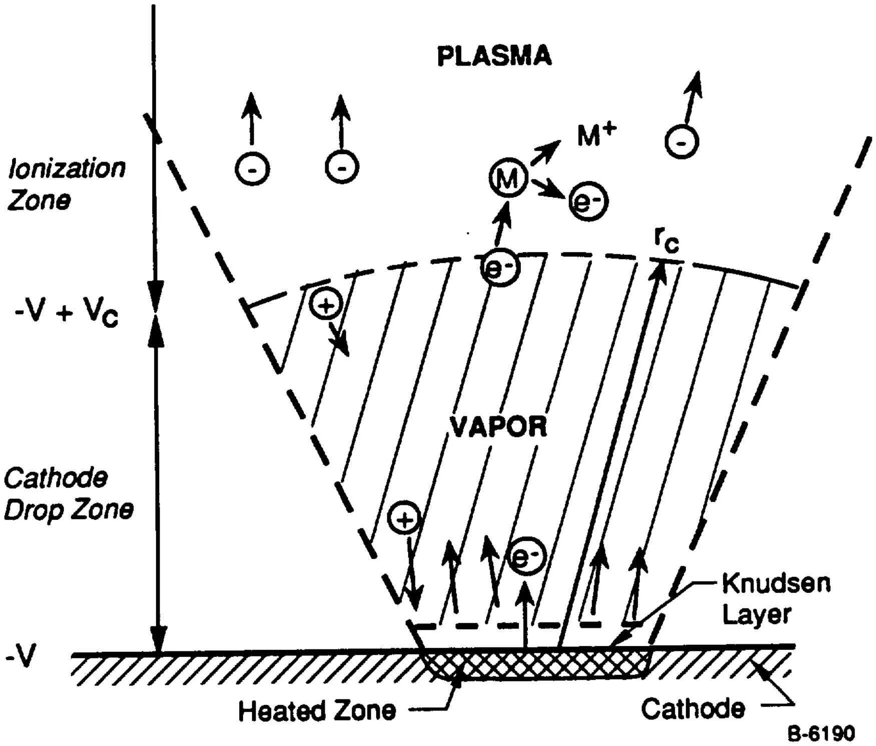

Figure 81. - Cathode arc voltage drop across dark zone V_C.

The vapor, which upon leaving the surface has a half Maxwellian distribution, expands through a Knudsen[39] layer of thickness typically three mean free paths and then expands into vacuum as a supersonic free jet. The threshold condition for maintaining the discharge is that the rate of ions lost to the cathode is equal to the rate of electrons generated by secondary electron emission (γ_T = secondary electron emission efficiency), and by the photoelectric effect (since the vapor is expected to radiate in the UV).

$$(\gamma_{ph} + \gamma_T)\left[1 + \beta \int_{\rho}^{\infty} n\sigma_i dt\right] \geq 1 \tag{5-8}$$

where $n(r)$ = number density of neutrals, σ_i = ionization cross section of neutrals, γ_{ph} is the photoelectric yield per ion hitting the surface, and $\beta(>1)$ is a factor that takes into account that electrons do not travel in straight lines - they make many elastic collisions with neutrals before they ionize the gas. Application of random walk theory would lead to an estimate for β

$$\beta \approx \left[\frac{\sigma_m}{\sigma_i}\right]^{1/2} \simeq 3 \text{ to } 10 \ . \tag{5-9}$$

where σ_m = momentum transfer cross section.

Equation (5.8) is essentially a condition on the density and extent of vapor above the cathode spot required for maintenance of the discharge. The density of vapor is, in turn, determined by the energy input to the surface by ions.

If the ion current density is j_+ and the energy with which the ions hit the surface is ϵ then the power on the surface is $P = (j_+/e)\pi a^2\epsilon$. This power input is balanced by vaporization and heat conduction from the surface to the bulk of the cathode. In steady state we have

$$\left[\frac{j_+}{e}\right]\epsilon\pi a^2 = \dot{m}\Delta H\pi a^2 + \dot{Q}_c \tag{5-10}$$

where $\dot{m}$ is the mass per unit area vaporized, $\Delta H \left[= \int^{T_s} C_p dT + H_v\right]$ is the energy per unit mass required to heat the cathode to the vaporization temperature T_s and then to vaporize it (heat of vaporization = H_v), and $\dot{Q}_c$ is the heat conduction losses to the bulk of

C-2.

the cathode. For short enough discharges and large cathode spots the thermal diffusion length ℓ_d will be smaller than a and $\dot{Q}_c$ scales as a^2. The spot radius can then be factored from Eq. (5.10), which will then yield a critical current density j_+. The spot size will then be related to the total current in the arc (since $I_+ = I_-$ in steady state) and a will scale as the square root of the current, $a \propto I^{1/2}$. Typical discharge times, τ, are experimentally found to be of the order of 1 μs. The thermal diffusivity for Kovar is $k_D \simeq 0.1$ cm^2/s. Thus, cathode spots of size $a > \sqrt{k_D \tau} = 3\ \mu$m will be in the one-dimensional regime for heat conduction.

5.4 Model and Analytic Experiment for Arc Rate

The previous PIC calculations pointed towards the role of secondary electron emission from the side of the cover glass in the arc initiations process. The theory developed for describing this process utilizes fields calculated for the region around the triple junction using the PIC code. A statistical model of field build-up at arc sites is presented below which predicts much of the behavior previously observed in our laboratory data. We consider the model system as shown in Figure 82. If the surface charge density on the side surface of the coverglass and adhesive is σ then once the coverglass and adhesive are charged by the plasma

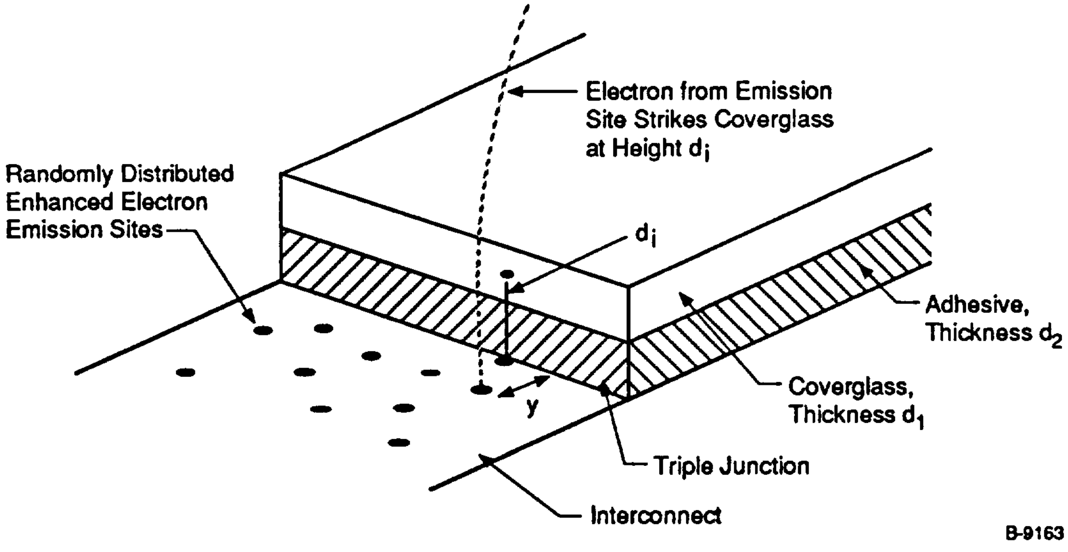

Figure 82. Model system.

$$I_e=S_{real}\left[\frac{S_{eff}}{S_{real}}\right] jec= S_{real}\left[\frac{S_{eff}}{S_{real}}\right] A(\beta E)^2 e^{-\frac{B}{\beta E}} \quad . \tag{5-11}$$

ions, the charge density changes due to electrons striking the surface. The electrons are taken to be emitted from enhanced field emission sites on the interconnector with a current

In (5.11), E is the average electric field at the emitting site while β is the field enhancement factor. The emission site is assumed to have an area S_{real}. The area S_{eff} is the effective emitting area of the site of actual area S_{real}. The field enhancement factor can be related to the microscopic characteristics of the surface. For example, a metallic whisker of height h and radius r will enhance the average field by $\beta=h/2r$. Experimental work has shown that typically for $1 \leq \beta \lesssim 100$, the physical reason for an enhancement is a metallic whisker. For $100 \lesssim \beta \lesssim 10002000$, microscopic dielectric inclusions enhance the average field. The constants A and B are physical constants related to the surface work function ϕ_w by

$$A=\frac{1.5 \times 10^{-6}\ 10^{4.52/\sqrt{\phi_w}}}{\phi_w} \quad A/V^2$$

$$B=6.53 \times 10^9\ \phi_w^{3/2} \quad V/m$$

with ϕ_w in eV. Experiments have shown that on dielectric inclusions, only in part of the inclusion may emit electrons. Hence, in general, $S_{eff} \lesssim S_{real}$. However, once the electrons leave the emission site, they spread out due to thermal effects so that they seem to coming from the area S_{real}.

If the electron emitted from a side strike an area of the side surface of $\sqrt{S_{real}}d_i$ then we can write

$$\frac{d\sigma}{dt} = (\gamma_{ee}-1)\ j_{ec}\ (\beta E)\ \frac{\sqrt{S_{real}}}{d_i} \tag{5-12}$$

In (5.12), γ_{ee} is the secondary electron yield of the side surface. In general, this is a function of the energy and angle of the impacting electron. We introduce the capacitance per unit area of the side surface, C_d and write for the electric field at the triple junction. The amplification factor ξ takes account of the fact that the electric field has to jump across the coverglass/adhesive interface. Hence, we have

$$E_{TJ} = \frac{\xi\sigma}{C_d d_i} \tag{5-13}$$

$$\epsilon = 1 \qquad\qquad d_i \leq d_2$$

$$\epsilon = \frac{1}{\frac{d_2}{d_i} + \frac{\epsilon_{d_2}}{\epsilon_{d_1}} \left[\frac{d_i - d_2}{d_i} \right]} \qquad d_i > d_2 \ .$$

The relation between the electric field at the emission site and the triple junction will, in general, be complex. In the model two dimensional system the electric field depends only on the distance, y, from the triple junction. Hence we write

$$E = \eta(y) E_{TJ} = \frac{\eta(y)\xi\sigma}{C_d d_i} \ . \tag{5-14}$$

The use of (5.11), (5.13), and (5.14) in (5.12) gives the rate of change of the electric field at the emitting site as

$$\frac{dE}{dt} = \eta(y)\xi\left(\gamma_{ee} - 1\right)\frac{\sqrt{S_{real}}}{C_d d_i(y)} A \left[\frac{S_{eff}}{S_{real}} \right] (\beta E)^2 e^{\frac{B}{\beta E}} \ . \tag{5-15}$$

If the secondary electron yield, γ_{ee}, it taken as a constant, then (5.15) can be solved exactly to give

$$\frac{E(t)}{E(t=0)} = \left[1 + \frac{\beta E(t=0)}{B} \ell n \left[1 - \exp\left[-\frac{B}{\beta E(t=0)} \right] \frac{B}{\beta} \alpha t \right] \right]^{-1} \tag{5-16}$$

where α is the constant in front of $(\beta E)^2$ in (5.15). This expression for the electric field diverges at a time τ_{EFEE} given by

$$\tau_{EFEE} \approx \frac{C_d d_i^2(y)}{(\gamma_{ee}-1)\sqrt{S_{real}}\ \eta(y)\ \xi\ A \left[\dfrac{S_{eff}}{S_{real} B\beta}\right]} \exp\left[\frac{B}{\beta E(t=0)}\right] \ . \qquad (5\text{-}17)$$

From a physical viewpoint, Eq. (5.15) contains the information that the emission site gives electrons to the side of the coverglass. If the side of the coverglass emits more secondary electrons than incoming primaries, the surface charges positively. This effect enhances the field at the emitter and therefore, a positive feedback loop exists. With the inclusion of more physics, however, it is clear that the electric field and associated emission current cannot become infinite. When the current becomes sufficiently large it will become space charge limited. Even before this happens, the atomic dissipation may destroy the emission site or, if there is gas or vapor in the current path it may be ionized. These occurrences would be seen as a discharge. Since the increase of the electric field is clearly a necessary condition for a discharge event to occur, Eq. (5.15) can be used to provide a lower bound on the time between arcs when the electric field buildup time is expected to be the slowest time in the arc process.

We can write (5.17) in a functional form that depends on the interconnector voltage, V. We have

$$T_{EFEE}(y,S_{real},S_{eff},\beta,V) = \frac{C_d d_i^2(y)}{(\gamma_{ee}-1)\sqrt{S_{real}}} \ \frac{1}{\eta\ \xi\ A \left[\dfrac{S_{eff}}{S_{real}}\right]} \ \frac{1}{B\beta} \exp\left[\frac{Bd}{\beta\eta\xi_o V}\right] \qquad (5\text{-}18)$$

where $d = d_1 + d_2$ and $\xi_o = \left[\dfrac{d_2}{d_1+d_2} + \dfrac{\epsilon_{d_2}}{\epsilon_{d_1}}\left[\dfrac{d_1}{d_1\ d_2}\right]\right]^{-1}$.

For the secondary electron yield, we use the well known expression

$$\gamma_{ee} = \gamma_{max}\left[\frac{E_i}{E_{max}}\right] \exp\left[2-2\sqrt{\frac{E_i}{E_{max}}}\right] \exp\big(2(1-\cos\theta_i)\big) \qquad (5\text{-}19)$$

where $E_i = \left[\dfrac{\xi_o}{\xi}\right]\left[\dfrac{d_i}{d}\right] V$ and $\theta_i = \tan^{-1}\left[\dfrac{d_i}{y}\right]$.

The impact distance d_i, field reduction factor η and side surface capacitance are functions only of y and were determined by particle in cell simulations. The results are

$$\frac{d_1}{d_1+d_2} = \sum_{n=1}^{6} a_n \left[\frac{d_y}{d_1+d_2}\right]^{n-1}$$

where $a_1=6.9$, $a_2=-21$, $a_3=31$ and $a_4=-14.6$,

$$\eta = 1 + \sum_{n=1}^{4} b_n \left[\left(\frac{y}{L}\right)^{2n} -1\right]$$

where $b_1=0.26$, $b_2=8.07\mathrm{x}10^{-2}$, $b_3=-0.12$, $b_4=0.54$ and 2L is the distance to the next triple junction (or length of the conductor),

$$\frac{\bar{C}_d}{C_d} = \sum_{n=1}^{6} C_n \left[\frac{d_1}{d_1+d_2}\right]^{n-1}$$

where $\bar{C}_d$ is a normalization constant = 3.80×10^6 F/m^2 and $C_1=4.38\mathrm{x}10^{-3}$, $C_2=0.65$, $C_3=-3.8$, $C_4=10.86$, $C_5=13.12$, and $C_6=5.73$.

Finally the minimum time between two arcs would be given as

$$\tau_{\mathrm{arc}} = \tau_{\mathrm{ion}} + \tau_{\mathrm{EFEE}} \tag{5-20}$$

where τ_{ion} is the time for ions to recharge the coverglass and adhesive after an arc. Hence, $\tau_{\mathrm{ion}}=\Delta Q/en_iV_{\mathrm{ion}}\,A_{\mathrm{cell}}$ where ΔQ is the charge lost in the last discharge, n_i is the plasma density, V_{ion} is the mean speed of the ions entering the sheath over the coverglass and A_{cell} is the cell surface area.

5.4.1 Procedure for Choosing the Parameters and Calculating the Arc Rate. - In the previous section we have derived an expression for time between arcs for each emission site. This expression can be modified in several ways to more realistically model the experimental situation. First, the recharging of the coverglass/adhesive after an arc and the build up of the electric field at an emission site will happen simultaneously rather than sequentially. If we define V_e as the voltage at which the enhanced field electron emission starts to become significant and V_a as the voltage at which the previous arc occurred which lost charge ΔQ then the coverglass will have dropped to V_a-$\Delta Q/C_f$ where C_f is the capacitance of the front surface. It will have to recover to V_e for enhanced field electron emission to lead to an arc. Therefore, we can unite

$$\tau_{arc} = \min\left\{\frac{(V_eC_f-(V_aC_f-\Delta Q))}{en_iV_{ion}A_{cell}} + \tau_{EFEE}(\beta V_e)\right\} \tag{5-21}$$

where the minimization is over all V_e such that $V_a-\frac{\Delta Q}{c_f}<V_e\leq V$. Furthermore, once a discharge occurs, the associated plasma cloud will discharge all the emission sites within some area around the discharging site. To model this, we define

$$\tau_a + \min\{\tau_{arc}\} \tag{5-22}$$

where the minimization is over all sites within some correlation area, A_{corr}.

The time τ_a depends on many physical parameters. Some of the parameters can be measured with certainty, for example, the thickness of the coverglass. Others, however, are either not known well or have not typically been measured. In order to model this we choose these parameters randomly from an assumed set of probability distribution functions. The parameters that we choose in this fashion are the charge lost in a discharge ΔQ, the plasma density N_i, the location of the emission site y, the actual area of the site S_{real}, the effective area of the site S_{eff} and the associated enhancement factor .

Finally, to obtain the arc rate we chose an experiment time, τ_{ex}. Next, we calculate the arc interval, τ_{a_1}, from (5.22) for the first arc using the procedure of choosing randomly the parameters above. After we have τ_{a_1} we determine τ_{a_2} by the same procedure and repeat this process until at the N+1th arc we have

$$\tau_{a_1} + \tau_{a_2} + \tau_{a_3} + \dots \tau_{a_{N+1}} > \tau_{ex}$$

we then set the arc rate to be $R=N/\tau_{ex}$. After the arc rate is determined in this manner, the entire procedure is repeated until a statistically significant sample of values of R is accumulated. The average arc rate $\overline{R}$ for each voltage is then calculated from the set of values of R.

5.4.2 Results for Various Experiments. - We compose the theory results with an experiment where, the arc rate vs voltage was measured for a configuration where a coverglass was glued to a kovar backing. To model this we chose the distance between the edge metal and the edge of the coverglass as 4 mm, the depth d_1=305μm, d_2=50μm with

$\epsilon_{d_1}/\epsilon_0=7.3$, $\epsilon_{d_2}/\epsilon_0=2.75$. The work function of the surface is $\phi_W=4.5$ eV. The secondary yield parameters of the glass were taken as those measured for borosilicate glass, i.e., $\gamma_{max}=2.4$, $E_{max}=400$eV. The ion mass in chamber was 40 amu with a coverglass of 1 cm x 1 cm. The experiment time was 11 min for most of the data points. The density of emission sites was chosen as 1.5×10^7 sites/m^2. This is a reasonable value as measured by experiments which have taken scanning electron micrographs of similar surfaces. If the sites are taken as uniformly distributed on the metal this gives 17 possible emission close enough to the 1 cm long triple junction to cause an arc. The real surface area of the emission sites was chosen randomly from a distribution such that $\log_{10} S_{real}$ was uniformly distributed from -13 to -9 (in m^2). At the largest sizes this corresponds to 30 μm size inclusion. This is consistent with the sizes of some of the adhesive nodular seen in previous quarterly reports. The effective surface areas were chosen randomly from a distribution such that $\log_{10} S_{eff}$ was uniformly distributed from -17 to -13 (in m^2). The charge loss, ΔQ, was chosen uniformly from a uniform distribution between 4.3×10^{-9}C and 2.8×10^{-8}C. At the highest charge loss and the highest voltage this corresponded to almost complete discharge of the coverglass. The plasma density was chosen from a uniform distribution between 4×10^{12}m^{-3} and 6×10^{12}m^{-3}. Finally, the field enhancement distribution was taken as

$$f(\beta) \propto e^{-\beta/\beta_0} \qquad 1 \leq \beta \leq 1000$$

with $\beta_0=170$.

The result is shown in Figure 83. The theory curve is shown to match the experimental data over most of the data range, only deviating at the highest voltages. For the entire range of voltages, the arc rate is dominated by the enhanced field electron emission. At low voltages, the rate decreases exponentially so that below 290V no arcing was found in repeated trials. The deviation at the highest voltages may be due to the finite time gas recycling on the side surface of the coverglass. The model contains the implicit assumption that no other process will reduce the arcing rate. At the highest frequencies it may be possible that the gas plume expansion and recharging of the surfaces reduces the rate at which arcs can happen.

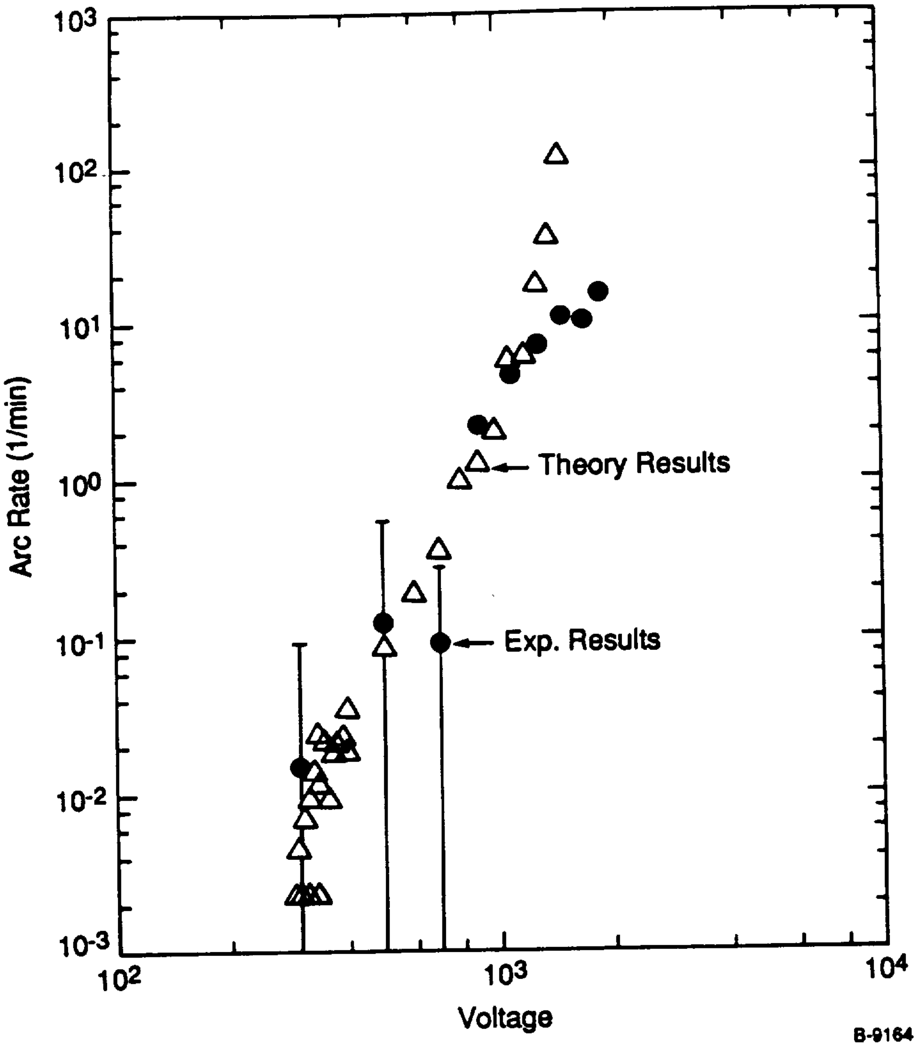

Figure 83. - Comparison of theory calculation with experimental measurements of model solar cell arcing rates.

6. CONCLUSIONS

Out examination of solar cell and anodized structural component arcing under negative bias in an LEO plasma have produced the following conclusions:

1. Primary mode of solar cell arcing observed is dielectric breakdown in cover glass adhesive.

2. Primary discharge mechanism is release of charge to the space plasma via ionization of desorbed species from the arcing site. Are durations are typically 1 to 5 μs in duration and produce UV light emission. The intensity of the light emission correlates linearly with arc current.

3. Interaction of H_2O vapor with adhesive enhances arcing rate - apparently by lowering dielectric strength.

4. Mechanism may be through reduction in effective film thickness due to absorption of water vapor at dielectric/plasma interface, where adhesive becomes partially conducting.

5. Plasma interactions with adhesive enhances surface conductivity - but penetration depth is probably small compared with film thickness.

6. Plume impact and water dumps on orbiting spacecraft may enhance local H_2O levels and maintain high arc rates well into mission duration.

7. Removal of adhesive film eliminates arcing but will enhance parasitic current collection along edge of solar cell.

8. Changing coverslip overhang to shield cell edge should reduce arcing and parasitic current collection.

9. Field enhancement o\at tips of whiskers are not responsible for arc initiation. Insufficient field strength exists for field ionization mechanism to operate.

10. Statistical theory incorporating secondary electron production on dielectric at triple junction shows promise in explaining arc rates observed on PIX II and in laboratory experiments. Predicted scaling of arc rate with plasma density is confirmed by laboratory measurements.

11. Arc thresholds for anodized aluminum plate are dependent on processing technique and film thickness. Thresholds of -450 to -650 V are observed for 0.2 mil sulfuric acid anodizations. Thresholds of approximately -150 V arc observed for 0.07 to 0.10 mil thick chromic acid processed samples.

12. Arc thresholds on anodized plate can be severely reduced by damage to the coating as a result of the production of triple junctions exposed to the plasma. Thresholds as low as -70 V are observed for cut edges and -140 V for simulated micrometeorite/debris impacts.

7. ACKNOWLEDGEMENTS

The authors would like to thank the following people for their roles in the conduct of this effort: Drs. Alan Gelb, Herbert Cohen and David Green for review of the technical effort; Dr. Karen Carleton for her early work on model solar cell design, construction, and mounting; Dr. Mark Horenstein of Boston University for his helpful discussions and guidance of Ed Aifer; and Dr. Mark Allen for his help in the use of the imaging CCD camera system. We would also like to thank Drs. Daniel Snyder, Dale Ferguson, and Barry Hillard for their support of the effort at NASA Lewis Research Center. In addition, we would like to acknowledge the assistance of Drs. David Handy and Don Guidice and Captain Paul Severance at the Geophysics Directorate of the Air Force, Phillips Laboratory and Dr. Raymond di Gaston of Vitro Corporation.

8. REFERENCES

1. Grier, N.T., "Experimental Results on Plasma Interactions with Large Surfaces at High Voltages," NASA TM-81423, January, 1980.

2. Grier, N.T., "Plasma Interaction Experiment II: Laboratory and Flight Results," Spacecraft Environment Interactions Technology Conference, Colorado, October 4-6, 1983, NASA CP-2359, p. 333-349.

3. Ferguson, D.C., "The Voltage Threshold for Arcing for Solar Cells in LEO - Flight and Ground Test Results," NASA TM-87259 (1986).

4. Miller, W.L., "An Investigation of Arc Discharging on Negatively Biased Dielectric-Conductor Samples in a Plasma," Spacecraft Environment Interactions Technology, NASA CP-2359, 367-377 (1983).

5. Thiemann, H. and Bogus, K., ESA Journal, 10, 43-57 (1986).

6. Snyder, D.B., "Discharges on a Negatively Biased Solar Array," NASA TM-83644, 1984.

7. Snyder, D.A., "Characteristic of Arc Currents on a Negatively Biased Solar Cell Array in a Plasma," NASA TM-83723, July 1984.

8. Thiemann, H., Schunk, R.W. and Bogus, K., "Where Do Negatively Biased Solar Arrays Arc?," Journal of Spacecraft and Rockets, Engineering Notes, Sept-Oct 1990.

9. Stevens, N.J., "Environmentally Induced Discharges on Satellites," NASA TM-82849, May, 1982

10. Fujii, H., Shibuya, Y., Abe, T., Ijichi, K., Kasaia, R., and Kuriki, K., "Laboratory Simulation of Plasma Interactions with High Voltage Solar Arrays," Proceedings of the 15th International Symposium on Space Technology and Science, Tokyo, 1986.

11. Kuninaka, H., "Qualitative Experiment with Arc Discharges on Negatively Biased Solar Cells," Journal of Spacecraft and Rockets, Vol. 27, No. 6, Nov-Dec 1990.

12. Thiemann, H., Bogus, K.P., "High-Voltage Solar Cell Modules in Simulated Low-Earth-Oribt Plasma," Journal of Spacecraft and Rockets, Vol. 25, No. 4, 1988.

13. Kennerud, K.L., "High Voltage Solar Array Experiment," NASA Report CR-121280, 1974.

14. Parks, D.E., Jongeward, G., Katz, I., and Davis, V.A., J. of Spacecraft and Rockets, 24, 367-371 (1987)

15. Hastings, D., Weyl, G., and Kaufmann, D., AIAA J. of Spacecrafts and Rockets, 27, 539-544 (1990).

16. Weyl, G., Hastings, D., Kaufmann, D., and Green, B.D., "Arcing in Negatively Biased Structures in Low Earth Orbit," PSI-2057/TR-889, Physical Sciences Inc., December 1988; NASA NAS3-25402.

17. Vaughn, J.A. and Carruth, M.R., "Current Flow in a Plasma Caused by Dielectric Breakdown," presented at Fifth Space Operations, Applications,and Research Conference, July 1991, Houston, TX.

18. Grier, N., "Kapton Pyrolization from Collected Electron Currents," presented at Fifth Space Operations, Applications, and Research Conference, July 1991, Houston, TX.

19. diGaston, R., Vitro Corporation, private communication, October 1991.

20. Snyder, D., NASA Lewis Research Center, private communication, October 1991.

21. Same as Ref. 19.

22. Arcing in Space Structure in Low Earth Orbit, Quarterly Report 2, PSI-TR-1046, August 1990.

23. diGaston, Vitro Corporation, private communication, October 1991.

24. Material Data Safety Sheet, DC93-500 adhesive, Dow Corning Corp, Midland, MI.

25. Handbook of Auger Electron Spectroscopy, 2nd Edition, published by the Physical Electronics Division of Perkin Elmer Corp., 1976.

26. Compton, K.G. and Mendizzce, A., Am. Soc. Testing Materials, Proc. 40, 978 (1940).

27. Caledonia, G.E., Krech, R.H., and Green, B.D., "A High Flux Source of Energetic Oxygen Atoms for Material Degradation Studies," AIAA J. 25, 59-63 (1987).

28. Grier, N. and Snyder, D., NASA Lewis Research Center, private communication, October 1991.

29. Hersktrowitz, N., "Plasma Diagnostics Vol 2, Surface Analysis and Interactions," Ed. by O. Auciello, and D.L. Flamm (Academic Press Inc., CA 1989).

30. Snyder, D.B., "Characteristics of Arc Currents on a Negatively Biased Solar Cell Array in a Plasma," Nuclear and Space Radiation effects Conference, Colorado Springs, CO, July 1984; also NASA TM-83728.

31. Miller, W., "An Investigation of Arc Discharging on Negative Biased Dielectric-Conductor Samples in a Plasma," NASA CP-2336 (1984).

32. Handbook of Mathematical Functions [M. Abramowitz and I. Stegun eds], National Bureau of Standards Applied Mathematical Series #55, U.S. Government Printing Office, Washington, D.C. 20402 (1964), p 229.

33. Arcing in Space Structures in Low Earth Orbit, Quarterly Report 3, PSI-2123, December 1990.

34. Cobine, J.D., Gaseous Electronics (Dover, New York, 1958), p. 136.

35. Hachenberg, O., Electronics and Electron Physics, Vol. 2.

36. Mesyats, G. and Proskurovsky, D., Pulsed Electric Discharges into Vacuum (Springer-Verlag, 1989).

37. Cobine, J.D., Gaseous Conductors (Dover, New York, 1958), pp. 212-226.

38. Same as Ref. 37, p. 217.

39. Anisimov, S., "Vaporization of Metal Absorbing Laser Radiation," Soviet Phys. JEJP, 27, 182-183 (1968).

APPENDIX A

Analytical evaluation of the electric field in the vicinity of the triple junction.

We extend in this section the calculations that were presented in quarterly report 3 (in which we calculated the electric field above the dielectric) to the evaluation of the fields in the vicinity of the triple junction. The geometry is shown in Figure 1. A dielectric of thickness d is placed above an infinite plane conductor that has potential $\phi_c = -V$. The conductor is in the xy plane and has coordinate $z = -d$. The dielectric has infinite extent in the y direction and covers the half plane $x > 0$. The top surface of the dielectric is located at $z = 0$ and has a charge density σ (x). We calculated the potential inside the dielectric when σ (x) was taken to be independent of x, i.e. $\sigma (x) = \sigma_0$. We found

$$\phi(x) = \frac{\sigma_0}{\epsilon} \int_{-x}^{\infty} dx' \, \ell n \left[\frac{(x-x')^2 + (z + 2d)^2}{(x-x')^2 + z^2} \right] - V \tag{A-1a}$$

$$= \frac{2d\sigma_0}{\epsilon} \int_{-\nu_0}^{\infty} d\upsilon \, \ell n \left[\frac{\upsilon^2 + (1 + z/2d)^2}{\upsilon^2 + (z/2d)^2} \right] - V \tag{A-1b}$$

where ϵ is the dielectric constant and, in the last step, we defined $\nu_0 = x/2d$. The charge density σ_0, for a uniformly charged capacitor sustaining a voltage V is

$$\sigma_0 = \frac{\epsilon V}{4\pi d} \tag{A-2}$$

Though Eq (A-1b) gives a good approximation to the field far from the edge of the dielectric ($\upsilon_0 >> 1$), it needs to be modified somewhat if we wish to calculate the field near the edge ($\upsilon_0 << 1$). At the top edge of the dielectric, we calculate the potential by setting $z = 0$ and $\upsilon_0 = 0$ in Eq (A-1b). We find

$$\phi(0,0) = \frac{V}{2\pi}\int_0^\infty \ell n\left[1+\frac{1}{\upsilon^2}\right]\alpha\upsilon \ -V$$

$$= \frac{V}{2\pi}\left[V\ \ell n\left[1+\frac{1}{\upsilon^2}\right]\Bigg|_0^\infty + 2\int_0^\infty \frac{d\upsilon}{(\upsilon^2+1)}\right] -V \qquad \text{(A-3)}$$

$$= -\frac{V}{2}$$

Now, in the presence of a space plasma the dielectric surface will charge up so that its potential is near zero everywhere. We must therefore add to σ_0 an extra positive charge density $\delta\sigma(x)$, which goes to zero as $x \to \infty$. It is clear from Eq (A-3) that $\delta\sigma$ will vary as $[1+(x/2d)^2]^{-\alpha}$. For purposes of calculations we set $\alpha = 1$ and therefore set:

$$\delta\sigma = \frac{A}{1+(x/2d)^2} \qquad \text{(A-4)}$$

We evaluate A in such a way that $\phi\ (0,0) = 0$. We must have:

$$\frac{2d\ A\sigma_0}{\epsilon}\int_0^\infty d\upsilon\ \frac{1}{1+\upsilon^2}\ \ell n\left[\frac{\upsilon^2+1}{\upsilon^2}\right] = \frac{V}{2} = \frac{2\pi d\sigma_0}{\epsilon} \qquad \text{(A-5)}$$

We change variable by defining

$$t^2 = \frac{\upsilon^2}{\upsilon^2+1}$$

We obtain[1]

$$\int_0^\infty \frac{d\upsilon}{1+\upsilon^2}\ \ell n\left[\frac{\upsilon^2+1}{\upsilon^2}\right] = \sim 2\int_0^1 \frac{\ell n\ t}{\sqrt{1-t^2}} = \pi\ell n2 \qquad \text{(A-6)}$$

Therefore $A = (\ell n2)^{-1}$

We will use in the evaluation of the field near the triple junction, the surface charge density

$$\sigma = \sigma_0 \left[1 + \frac{1}{\ell n \, 2 \left[1 + (x/2d)^2 \right]} \right] \tag{A-7}$$

The electric potential in space, outside of the dielectric is obtained by evaluating the integral

$$\phi\,(\vec{r}) = \int \frac{e(r')}{|\vec{r} - \vec{r'}|}\, d\vec{r'} + \phi_0 \tag{A-8}$$

Where $\rho(\vec{r})$ is a charge distribution due to

a) Free charges on the surface of the dielectric
b) Bound charges ρ_p due to the change in the polarization vector
c) Image charges due to the presence of the infinite conductor at $z = -d$

We have:

$$\rho_p = -\nabla'(\vec{P}) \tag{A-9}$$

where

$$\vec{P} = \chi\, \vec{E} = \frac{\epsilon - 1}{4\pi}\, \vec{E} \tag{A-10}$$

It is easy to show that the sum of contributions (a) and (b) from the top surface of the dielectric is equivalent to considering an effective surface charge density σ_0/ϵ, where $\sigma_0\,(r')$ is the actual surface charge density. The proof is as follows.

We have

$$\nabla'_{.}\vec{D} = \nabla.(\epsilon\vec{E}) = 4\pi\rho$$

$$-\nabla'\vec{P} = -\nabla'_{.}\left[\frac{\epsilon-1}{4\pi}\vec{E}\right] = \rho_p$$

Thus

$$\int \frac{(\rho+\rho_p)}{|\vec{r}-\vec{r}\,'|}\, d\vec{r}\,' = \frac{1}{4\pi}\int \nabla'_{.}\left[\vec{D}-\vec{D}+\frac{\vec{D}}{\epsilon}\right] d\vec{r}\,'$$

$$= \frac{1}{4\pi}\int_{Surface}\left[\frac{\vec{D}_2}{\epsilon_2}-\frac{\vec{D}_1}{\epsilon_1}\right]\cdot\hat{\eta}\, dA'$$

On the vacuum side of the surface we have $\vec{E}_2 = \vec{D}_2 = 0$. Across the dielectric we have

$\vec{D}_2 - \vec{D}_1 = -\vec{D}_1 = 4\pi\sigma\,\hat{n}$.

Thus

$$\frac{1}{4\pi}\int \frac{(\rho+\rho_p)}{|r-r'|}\, d\vec{r}\,' = \int_{\text{top surface}} \frac{\sigma}{\epsilon|\vec{r}-\vec{r}\,'|}\, d\vec{r}\,'$$

If we now take into account the image charges, we obtain Eq (A-1a) for the contribution by the top surface of the dielectric to the potential in the vicinity of the triple junction; with $\phi_0 = -V$.

As a first approximation we will neglect the change in polarization inside the dielectric (we assume uniform $\vec{E}$ inside the dielectric) except at the boundary glass-adhesive.

We assume the adhesive to be much thinner than the glass cover plate so that we can evaluate the field at the boundary as being the same as the field at the surface of the conductor (z = -d).

Setting z = -d in Eq (A-1a) we obtain

$$\vec{E}\,(x).\hat{\eta} = \lim_{z\to 0}\left[-\frac{\partial}{\partial z}\,\frac{2d}{\epsilon}\int_{-\upsilon_0}^{\infty}\sigma(\upsilon)\ell n\left[\frac{\upsilon^2+[1+(z/2d)]^2}{\upsilon^2+(z/2d)^2}\right]\right]d\upsilon \qquad \text{(A-11)}$$

Thus the contribution from the change in the polarization at the boundary glass-adhesive is:

$$\delta\phi = -\int\frac{\nabla'\cdot P}{|\vec{r}-\vec{r}\,'|} + \textit{Image contribution}$$

$$= -\int\frac{\left[\vec{P}_{glass}-\vec{P}_{adh}\right]}{|\vec{r}-\vec{r}\,'|}\,.\,\hat{\eta}\;dA + \textit{image contribution} \qquad \text{(A-12)}$$

$$\delta\phi = -\int_{s'}\frac{\vec{E}\cdot\hat{\eta}}{4\pi|\vec{r}-r'|}\left(\frac{\epsilon}{\epsilon_a}-1\right)dA + \textit{Image contribution}$$

Where $\vec{E}$ is given by Eq (A-11). Performing the derivative in Eq (A-11) with respect to z and letting z→-d in the result, we find

$$\vec{E}\,.\hat{\eta} = -\frac{2}{\epsilon}\int_{-\upsilon_0}^{\infty}\frac{\sigma(\nu)}{\nu^2+1/4}\,d\,\nu$$

Thus

$$\delta\phi = \frac{1}{2\pi}\left(\frac{1}{\epsilon}-\frac{1}{\epsilon_a}\right)\int_{S'}\frac{dA}{|\vec{r}-\vec{r}'|}\int_{-\nu_o(r')}^{\infty}\frac{\sigma(\nu)}{(\nu^2+1/4)}\,d\nu + \textit{Image contribution} \qquad \text{(A-13)}$$

We evaluate the integral over ν.

$$T(\nu_o) = \int_{-\nu_o}^{\infty}\left[1+\frac{1}{\ell n2(1+\nu^2)}\right]\left[\frac{1}{\nu^2+1/4}\right]d\nu \qquad \text{(A-14)}$$

We have

$$\frac{1}{(\nu^2+1)(\nu^2+1/4)} = \frac{A}{(\nu^2+1/4)} + \frac{B}{(\nu^2+1/4)} = \frac{(A+B)\nu^2+(A/4+B)}{(\nu^2+1)(\nu^2+1/4)} \qquad \text{(A-15)}$$

By identification with the lefthand side of Eq (A-15) we find A=-B and (A/4+B)=3B/4=1. Thus B=-A=4/3. Using the fact that

$$\int_{\nu_1}^{\nu_2}\frac{d\nu}{(\nu^2+a^2)} = \frac{1}{a}\tan^{-1}\frac{\nu}{a}\Big|_{\nu_1}^{\nu_2} \qquad \text{(A-16)}$$

We obtain

$$T(\nu_0) = \left\{\int \pi + 2\tan^{-1}2\nu_0 + \frac{4}{3\ell n2}\left[2\tan^{-1}2\nu_0 - \tan^{-1}\nu_0 + \frac{\pi}{2}\right]\right\} \qquad \text{(A-16)}$$

We evaluate the surface integrals by first integrating over y. We must group the contribution from the polarization charge and its image charge in order for the integral to be bounded. We use the fact that

$$\int \frac{d(y-y')}{\sqrt{(y-y')^2 + (x-x')^2 + (z-z')^2}} = \int \frac{d(y-y')}{\sqrt{(y-y')^2 + C^2}}$$

$$= \ell n \left[(y-y') + \sqrt{(y-y')^2 + C^2} \right]$$

For the integral over the polarization charge we set $c = c_1$, and for the image charge we set $c = c_2$, where

$$c_1^2 = (x-x')^2 + [z + (d-\delta)]^2 \qquad \text{(A-17a)}$$

$$c_2^2 = (x-x')^2 + [z + (d-\delta)]^2 \qquad \text{(A-17b)}$$

We obtain:

$$\int_{-\infty}^{+\infty} \left[\frac{1}{|\vec{r}-\vec{r}'|} - \frac{1}{|\vec{r}-\vec{r}''|} \right] d(y-y') = \ell n \left[\frac{(y-y') + \sqrt{(y-y')^2 + C_1^2}}{(y-y') + \sqrt{(y-y')^2 + C_2^2}} \right|_{-\infty}^{+\infty}$$

When $(y-y') \to +\infty$ both numerator and denominator tend toward the same limit $2(y-y')$ and the logarithm of the ratio is 7 uo. When $(y-y') \to -\infty$, we readily see by expanding the square root

$$\sqrt{(y-y')^2 + C_1^2} = |y-y'| \left[1 + \frac{C_1^2}{2(y-y')^2} \right],$$

that the logarithm tends toward the limit $\ell n \frac{c_1^2}{c_2^2}$. The contribution to the potential due to the adhesive-dielectric boundary now becomes:

$$\delta\phi = \frac{\sigma_0}{2\pi}\left[\frac{1}{\epsilon}-\frac{1}{\epsilon_a}\right]\int_0^{\infty} dx'\ T(\nu_0)\ \ell n\frac{(x-x')^2+\left[(d-\delta)\right]^2}{(x-x')^2+\left[z+(d+\delta)^2\right]} \tag{A-18}$$

Where $\nu = \frac{x-x'}{2d}$ and $T(\nu)$ is given by Eq (A-16). Combining Eqs (A-1a) and (A-18) with σ_0 in Eq (A-1a) replaced by σ given by Eq (A-8), we obtain the following expression for the potential in the vicinity of the triple junction.

$$\Phi\ (X,Z) = \frac{2d\sigma_0}{\epsilon}\int_{\frac{-X}{2d}}^{\infty}\left\{ (1+\frac{1}{(1+\nu^2)\ell n2})\ \ell n\left[\frac{\nu 2+\frac{1}{4}(1+Z/d)^2}{\nu 2+\frac{1}{4}(1-Z/d)^2}\right] + \frac{1}{2\pi}\left[1-\frac{\epsilon}{\epsilon_a}\right]T(\nu)\ \ell n\left[\frac{\nu^2+\left[\frac{Z-\delta}{2d}\right]^2}{\nu^2+\left[\frac{Z+\delta}{2d}\right]^2}\right]\right\} -V \tag{A-19}$$

Where we used a new coordinate system centered at the triple junction (Ω, see Fig 1).

We note that the integral is zero when Z is set equal to zero and that $-\partial\Phi/dx = 0$ when $Z = 0$.

We now evaluate the electric field in the vicinity of the triple junction. The electric field in the X direction is

$$E_X = \frac{-\partial\Phi}{\partial X} = -\frac{\sigma_0}{\epsilon}\left[\left[1+\frac{1}{(1+V^2)\ell n2}\right]\ell n\left[\frac{V^2+\left[\frac{Z}{2\alpha}+1\right]^2}{V^2+\left[\frac{Z}{2\alpha}-1\right]^2}\right] - \frac{\sigma_0}{2\pi}\left[\frac{1}{\epsilon}-\frac{1}{\epsilon_a}\right]\ell n\ \frac{V^2+\left[Z+\frac{1^2}{2}(1-d/\sigma)\right]^2}{V^2+\left[Z+\frac{1}{2}(1+d/\sigma)\right]^2}\right]T(\nu) \tag{A-20}$$

where $V = -X/2d$

For Z > O the logarithm of the first term is positive, so that the first term leads to a negative E_x field that is attracting electrons toward the dielectric. The logarithm of the second term is negative so that the second term gives and attractive contribution if $\epsilon > \epsilon_a$ and repulsive if $\epsilon < \epsilon_a$.

We have

$$E_t = -\frac{\partial\phi}{\partial Z} = -\frac{2\sigma_o}{\epsilon} \int_{\frac{-X}{2d}}^{\infty} \left\{ \left[1+\frac{1}{(1+\nu^2)\ell n2}\right] \left[\frac{\frac{1}{2}(1+\frac{Z}{d})}{\nu^2+\frac{1}{4}(1+\frac{Z}{d})^2} - \frac{\frac{1}{2}(\frac{Z}{d}-1)}{\nu^2+\frac{1}{4}(1-\frac{Z}{d})^2}\right] \right. \tag{A-21}$$

$$\left. +\frac{1}{2\pi}\left[1-\frac{\epsilon}{\epsilon_o}\right] T(\nu) \left[\frac{\left[\frac{Z-\delta}{2\alpha}\right]}{\nu^2+\left[\frac{Z-\delta}{2d}\right]^2} - \frac{\left[\frac{Z+\delta}{2d}\right]}{\nu^2+\left[\frac{Z-\delta}{2d}\right]}\right]\right\} d\nu$$

$$= E_{1Z} + E_{2Z}$$

We have, to order $((Z/d)^2 << 1)$

$$E_{1Z} = -\frac{2\sigma_o}{\epsilon} \int_{\frac{-X}{2d}}^{\infty} \left[1+\frac{1}{1+\nu^2\ell n2}\right] \frac{1}{\nu^2+\frac{1}{4}}\, dv \tag{A-22}$$

$$= -\frac{2\sigma_o}{\epsilon} T\left[\frac{X}{2d}\right]$$

The second term, when expressed in terms of Z, becomes

$$E_{2Z} = -\frac{\sigma_o}{\pi}\left[\frac{1}{\epsilon}-\frac{1}{\epsilon_o}\right] \int_{\frac{-X}{2d}}^{\infty} T(\nu) \left[\frac{\frac{Z}{2d}-\frac{\delta}{2}}{\nu 2+\left[\frac{Z}{2d}-\frac{\delta}{d}\right]^2} - \frac{\frac{Z}{2d}+\frac{\delta}{d}}{\nu^2+\left[\frac{Z}{2d}+\frac{\delta}{d}\right]^2}\right] d\nu \tag{A-23}$$

The integral in Eq (A-23) cannot be performed analytically. In order to obtain analytical results we approximate T(ν) by the ratio of polynomials.

$$I(\nu) = \frac{\nu + a}{-\nu^2+b\nu+c} \tag{A-24}$$

When ν is small, we have, from Eq (A-16)

$$T(\nu) \simeq \pi \left[1+\frac{2}{3\ell n2}\right] + 4\left[1+\frac{1}{\ell n2}\right] \nu + O(\nu^2)$$

Expanding $I(\nu)$in powers of ν, we see that $I(\nu) = \frac{a}{c}\left[1 + \nu \left[\frac{1}{a}-\frac{b}{c}\right] + O\left(\nu^2\right)\right]$, which leads to the relations

$$\frac{a}{c} = \pi \left[1 + \frac{2}{3\ell n2}\right] = 6.163 \tag{A-25a}$$

$$\frac{a}{c} = \left[\frac{1}{a} - \frac{b}{c}\right] + 4 \left[1 + \frac{1}{\ell n2}\right] = 9.771 \tag{A-25b}$$

When $\nu \rightarrow \infty$, it is easy to see that $T(\nu)$ decreases toward zero and so does $I(\nu)$. We need one more equation to determine a, b, and c. We obtain this equation by calculating $T(\nu)$ at some intermediate joint, say $\nu = -1$. We have

$$T(-1) = 1.20 = \frac{a-1}{-\nu^2-b+c} \tag{A-25c}$$

The solution of Eqs (A-25a) through (A-25c) is: $a = -1.26$, $b = -0.204$ and $c = 0.678$. A plot of $I(\nu)$ and $T(\nu)$ is shown in Figure 2, from which one verifies the goodness of the fit. $I(\sigma)$ underestimates the actual function by at most 10 percent for $-1 < \nu < 0$ and overestimates $T(\nu)$ by at most 10 percent for $\nu < -1$.

We thus have

$$T(\nu) \approx \frac{\nu - 1.26}{-\nu^2 - 0.204b + 0,678} \tag{A-26}$$

For purpose of integration we can write

$$T(\nu) = \frac{\nu+a}{(\nu-a_1)^2 + a_2^2}$$

with $a = -1.26$, $a_1 = 0.678$, $a_2 = 0.597$. We can now readily perform the integrals in Eq (A-23) since the integral is compared in terms of the form

$$\frac{\nu + a}{(\nu-a_1)^2 + a_2^2} \times \frac{c}{\nu^2 + d^2}$$

which can easily be decomposed into the sum of two integral fractions

$$\frac{AV+B}{(\nu-a_1)^2+a_2^2} + \frac{CV+D}{\nu^2+d^2} \tag{A-27}$$

After some algebra, we find

$$A = \frac{a}{b^2} \frac{a_1^2 + a_2^2 - b^2}{(a_1^2+a_2^2-1)(a+2a_1^2b)-2a_1(a_1^2+a_2^2-b^2)} \tag{A-28a}$$

$$B = \frac{a}{b^2} - \frac{(a_1^2 + a_2^2)\ (a+2a_1b^2)\ A}{a_1^2+a_2^2-b^2} \tag{A-28b}$$

$$C = -A \tag{A-28c}$$

$$D = \frac{a + 2a_1\ b^2\ A}{(a_1^2+a_2^2-b^2)} \tag{A-28d}$$

The integrals in Eq A-23 are then performed readily, since

$$\int \frac{A_{v}+B}{(\nu-a_1)^2+a_2^2} = \frac{A}{2}\,\ell n\left[(\nu-a_1)^2+a_2^2\right] + (Aa_1+B)a_2 \tan^{-1}\left[\frac{\nu-a_1}{a_2}\right] \qquad \text{(A-29a)}$$

and, similarly

$$\int \frac{CV+D}{\nu^2+a^2} = \frac{c}{2}\,\ell n\left(\nu^2+a^2\right) + Dd \tan^{-1}\left[\frac{\nu}{d}\right] \qquad \text{(A-29b)}$$

REFERENCE

1) Gradsrleyn, I. and Ryzhnik, I., Table of integrals series and products, Academic Press, NY 1965), see Eq 4.241-7, p. 535.

Devivation of Eqs 28a through 28d.

AV+B

$$\frac{\nu+a}{(\nu-a_1)^2+a_2^2} \times \frac{1}{\nu^2+b^2}$$

$$= \frac{A\nu+B}{(\nu-a_1)^2+a_2^2} + \frac{CV+D}{\nu^2+b^2}$$

We have $(A\nu+B)(\nu^2+b^2) + (CV+D)\,[(\nu-a_1)^2+a_2^2] = \nu+a$.

$\nu^3(A+C)+V^2[B+D -2a_1C] +V[Ab^2+CA_2^2-2Da_1+Ca_1^2] + Bb^2 = D(a_1^2+a_2^2) = \nu + a$.

Thus

$$\left[\begin{array}{c} C = -A \\ B + D = -2a_1A \\ \left(b^2-a_2^2-a_1^2\right) A-2D = 1 \\ Bb^2 + D\left(a_1^2+a_2^2\right) = a \end{array}\right] \qquad \begin{array}{c}(1)\\(2)\\(3)\\(4)\end{array}$$

We express B and D in terms of A from Eqs (2) and (4).

$$D(a_1^2+a_2^2-b^2) = (a + 2a_1b^2)A$$

$$D = \frac{(a + 2a_1\, b^2)\, A}{a_1^2 + a_2^2 - b^2} \qquad (5)$$

from Eq (4)

$$B = \frac{a}{\ell^2} - \frac{\left(a_1^2 + a_2^2\right)\left(a + 2a_1\, b^2\right) A}{a_1^2 + a_2^2 - b^2} \qquad (6)$$

We insert into Eq (2)

$$\frac{a}{\sigma^2} + \left[- \frac{(a_1^2 + a_2)^2 (a + 2a_1 b_2) \ + \ a + 2a_1^2 b}{a_1^2 + a_2^2 - b^2} \right] = -2a_1 \ A$$

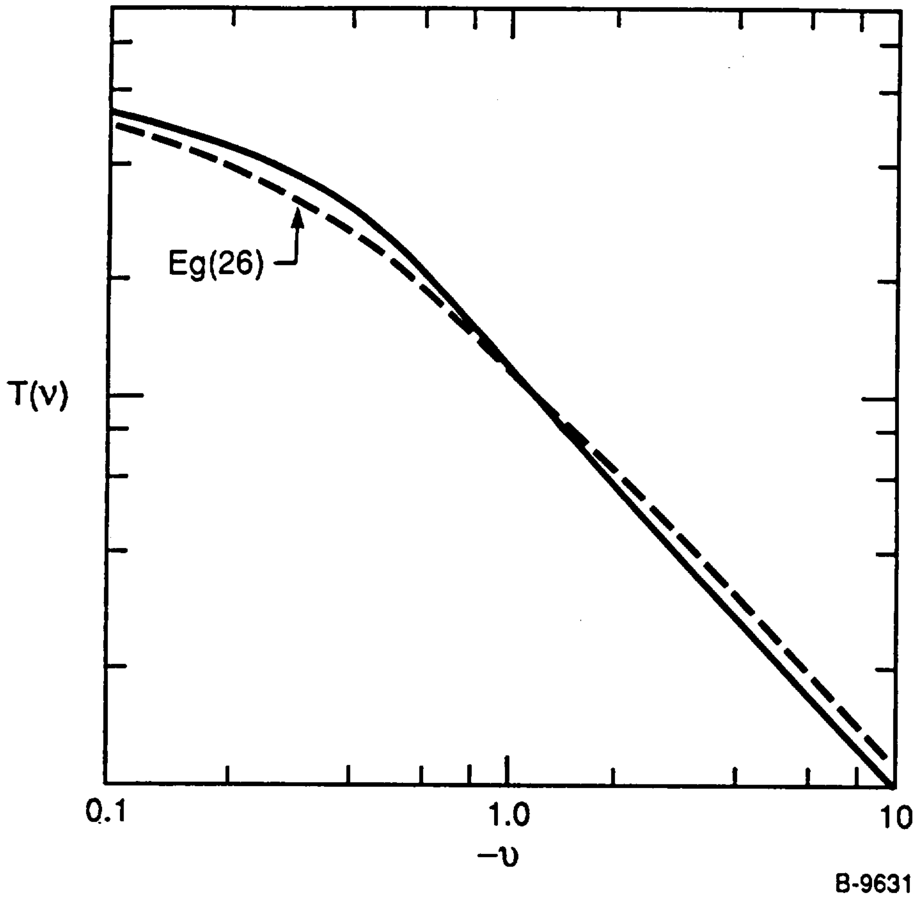

Figure 1

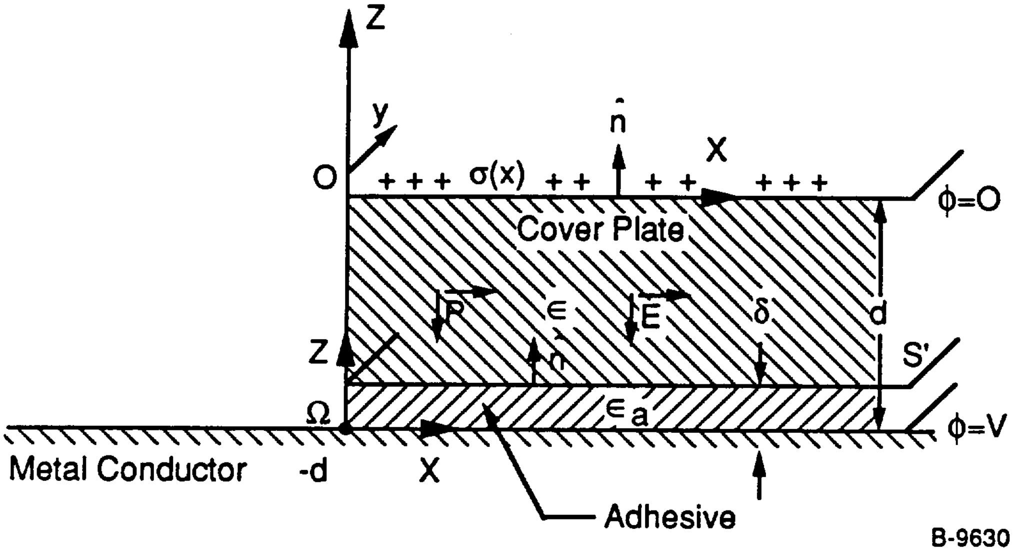
Z
y
n̂
X
O
+ + + σ(x) + + + + + + +
φ=O
Cover Plate
P
∈
E
δ
d
Z
n̂
S'
Ω
∈a
φ=V
Metal Conductor
-d
X
Adhesive
B-9630

Figure 2

```
   14. STIMS 3X ACC#  9336358      ISSUE # =  99      IPS-FILE ADABAS # =    10559
FICHE AVAIL    = AD             HARD COPY AVL = OK              COPYRIGHT       = N
ORIG AGENCY    = NASA           RECEIPT TYPE  = REG             ACQUIS  TYPE    = REG
DOCUMENT CLASS= TRP             ACCESS LEVEL  =   0             ACCESS RESTR    = UNRES
LIMITATION CAT= NONE            DOCUMENT SEC  = NC              TITLE SECURITY= NC
SUBJECT CATGRY= 33              SPECIAL HANDL =                 PAGE COUNT      = 00127
INC AUTHOR LST= N               INC CNTRCT LST= N               LANGUAGE        = EN
COUNTRY ORIGIN= US              COUNTRY FINANC= US              ABSTRACT PREP = NON
PUB DATE       = 19920100       CORP SOURCE   = PQ626284        JOURNAL PAGE    =    0

TITLE          = Arcing in space structures in low Earth orbit
TITLE SUPP     = Final Report, 1 Jan. 1990 - 29 Dec. 1991
AUTHOR       1 = Upschulte, B. L.
AUTHOR       2 = Marinelli, W. J.
AUTHOR       3 = Weyl, G.
AUTHOR       4 = Carleton, K. L.
CONTRACT NUM   = NAS3-25797
CONTRACT NUM   = SBIR-10.01-9030
REPORT NUM     = NASA-CR-194223
REPORT NUM     = NAS 1.26:194223
REPORT NUM     = PSI-2123/TR-1153
SALES AGY PRIC= Contact the Lewis SBIR Field Center Manager for fu
SALES AGY PRIC= rther information
MAJOR TERMS    = ARC DISCHARGES
MAJOR TERMS    = ELECTRIC ARCS
MAJOR TERMS    = SOLAR ARRAYS
MAJOR TERMS    = SOLAR CELLS
MAJOR TERMS    = SPACE STATION STRUCTURES
MAJOR TERMS    = SPACECRAFT CHARGING
MAJOR TERMS    = SPACECRAFT STRUCTURES
MINOR TERMS    = ADHESIVES
MINOR TERMS    = EARTH ORBITAL ENVIRONMENTS
MINOR TERMS    = OXYGEN ATOMS
MINOR TERMS    = PLASMA INTERACTIONS
FORM OF INPUT = HC

***************     END OF ADABAS RECORD #      10559     ***************
```